

---

**THE BREAKDOWN FIELDS AND RISETIMES OF SELECT  
GASES UNDER CONDITIONS OF FAST CHARGING (~ 20 ns  
and less) AND HIGH PRESSURES (20 – 100 Atmospheres)**

**Vic Carboni et al.**

**TITAN Systems Corporation  
Pulse Sciences Division  
2700 Merced Street  
San Leandro, CA 94577**

**November 2001**

**Final Report**

**APPROVED FOR PUBLIC RELEASE; DISTRIBUTION IS UNLIMITED.**



**AIR FORCE RESEARCH LABORATORY  
Directed Energy Directorate  
3550 Aberdeen Ave SE  
AIR FORCE MATERIEL COMMAND  
KIRTLAND AIR FORCE BASE, NM 87117-5776**

---


Using Government drawings, specifications, or other data included in this document for any purpose other than Government procurement does not in any way obligate the U.S. Government. The fact that the Government formulated or supplied the drawings, specifications, or other data, does not license the holder or any other person or corporation; or convey any rights or permission to manufacture, use, or sell any patented invention that may relate to them.

This report has been reviewed by the Public Affairs Office and is releasable to the National Technical Information Service (NTIS). At NTIS, it will be available to the general public, including foreign nationals.

If you change your address, wish to be removed from this mailing list, or your organization no longer employs the addressee, please notify AFRL/DEHP, 3550 Aberdeen Avenue SE, Kirtland AFB, NM 87117-5776

Do not return copies of this report unless contractual obligations or notice on a specific document requires its return.


This report has been approved for publication.



TYRONE C. TRAN, DR-II  
Project Manager



PAUL L. THEE, Lt Col, USAF  
Chief, High Power Microwave Division



R. EARL GOOD, SES  
Director, Directed Energy

REPORT DOCUMENTATION PAGE				Form Approved OMB No. 0704-0188	
Public reporting burden for this collection of information is estimated to average 1 hour per response, including the time for reviewing instructions, searching existing data sources, gathering and maintaining the data needed, and completing and reviewing this collection of information. Send comments regarding this burden estimate or any other aspect of this collection of information, including suggestions for reducing this burden to Department of Defense, Washington Headquarters Services, Directorate for Information Operations and Reports (0704-0188), 1215 Jefferson Davis Highway, Suite 1204, Arlington, VA 22202-4302. Respondents should be aware that notwithstanding any other provision of law, no person shall be subject to any penalty for failing to comply with a collection of information if it does not display a currently valid OMB control number. <b>PLEASE DO NOT RETURN YOUR FORM TO THE ABOVE ADDRESS.</b>					
1. REPORT DATE (DD-MM-YYYY) November 2001		2. REPORT TYPE Final Report		3. DATES COVERED (From - To) September 1999 – September 2001	
4. TITLE AND SUBTITLE The Breakdown Fields and Risetimes of Select Gases Under Conditions  of Fast Charging (~20 ns and less) and High Pressures  (20 - 100 Atmospheres)				5a. CONTRACT NUMB F29601-99-C-0165	
				5b. GRANT NUMBER N/A	
				5c. PROGRAM ELEMENT NUMBER 65502F	
6. AUTHOR(S) Vic Carboni, Heinz Lackner, and David V. Giri*				5d. PROJECT NUMBER 3005	
				5e. TASK NUMBER D0	
				5f. WORK UNIT NUMBER CK	
7. PERFORMING ORGANIZATION NAME(S) AND ADDRESS(ES)  TITAN Systems Corporation Pulse Sciences Division 2700 Merced Street San Leandro, CA 94577				8. PERFORMING ORGANIZATION REPORT NUMBER	
9. SPONSORING / MONITORING AGENCY NAME(S) AND ADDRESS(ES)  AFRL/DEHP 3550 Aberdeen Ave SE Kirtland AFB, NM 87117-5776				10. SPONSOR/MONITOR'S ACRONYM(S)  AFRL	
				11. SPONSOR/MONITOR'S REPORT NUMBER AFRL-DE-TR-2001-1077	
12. DISTRIBUTION / AVAILABILITY STATEMENT  APPROVED FOR PUBLIC RELEASE; DISTRIBUTION IS UNLIMITED.					
13. SUPPLEMENTARY NOTES *Pro-Tech 11-C Orchard Court Alamo, CA 94507-1541					
14. ABSTRACT An interest in wideband impulse-radiating systems has brought about the need to develop high-voltage timed-array antennas that can focus and steer an electromagnetic pulse in the far field. To produce desirable radiated signal levels in the far field, these arrays will need to be driven by high-voltage, high-power sources that at least in the short term will have to rely on pulsed based on gas spark gap technology. To produce the high frequencies, an array must be driven by sources with risetimes in the range of 100-200 ps or even faster. Since multiple pulsed will have to be used to drive a large array, a suitable pulsed design will most importantly have to have ultra-low triggering jitter (the standard deviation in the switch closure delay after trigger arrival). The jitter will have to be some relatively small fraction of this risetime to accurately steer and preserve the risetime. This implies a jitter ideally in the few tens of ps range. Although risetimes can routinely be achieved in this specified range, the jitter requirement represents a breakthrough in spark gap technology. This report describes the development and the performance of an ultra-low jitter and fast risetime triggered spark gap based pulsed and the gas breakdown and characterization experiments that lead to its realization.					
15. SUBJECT Jitter, Spark-gap, Triggered switches, Gas breakdown, Fast charging, Timed-array antennas, High-pressure switches, Multi-channel arcs					
16. SECURITY CLASSIFICATION OF:			17. LIMITATION OF ABSTRACT	18. NUMBER OF PAGES	19a. NAME OF RESPONSIBLE PERSON
a. REPORT Unclassified	b. ABSTRACT Unclassified	c. THIS PAGE Unclassified			Tyrone C. Tran
			Unlimited	104	19b. TELEPHONE NUMBER (include area code) (505) 846-0299



## TABLE OF CONTENTS

Section	Page
1.0 INTRODUCTION .....	1
1.1 Program Goals .....	1
1.2 Conceptual Design Approach .....	1
1.3 Development Program Plan .....	11
2.0 PHASE I GAS CHARACTERIZATION .....	12
2.1 Monocone Design .....	12
2.2 Monocone Data.....	18
2.2.1 Near Uniform Field Breakdown Dependency on Pressure.....	18
2.2.2 New Uniform Field Breakdown Dependency on Stress Time.....	41
2.2.3 Point-Plane Breakdown .....	44
2.2.4 Resistive Phase Risetime .....	47
3.0 PHASE II PULSER FABRICATION AND TESTING .....	49
3.1 Pulser Design .....	49
3.1.1 General.....	49
3.1.2 Marx Circuit.....	49
3.1.3 Pulser Circuit .....	53
3.1.4 Mechanical Layout.....	54
3.1.5 Diagnostics and Instrumentation.....	64
3.1.6 Parameter Variability .....	71
3.1.7 Chronology of Problems and Changes .....	72
3.1.8 Results.....	73
3.1.8.1 Polarity.....	73
3.1.8.2 Mushroom Stick-out and Distance and Gap Length.....	75
3.1.8.3 TS and OS Risetimes .....	89
3.1.9 Next Generation Pulser .....	92
4.0 CONCLUSION.....	93
Distribution List .....	94

## List of illustrations

Figure		Page
1	Laboratory demonstration pulser concept.....	2
2	Steerable NxM antenna array concept .....	2
3	Simplified Peaking Circuit .....	5
4	Practical V/N multiple channel 3 MV SF6 switch.....	7
5	Multichanneling demonstration switch (side view).....	8
6	Channeling photo of Aesop demonstration switch .....	9
7	Extent of multi-channeling with pressure and charge time .....	9
8	Monocone test fixture, elevation view.....	12
9	Monocone test fixture plan view of grounded bottom plate .....	12
10	Monocone test fixture plan view of top .....	13
11	Monocone test fixture .....	13
12	View of monocone test fixture in oil tank .....	14
13	Monocone tip .....	15
14	Point-plane electrode tip .....	15
15	Monocone instrumentation and diagnostic configuration.....	16
16	Gas breakdown monocone circuit.....	16
17	Typical monocone charging waveform measured by the resistive monitor .....	17
18	Marx with added series inductor.....	18
19	Monocone air negative polarity .....	20
20	Monocone air negative polarity .....	20
21	Monocone air positive polarity .....	21
22	Monocone air positive polarity .....	21
23	Monocone nitrogen negative polarity .....	22
24	Monocone nitrogen negative polarity .....	22
25	Monocone nitrogen positive polarity .....	23
26	Monocone nitrogen positive polarity .....	23
27	Monocone hydrogen negative polarity .....	24
28	Monocone hydrogen negative polarity .....	24
29	Monocone hydrogen positive polarity .....	25

### List of illustrations (Continued)

Figure	Page
30 Monocone hydrogen positive polarity .....	25
31 Monocone SF6 negative polarity .....	26
32 Monocone SF6 negative polarity .....	26
33 Monocone 15% SF6/85% air negative polarity .....	27
34 Monocone 15% SF6/85% air negative polarity .....	27
35 Monocone 15% SF6/85% air positive polarity .....	28
36 Monocone 15% SF6/85% air positive polarity .....	28
37 Monocone 30% SF6/70% air negative polarity .....	29
38 Monocone 30% SF6/70% air negative polarity .....	29
39 Monocone 30% SF6/70% air positive polarity .....	30
40 Monocone 30% SF6/70% air positive polarity .....	30
41 Point plane nitrogen negative polarity .....	31
42 Point plane nitrogen negative polarity .....	31
43 Point plane nitrogen positive polarity .....	32
44 Point plane nitrogen positive polarity .....	32
45 Point plane hydrogen negative polarity .....	33
46 Point plane hydrogen negative polarity .....	33
47 Point plane hydrogen positive polarity .....	34
48 Point plane hydrogen positive polarity .....	34
49 Point plane SF6 negative polarity .....	35
50 Point plane SF6 negative polarity .....	35
51 Point plane 15% SF6/85% air negative polarity .....	36
52 Point plane 15% SF6/85% air negative polarity .....	36
53 Point plane 15% SF6/85% air positive polarity .....	37
54 Point plane 15% SF6/85% air positive polarity .....	37
55 Point plane 30% SF6/70% air negative polarity .....	38
56 Point plane 30% SF6/70% air negative polarity .....	38
57 Point plane 30% SF6/70% air positive polarity .....	39
58 Point plane 30% SF6/70% air positive polarity .....	39

## List of illustrations (Continued)

Figure	Page
59 Monocone negative breakdown for all gases .....	40
60 Breakdown delay time .....	42
61 Hydrogen positive monocone tip .....	43
62 Point plane hydrogen and nitrogen .....	44
63 15% SF6 point plane positive and negative .....	45
64 30% SF6 point plane positive and negative .....	45
65 Control consoles.....	50
66 Marx generator.....	50
67 Marx enclosure, oil box and cart.....	50
68 Pulser.....	51
69 Coaxial feed and antenna .....	51
70 Simplified pulser circuit.....	52
71 Simulated charging waveforms.....	54
72 Low jitter triggered pulser .....	55
73 Typical fields at 300 kV .....	56
74 Self-breaking trigger switch.....	57
75 Interior of oil tank .....	58
76 Transfer switch mushroom electrode.....	59
77 Transfer switch charged electrode with mushroom removed .....	59
78 Transfer switch downstream electrode .....	60
79 Transfer switch electric fields before triggering with balanced mushroom voltage.....	60
80 UV illuminator downstream electrode with Torlon support for peaking capacitor.....	62
81 Peaking capacitor and output switch charged electrode assembly .....	62
82 Peaking capacitor and downstream output switch electrode with charged electrode removed .....	63
83 Downstream output switch electrode and coaxial feed section .....	64
84 Trigger coax calibration pulse (integrated D-dot) .....	65
85 Transfer switch charging voltage waveform (integrated D-dot).....	66
86 Transfer switch output waveform (integrated D-dot) .....	67



## List of illustrations (Concluded)

Figure	Page
87 Peaking capacitor charging waveform (integrated D-dot).....	67
88 Oil line calibration signal (integrated D-dot).....	68
89 Trigger coax calibration pulse (integrated D-dot) .....	69
90 Example of unintegrated pulser D-dot signals used to characterize its operation .....	70
91 Oil line output (integrated D-dot) .....	72
92 TS closure delay vs pressure.....	75
93 TS closure delay as function of % of self-break; TS gap 0.257 cm, nitrogen gas, mushroom stick-out 33% .....	76
94 TS closure delay vs. voltage with nitrogen gas; TS gap is 0.257 cm, stick-out 33% ...	77
95 TS closure delay vs. peak voltage for shots 682-691, TS gap 0.257 cm .....	78
96 TS closure delay vs. peak voltage for shots 692-701, TS gap 0.257 cm .....	78
97 TS jitter vs. percent of self-break for gap 0.257 cm and stick-out 33% .....	79
98 TS jitter vs. percent of self-break for a gap of 0.226 cm with nitrogen and mushroom stick-out 38% .....	81
99 TS closure delay vs. percent of self-break with nitrogen and 0.226 cm gap, 38% mushroom stick-out .....	82
100 TS closure delay vs. peak voltage with nitrogen, gap = 0.226 cm, 38% mushroom stick-out .....	83
101 TS jitter vs. percent of self-break, nitrogen gap 0.226 cm, stick-out 38%, 37.5 kV Marx.....	84
102 TS closure time as function of peak voltage for shots 1381-1391.....	85
103 TS and OS closure times as a function of TS voltage for shots 1413-1425 .....	86
104 TS and OS closure times as a function of TS voltage for shots 1393-1402 .....	86
105 TS closure delay vs. percent of self-break .....	87
106 TS jitter vs. percent of self-break with nitrogen; gap = 0.226 cm, mushroom stick-out 38% .....	88
107 TS and OS closure times as a function of TS voltage for shots 1457-1471 .....	88
108 TS and OS closure times as a function of TS voltage for shots 1556-1580 .....	89
109 TS output pulse with nitrogen, risetime = 300 ps .....	90
110 TS output pulse with hydrogen, risetime = 137 ps .....	90
111 Output voltage from integrated oil line D-dot output voltage ~280 kV .....	91

## List of Tables

Table	Page
1 Gas density data .....	4
2 Gas breakdown data plots .....	19
3 Pressure dependency of monocone breakdown field.....	40
4 Summary of breakdown field strengths for the mildly-enhanced monocone gap .....	41
5 Summary of enhanced breakdown field strengths .....	46
6 Monocone risetime data summary .....	47
7 Normal triggered shot arrival times of the D-dot signals at the oscilloscope .....	69
8 Prefire arrival times of the D-dot signals at the oscilloscope .....	71
9 TS jitter (gap 0.206 cm, mushroom stick-out 36%, nitrogen) .....	74
10 TS closure delay and jitter for a TS gap of 0.257 cm with 33% mushroom stick-out and positive trigger, output switch gap 0.194 cm.....	76
11 TS gap closure delay and jitter with nitrogen (0.226 cm, stick-out 33%, all 30 kV dc Marx charge, positive trigger, OS gap 0.105 cm with nitrogen) .....	79
12 TS gap closure delay and jitter (0.226 cm, mushroom stick-out 38%, positive trigger polarity; OS gap 0.105 cm, 37.5 kV and 45 kV Marx charge) .....	82
13 TS gap closure delay and jitter (0.226 cm, 38% stick-out, nitrogen; OS gap 0.105 cm hydrogen, 45 kV Marx charge).....	87

## 1.0 INTRODUCTION

An interest in wide-band impulse radar and even weapon systems has brought about the need to develop high-voltage phased antenna arrays that can focus and steer an electromagnetic pulse in the far field. The advantage of using a wide-band source rather than a fixed frequency source for radar is that the wide-band source produces a continuum of frequencies that are reflected from an object and can be detected. The signals associated with each selected frequency can be processed and combined using sophisticated imaging software to produce a composite image that more accurately represents the objects profile details than that resulting from a conventional fixed frequency radar.

To produce desirable radiated signal levels in the far field, these arrays will need to be driven by high voltage, high power sources that at least in the short term will have to rely on pulsed based on gas spark gap technology. To produce the high frequencies, an array must driven by sources with a risetimes in the range of 100-200 ps or even faster. Since multiple pulsed will have to be used to drive a large array, a suitable pulsed design will most importantly have to have ultra-low triggering jitter (the standard deviation in the switch closure delay after trigger arrival). The jitter will have to be some relatively small fraction of this risetime to accurately steer and preserve the risetime. This implies a jitter ideally in the few tens of picosecond range. Although risetimes can routinely be achieved in this specified range, the jitter requirement represents a breakthrough in spark gap technology.

This paper describes the development and the performance of an ultra-low jitter and fast risetime triggered spark gap based pulsed and the gas breakdown and characterization experiments that lead to its realization.

### 1.1 Program Goals

The goals of the program were to construct a pulsed that could drive a conical antenna with an exponential output pulse having the following specifications:

- Peak amplitude of up to 500 kV
- Pulse length (e-fold) of 5 ns
- Risetime of about 100 ps 10-90%
- $dV/dt \geq 5 \times 10^{15}$  V/s
- Jitter of about 25 ps
- Driven load impedance of between 67 and 135 ohms

The repetition rate goal was set at single shot to 1 Hz because of the budgetary limitations for providing ample power supplies and trigger supplies for faster repetition.

### 1.2 Conceptual Design Approach

A concept of the laboratory demonstration pulsed driving a single antenna is shown in Figure 1. Figure 2 shows a more practical concept where a larger antenna array is employed. Here, multiple synchronized pulsed would drive the array. Each antenna is coupled back to the driving

sources through variable transit time lines, perhaps designed as Trombone-like stepping motor-driven mechanisms or perhaps even electronically time varied sources, to enable synchronizing each antenna and steer the radiated pulse in the far field.

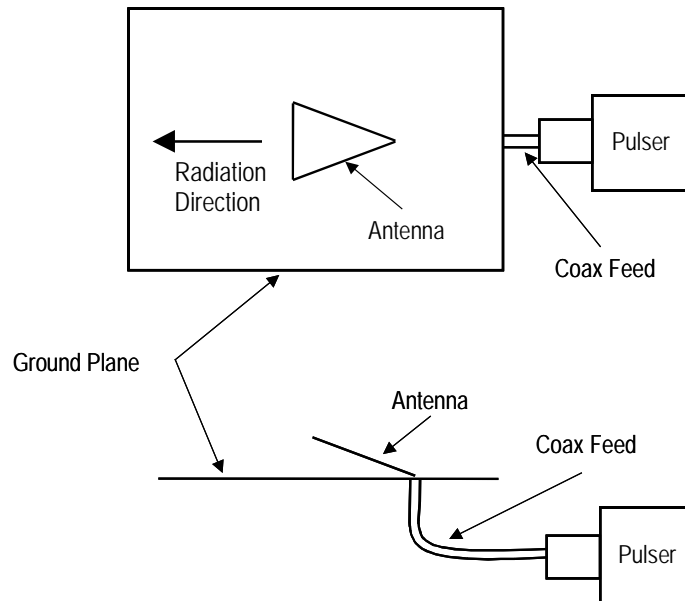


Figure 1. Laboratory demonstration pulser concept.

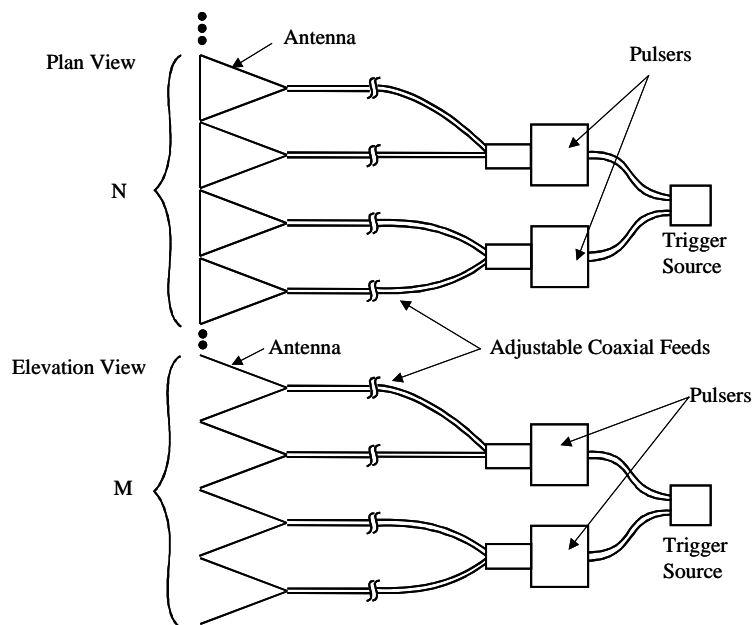


Figure 2. Steerable NxM antenna array concept.

The development program described here set out to construct a pulser of a design drawing from known technologies and relevant reportings in the literature as well as drawing from our own

common sense, experimental data and applications experiences. These inputs were applied to achieve the low jitter and fast risetime in a single pulser.

The point design for the pulser was also based on the practical aspects associated with eventual operation. For example, although laser triggering of a 100 kV, dc-charged SF6 gap has been demonstrated in our laboratory and has resulted in jitter as low as 125 picoseconds, the practicality of splitting and piping a high energy laser beam to many switches would require a complicated optics system. Such a system would not likely be suitable for field use outside the laboratory. Thus, the use of electrical triggering was chosen for use in the demonstration pulser. Drawing from the known formulas for predicting risetime, minimizing the resistive as well as the inductive contributions to risetime implies the use of high-pressure gases. The resistive phase risetime (e-fold) of the arc is calculated using the formula developed by J.C Martin:

$$\tau(R) = (88 \sqrt{p/p(\text{air})}) / ((F)^{4/3} (Z)^{1/3}) \text{ e-fold} \quad (1)$$

where:

$\tau(R)$	=	risetime in nanoseconds
$p$	=	density of the gas at operating pressure
$p(\text{air})$	=	density of air at STP
$F$	=	electric breakdown field at switch time in units of 10 kV/cm
$Z$	=	driven impedance in ohms

Because the rise is not exponential, multiplying by 1.8 converts the e-fold risetime to a 10-90% risetime:

$$\tau(R) = (158 \sqrt{p/p(\text{air})}) / ((F)^{4/3} (Z)^{1/3}) \text{ 10-90\%} \quad (2)$$

The inductive risetime of the arc is given by

$$\tau(L) = L/R \text{ e-fold} \quad (3)$$

$$\tau(L) = 2.2 L/R \text{ 10-90\%} \quad (4)$$

where:

$L$	=	arc inductance
$R$	=	driven impedance

The overall risetime is estimated by taking the quadrature sum of the resistive and inductive contributions.

Since the increase of breakdown field,  $F$ , of some common gases is generally known to follow a  $p^{0.7}$  relationship, where  $p$  is the pressure in absolute atmospheres, the denominator of the resistive phase formula increases with pressure faster than the numerator and thus the calculated risetime

decreases with higher pressure. Thus, operation at high gas pressures is desirable to reduce resistive phase risetime as well as the inductive risetime contributions by allowing the use of smaller gap spacing.

Furthermore, the choice of gas will also have an effect on the calculated resistive phase. Table 1 lists the densities of commonly used gases in pulse power. The use of hydrogen to achieve a fast risetime is well known. With a density about 8% of air and a breakdown strength about 75% of air, the resistive phase risetime for hydrogen should be less than half of that of air for similar pressure according to Equation (1). Thus, hydrogen should be an excellent candidate for a fast risetime gas switch.

Table 1. Gas density data.		
Gas (dry)	Density (STP)	Relative Density
Air	0.001205 g/cc	1.00
Nitrogen	0.001251 g/cc	1.04
Hydrogen	0.00008988 g/cc	.075
SF6	0.006387 g/cc	5.30
15% SF6 / 70% Air	0.00198	1.64
30% SF6 / 50% Air	0.00276	2.29

On the other hand, SF6 with a density of 5.3 times air and a relative breakdown field approximately three times air would also result in a calculated risetime half of that with air. Experience has shown however, that at low currents the arc channel evidently does not heat up fast enough to achieve a small resistive phase risetime component. This was observed when approximately 200-300 kV discharged into 150-ohm impedance. The resulting current in the range of 1-2 kA yielded risetimes at least two to three times greater than expected from the calculation.

The current in the demonstration pulser will generally be higher than 1-2 kA. Perhaps 3-5 kA will be more likely which will reduce or eliminate the arc channel-heating problem. Thus, SF6 might also be considered as an appropriate gas for a fast risetime switch.

A side thought though, is that SF6 with its high hold-off fields at high pressures will require a very small gap spacing. For the triggered switch this may make it very difficult to maintain accurate separation distances as well as planarity between the mushroom trigger electrode and adjacent electrodes.

Mixes of SF6 and air could also be interesting candidates and will be examined during the gas characterization phase. Liquifactors of the SF6, however, limits the maximum fields achievable.

Nitrogen and air are also considered appropriate candidates for switching gases because of their availability and cost and will be tested.

In general, another requirement for fast risetime switching and the preservation of the fast risetime pulse after switchout is to keep all of the components physically small, transit times small, and avoid abrupt contour changes and impedance mismatches. In the time regime of 100-

200 ps risetimes, the two-way transit time of only 1 cm is on the order of the risetime. Thus, in regions where the wave front must establish itself, spacings and volumes must be kept to lengths on the order of a centimeter or so to maintain a risetime in the desired range.

Another assumed requirement for the pulser design is the use of rapid charging to achieve higher breakdown fields and to take advantage of the formative time of the peaking switch gap, described below. Since a higher breakdown field,  $F$ , shows up in the denominator of the resistive phase formula, increasing it reduces the resistive phase risetime. Obviously this also helps to lower the inductive risetime contribution by allowing a smaller gap to be used for a given voltage.

In the literature, it has been reported that when a specific SF6 gap was rapidly charged in a time less than or comparable to the formative time and was UV-illuminated, a diffuse breakdown was observed where there appeared to be no discrete channels formed. Typically, the formative time falls into a range of 1 to 1.5 nanoseconds. Thus, the peaking switch circuit is designed to be charged within this time span and UV-illuminated to achieve as low inductance as possible.

Another requirement for rapid charging is in the trigger source pulse. We know from experience that the jitter of a triggered switch is usually dependent on the risetime of the trigger pulse especially for a non-UV-illuminated gap. Typically, the jitter might be 10% of the trigger pulse risetime for a trigger risetime in the 10-100 ns range. Thus, the trigger pulse risetime for the demonstration pulser will be as fast as possible preferably in the 200 ps range and will be preserved so it can be applied directly to the trigger electrode.

To achieve the necessary rapid charging of the switches and the fast output risetime, a traditional peaking circuit is used. This circuit concept is shown in simplified form in Figure 3. The circuit uses two stages to achieve risetime and pulse compression. Roughly, the desired decay time is determined by the primary stage capacitance  $C_1$  discharging into the load impedance.

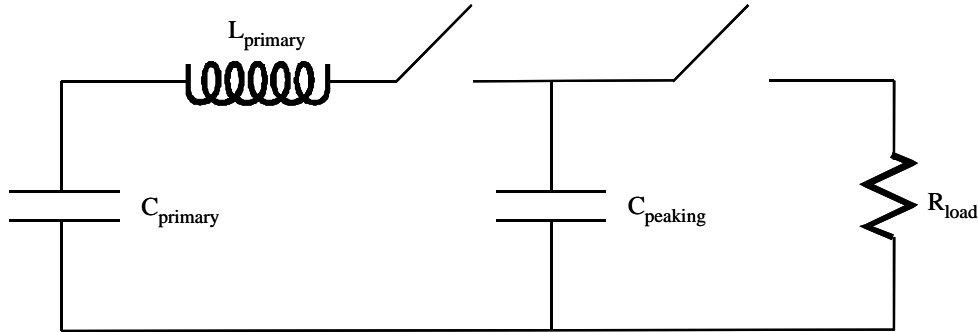


Figure 3. Simplified peaking circuit.

The sizing of the peaking capacitor,  $C_p$ , can roughly be calculated from the other circuit parameters using the formula:

$$C_p = \left( \left( L/R^2 \right) / \left( 1 + \left( L/R^2 \right) C_1 \right) \right) \quad (5)$$

Where  $C_1$  and  $L$  are the capacitance and inductance associated with the primary discharge circuit and  $R$  represents the driven load impedance.

The reason that this determination of the peaking capacitor value is rough is that the formula assumes lumped circuit parameters where the charge times are long compared to the transit time between  $C_1$  and  $C_p$ . In the fast risetime demonstration pulser the physical dimensions of the circuit will be small and the charge time of the peaking capacitor very short. The two will be comparable, thus the charging of the peaking capacitor is initially through a transmission line impedance rather than a lumped inductance for a significant fraction of the charge time.

In the demonstration pulser, the first stage of the circuit will be triggered and the peaking stage self-breaking. This is the most practical approach because the dimensions of the peaking region will have to be smaller than the primary stage region to produce and preserve the fast risetime. Introducing a trigger into the small peaking switch would be a difficult thing to do.

As will be discussed below, the intended triggering method should produce multi-channeling. Multi-channeling will significantly reduce the risetime of the triggered primary switch. Under optimal conditions of gas type and pressure, the risetime of this switch could be in the 100-200 ps. It is conceivable that a peaking stage is not necessary to achieve the output risetime. Exploiting this possibility of the primary switch by itself being fast enough was considered risky for two reasons. The first is that there was the possibility that the desired risetime would not be achievable from a single triggered switch. The second reason was the difficulty of extracting the pulse from the triggered gap geometry. The radially expanding wave would be difficult to feed directly into one or more coaxial lines. The latter, to our knowledge, has ever been achieved at up to 500 kV and with a 100 ps risetime.

The effectiveness of electrical triggering is well established and a  $V/n$  field distortion switch configuration is selected as the point design approach for the demonstration pulser. In a  $V/n$  switch, a mushroom-shaped trigger electrode is placed at a distance from the adjacent electrode that is a fraction of  $1/n$  of the total gap spacing. Figure 4 shows an example of such a configuration where typically in a practical switch,  $n$  ranges from two to ten.

The switch works by carefully shaping the mushroom and floating or balancing it so that it lies on what would be an equipotential contour if there were no mushroom introduced into the gap. This way the mushroom edge is not enhanced and the presence of the mushroom does not disturb the field distribution within the gap region.

There are two gaps formed when the mushroom is introduced. The one between the mushroom and its adjacent electrode through which the mushroom stem passes is the smaller gap and has a voltage difference of  $1/n$  of the total gap voltage. The other, the larger gap, has a voltage difference of  $(n-1)/n$  of the total gap voltage.

When a trigger pulse is applied to the mushroom, it is optimal when the larger of the two gaps breaks first. The trigger pulse must swing the mushroom's potential such that the large gap potential increases which distorts the field and launches streamers off the sharp mushroom edge. Ideally, the smaller gap differential voltage goes from the initial  $\Delta V$  to  $-\Delta V$ . Going too far with a



higher voltage trigger or using the wrong polarity trigger could actually cause poorer performance in terms of jitter because the smaller gap might likely would close first.

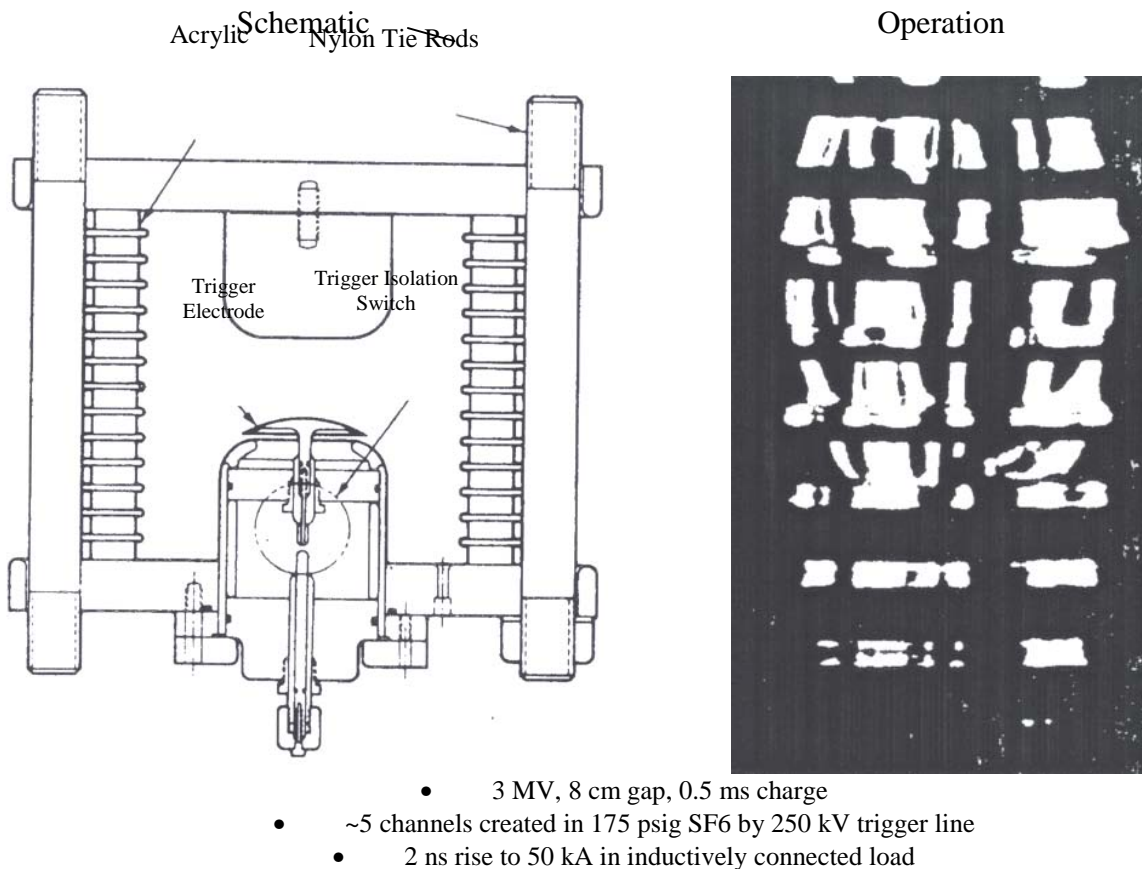


Figure 4. Practical V/n multiple channel 3 MV SF6 switch (Mercer, Martin, PI/Sandia, 1974).

The advantage of the V/n switch is that a relatively small trigger voltage can be used to switch a significantly larger voltage. For example, the switch shown in Figure 4 was a V/10 configuration that was actually fielded. A voltage of 3 MV was switched through an 8 cm SF6 gas gap at 175 psig and needed only a trigger pulse of 250 kV. The trigger pulse was very effective as evidenced by the five channels that were routinely produced.

In the demonstration pulser, a value of  $n$  between 4 and 6 is planned to be used. This sets the trigger pulse voltage at about 100 kV for the 500 kV pulser output, which is a reasonable value. Low jitter and multi-channeling seem to go hand in hand. This seems reasonable because if there were significant jitter in the switch, one streamer would likely outpace the others and result in a single channel.

In an experiment at PSI to investigate fast risetime switching in the HDL (now ARL)-funded AESOP-II program, a 1 MV, 9.5-ohm monocone was constructed with a 1 cm gap and a 4-inch diameter mushroom trigger electrode using SF6. The mushroom position formed approximately a V/2.5 switch. A schematic of this switch is shown in Figure 5.

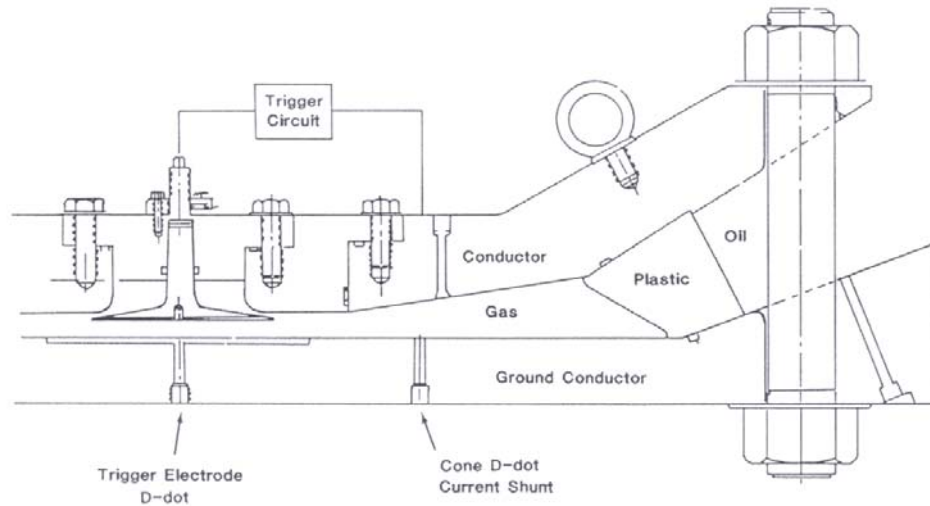


Figure 5. Multi-channeling demonstration switch (side view).

The intent of this design was to produce multi-channeling and thus, a fast risetime. The mushroom projected out of the top plate, which was the charged electrode. The bottom electrode or plate was at ground potential. The trigger for this switch was derived from a 1-ns long (one way), 25-ohm transmission line connected directly to the mushroom. This line was capacitively-balanced so that the small gap differential voltage was  $1/2.5$  the total gap voltage.

The far end of the trigger line was shorted by a self-breaking gas switch which when closed launched an equal amplitude but opposite polarity pulse down the line. The trigger pulse risetime, limited primarily by the inductance of the shorting switch, was estimated to be on the order 1 ns; less than or equal to the expected formative time of the gap. With the rather close coupling of the line to the mushroom, this risetime was believed to have been preserved and directly applied to the mushroom.

The switch exhibited multi-channeling performance with at least 10 channels routinely observed as shown in Figure 6. Later investigations during which parameter scans were performed showed that better multi-channeling occurred with higher pressure and faster charging of the monocone. Figure 7 shows this trend. The best results were obtained at 180-200 psig SF<sub>6</sub> and the fastest charge times possible with the hardware that was on the order of 25 ns.

Although jitter was not measured, the extreme number of channels would imply low jitter. Thus, the demonstration pulser's triggered switch will use both a fast charge on the order of 25 ns or less and a fast rising trigger pulse well under the formative time of the gap.

Another general observation that should be considered in the design is that a positive trigger pulse produces better triggering performance. The lower breakdown field for enhanced positive polarity causes this to occur. Thus, a positive trigger pulse will be accommodated.

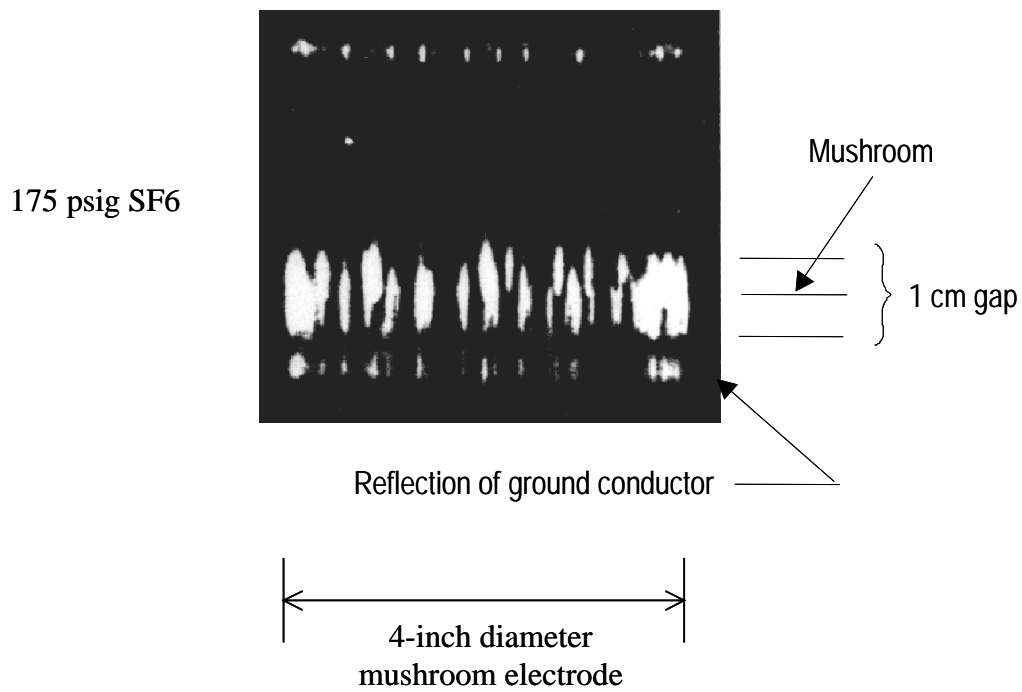


Figure 6. Channeling photo of Aesop demonstration switch.

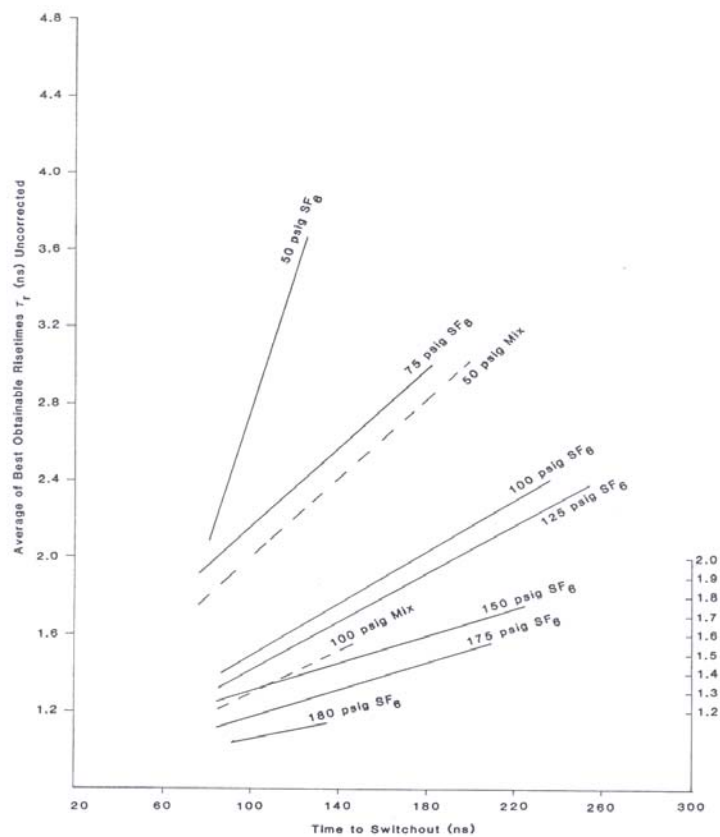


Figure 7. Extent of multi-channeling with pressure and charge time.

For the small dimensions of the components, particularly the primary and peaking capacitors, and the high voltages used here, the use of water and oil dielectrics outside the switch regions is most practical. Solid materials such as ceramic or plastic for the capacitor dielectrics simply do not have the voltage hold-off capability.

In the general design of the pulser, the liquid spacings are based on the commonly used formulas for the water and oil breakdown field,  $F$ . These are

$$F_+ (\text{kV/cm}) = 230 t^{-1/3} A^{-0.058} \quad \text{positive side water} \quad (6)$$

$$F_- (\text{kV/cm}) = 557 t^{-1/3} A^{-0.069} \quad \text{negative side water} \quad (7)$$

$$F_+ (\text{MV/cm}) = 0.48 \alpha t^{-1/3} A^{-0.073} \quad \text{positive side oil} \quad (8)$$

$$F_- (\text{MV/cm}) = K - 0.48 \alpha t^{-1/3} A^{-0.073} \quad \text{negative side oil} \quad (9)$$

where

$$\begin{aligned} F_{\pm} &= \text{positive/negative breakdown field} \\ t &= \text{effective stress time measured at 63\% } \mu\text{sec} \\ A &= \text{area cm}^2 \\ \alpha &= 1 + 0.12 \sqrt{((E_{\max}/E_{\text{mean}}) - 1)} \\ K &= 1.7 \text{ if enhancement is } > 1.14 \\ &= 1 \text{ if enhancement is } < 1.14 \end{aligned}$$

Spacings in the pulser were sized to produce fields nominally  $< 75\%$  of the calculated breakdown fields using the above formulae. Fields were determined using the Quickfield application software.

In summary, the point design of the pulser incorporates the following features:

- Use of gas switches
- Provision to use hydrogen, nitrogen, air, and SF6
- Use of high pressure gas
- Provision for pressures to 100 atm.
- Small dimensions and smooth and impedance matched profiles
- Use of two-stage peaking circuit
- Use of water dielectric capacitors
- Use of field distortion triggered primary switch
- Use  $\sim V/5$  switch
- Use of a self closing UV illuminated peaking switch
- Fast charging of the switches
- $\sim 25$  nanosecond charge time of the primary stage triggered switch
- $\sim 1 - 1.5$  ns charge time of peaking stage
- Use of a fast  $\sim 200$  ps trigger pulse

### 1.3 Development Program Plan

The development program of the demonstration pulser was divided into two phases. The first phase characterized candidate gases while the second phase designed, fabricated, and tested the pulser.

The goals of each phase were as follows:

#### **Phase 1:**

- Characterize the breakdown of air, nitrogen, hydrogen and SF6 and SF6 mixes
- Breakdown field vs. pressure
- Polarity effects
- Varying stress times
- Uniform field
- Point-plane
- Compare actual measured risetimes to calculations
- 

#### **Phase 2:**

- 
- Fabricate the demonstration pulser test bed
- Characterize the pulser performance
- Gas type characteristics
- Triggerability
- Jitter of triggered switch
- Jitter of self breaking switch
- Gap closure delay after triggering
- UV illumination effectiveness
- Risettime of multi-channeling triggered switch
- Risettime of peaking switch
- Optimal positioning and biasing of mushroom electrode
- Drive an antenna
- Measure radiated fields

## 2.0 PHASE 1 GAS CHARACTERIZATION

### 2.1 Monocone Design

A monocone design was chosen to evaluate the gas characteristics. The reason for this design was to provide a well-defined geometry of calculable and constant impedance unobstructed for a sufficient clear time in order to be able to measure the arc risetime and compare it to calculation. The monocone was constructed to be used in conjunction with the pulser test bed hardware. The monocone is sized to fit into the pulser oil tank and is designed to be charged by the same Marx used for the pulser tests. Photographs of the monocone construction are shown in Figures 8 through 10 which show the plan, top and bottom views. Figure 11 shows a schematic layout. Figure 12 shows the monocone installed in the pulser test bed oil box.

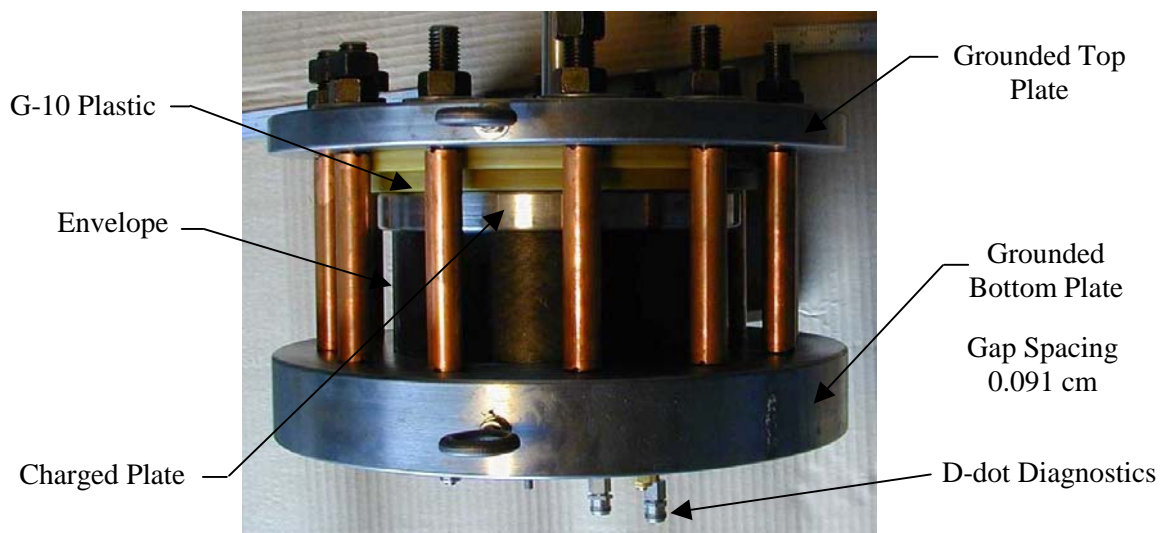


Figure 8. Monocone test fixture, elevation view.

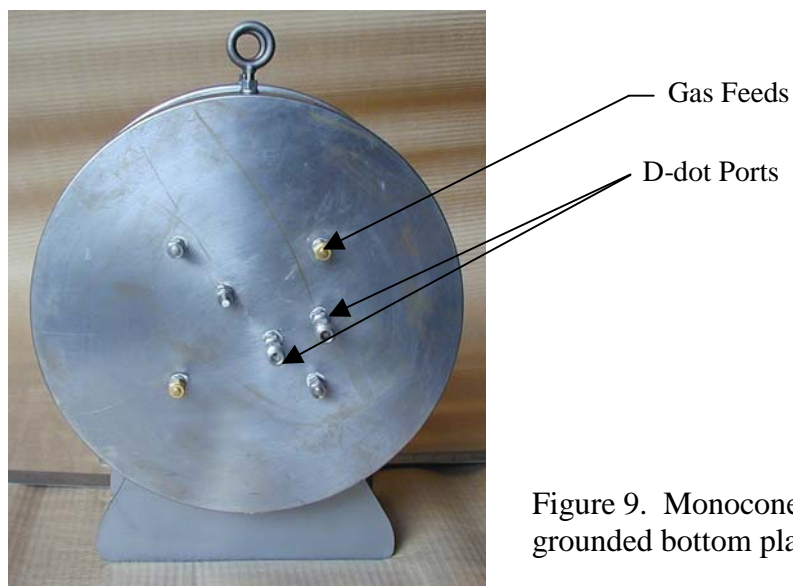


Figure 9. Monocone test fixture plan view of grounded bottom plate.

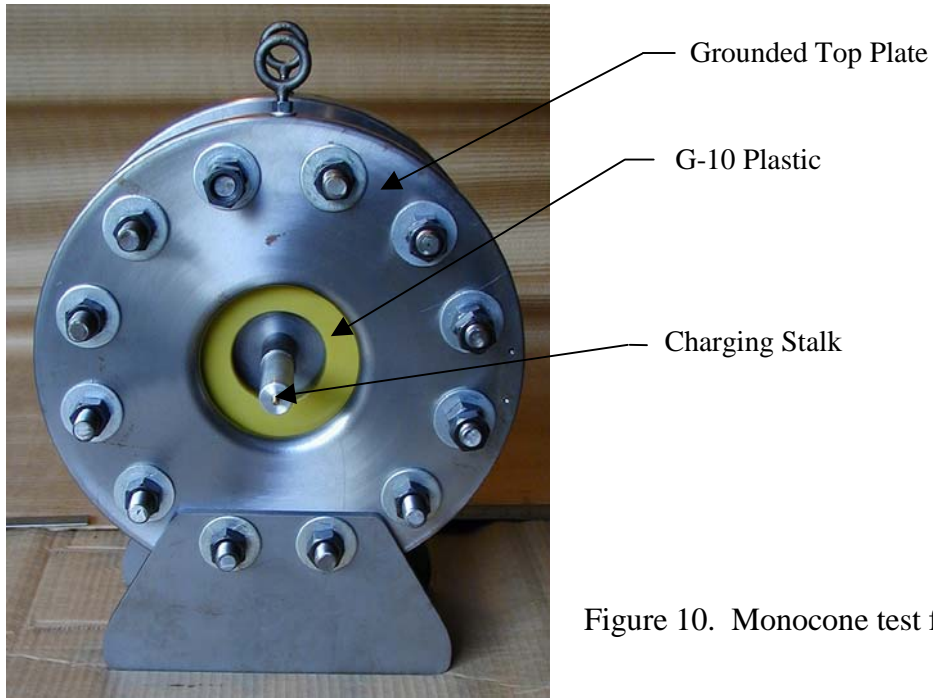


Figure 10. Monocone test fixture plan view of top.

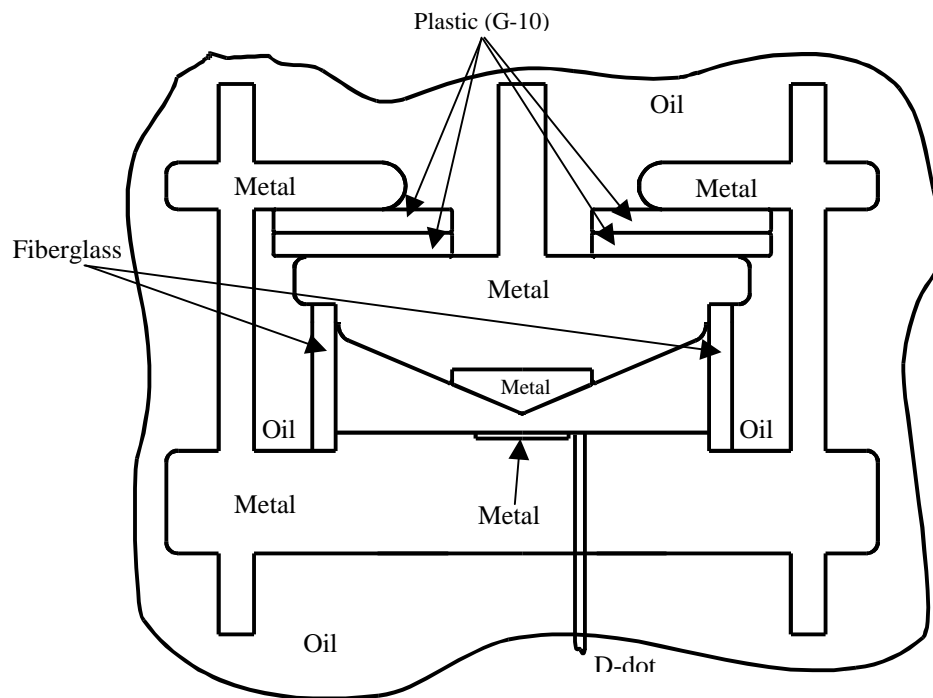


Figure 11. Monocone test fixture.



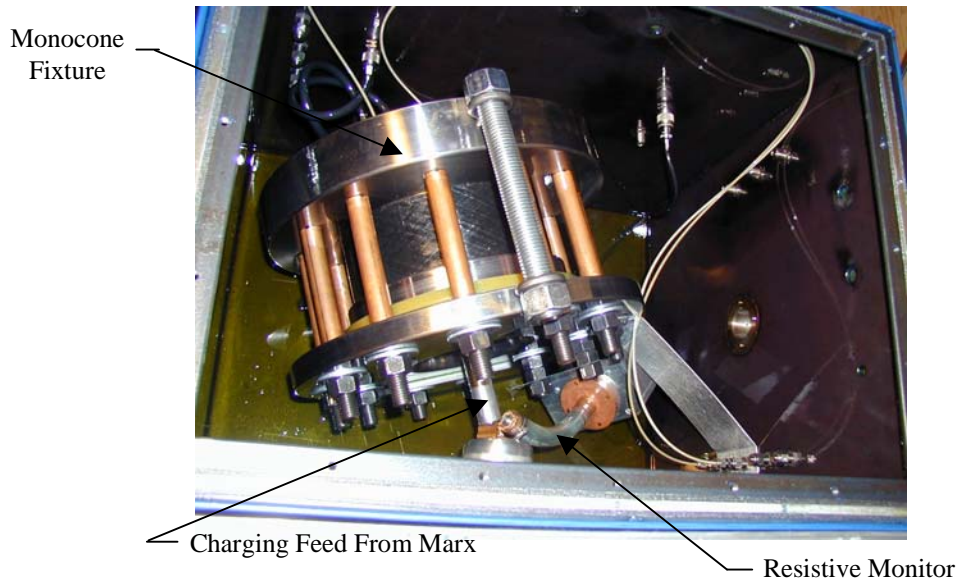


Figure 12. View of monocone test fixture in oil tank.

The cone can safely be pressurized to 100 atmospheres with any of the candidate gases including hydrogen. The inner diameter of the pressurized vessel envelope is approximately 8 inches and is approximately 3 inches long. The smaller conductive top endplate of the vessel with the conical shaped interior contour is the charged end. The opposite plate is flat and is the grounded side.

The charged plate is sandwiched between the grounded flat monocone plate and a second annular steel plate that is also grounded. The charged top plate is insulated from this second plate by two stacked layers of ½-inch thick G-10 plastic. A stalk connected to the charged plate extends through the hole in the second steel plate and connects to the charging input lead from the Marx. The two grounded steel plates are bolted together with 12 steel tie rods that transfer the compressive forces to the monocone top plate through the annular G-10 sheets. This design avoided the use of Torlon tie rods that would have been very costly and not even feasible for use at these pressures and the chosen diameter of the vessel.

The monocone impedance is 16.5 ohms and the apex tip is made of stainless steel. The flat ground plate is fitted with a 2-inch-diameter by 0.125-inch-thick stainless steel strike plate. The enhancement of the monocone apex tip is 1.38 with a gap of 0.091 cm which was used throughout the testing. Figure 13 shows this tip.

For point-plane breakdown testing, the apex tip of the monocone was removed. This removable apex tip section was truncated flat approximately 5/8-inch above the tip. A 3-inch diameter disk with a pointed needle-like end replaced the removed apex section. The point is shown in Figure 14. The diameter of the point is between 0.018 and 0.020 inches and the thin diameter shank is approximately 0.18 inches long. A gap of 0.18 cm was used for the point-plane tests.

The grounded monocone flat plate (see Figure 9) is equipped with several D-dot ports. Two are positioned 1.19 inches from the apex and another is positioned 2.5 inches from the apex. The clear time of the wave-front is determined by the two-way transit time between the position of



the D-dot and the impedance discontinuity of the vessel wall. The clear time of a wave-front signal detected by the D-dot in the either of the closer ports is approximately 560 ps while the clear time of the furthest D-dot is about 250 ps.



Figure 13. Monocone tip.



Figure 14. Point-plane electrode tip.

The estimated D-dot risetime is 25 ps which is approximately determined by the transit time of a wave across the cut-off end of the 0.25-inch-diameter semi-rigid cable. The D-dot was calibrated against a 2500-ohm liquid resistive monitor with an attenuation factor of 1480/1 that was itself calibrated against a reference monitor using standard traceable PSI calibration standards. The D-dot was used to measure risetime while the resistive monitor measured voltage amplitude.

A TDS 684C with a bandwidth of 1 GHz was used to record the charging waveforms for determining the charge time and amplitude. An SCD 5000 with a bandwidth of 4.5 GHz was used to measure the output risetime.

The cable from the monocone to the SCD-5000 oscilloscope was 1/2-inch-diameter Foamflex used in conjunction with a DC-11 compensated delay line. The throughput risetime of the SCD

5000, cabling, and delay line is estimated to be 100 picoseconds. The diagnostics diagram is shown in Figure 15.

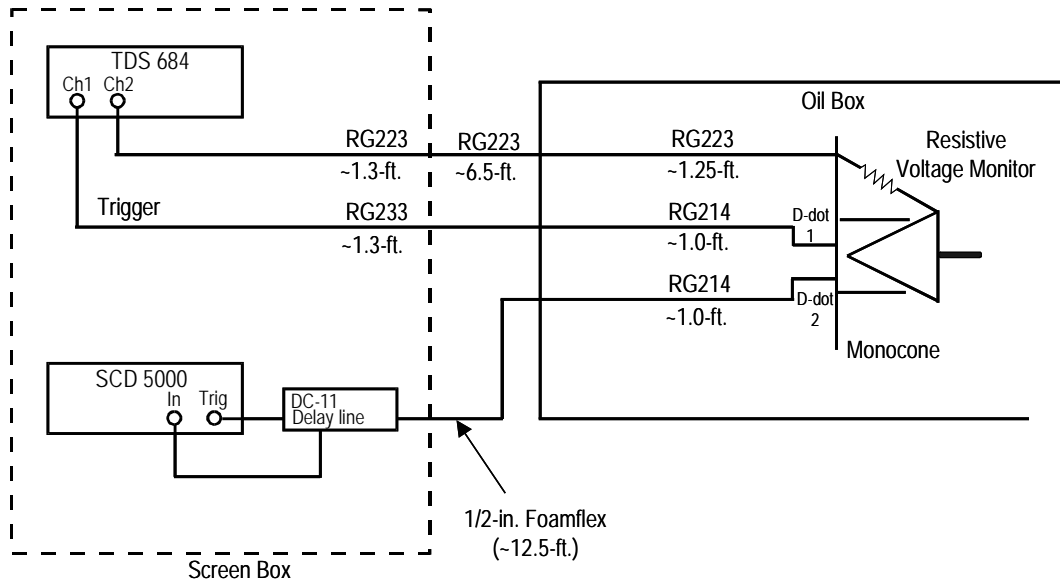
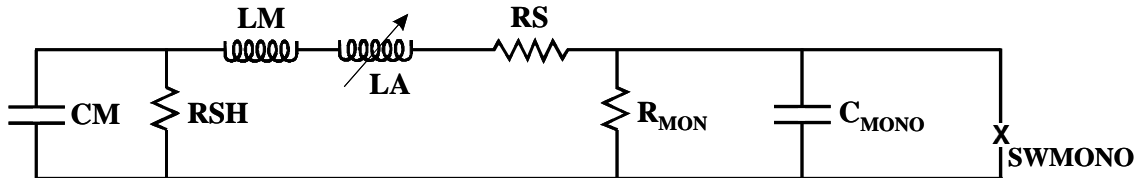


Figure 15. Monocone instrumentation and diagnostic configuration.

The circuit schematic for the monocone test configuration is shown in Figure 16. Details of the Marx are described in the section of this report that discusses the pulser. For the monocone tests, additional 300 ohms were placed between the Marx and the monocone to limit the late-time current through the arc channel. This minimized the wear on the electrode tips and possible degradation of the measured breakdown fields.



CM (Marx Capacitance)	425 pF
RSH (Marx Shunt Resistance)	1000 ohms
LM (Marx Series Inductance)	1.5 $\mu$ H
LA (Added Series Inductance)	0 or 16 $\mu$ H
RS (Added Current Limiting Resistance)	300 ohms
RMON (Resistive Monitor)	2400 ohms
CMONO (Equivalent Capacitance of Monocone Load)	210 pF
SW MONO (Monocone Gap)	

Figure 16. Gas breakdown monocone circuit.

The equivalent capacitance of the monocone load was much greater than expected because of the G-10 that was used (see the previous description of the monocone construction). The initial concept was going to use a low dielectric plastic but final calculations determined that G-10 was required for mechanical compressive strength. G-10 has a dielectric constant of at least five which is more than twice that of the more common plastics. This made the equivalent capacitance of the monocone about 210 pF. Thus, the maximum voltage on the load as determined by simulation was only about 50% of the open circuit Marx output voltage. This determined the gap spacing of the monocone so useful fields could be achieved for this limited voltage.

An important parameter that was varied was the application time of the voltage on the gap which defines the effective stress time. The effective stress time, referred to as  $t_{\text{eff}}$ , is defined as the time the voltage exceeds a level of 89% of its peak prior to breakdown.

The value of  $t_{\text{eff}}$  is measured from each waveform as the time between the 89% level and the 100% level, which is where the gap breaks down. Figure 17 shows a typical waveform indicating the measured stress time.

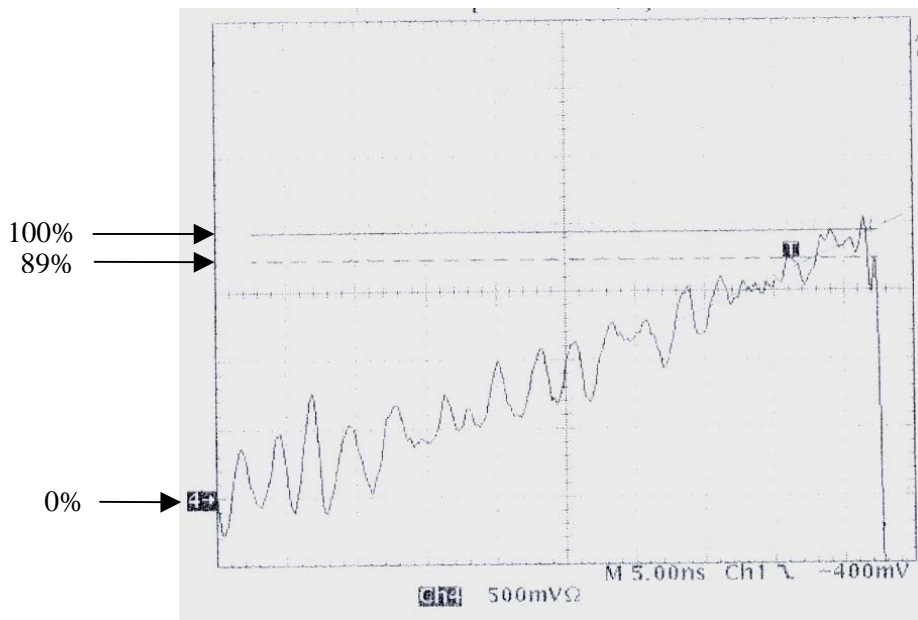


Figure 17. Typical monocone charging waveform measured by the resistive monitor.

The stress time can be varied by several means. One method is to place an additional 16  $\mu\text{H}$  in series with the Marx that increases the charge time by a factor of about four times. This added Marx series inductance is shown in Figure 18. Another is to vary the dc charge voltage of the Marx and consequently the Marx output voltage for a given pressure. The range of stress times achieved using these methods in combination was approximately 1 to 5 ns.

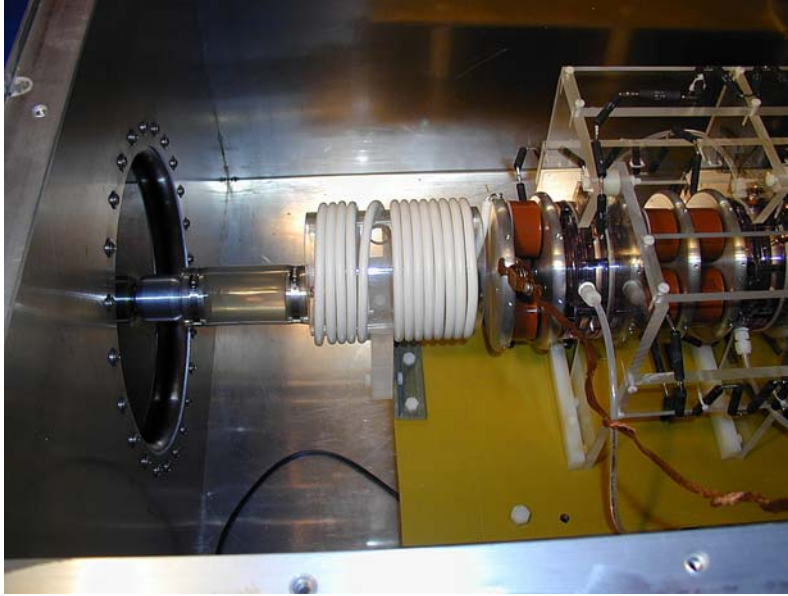


Figure 18. Marx with added series inductor.

## 2.2 Monocone Data

The available monocone breakdown field data is organized and listed in Table 2 and plotted in Figures 19 through 58. The data includes the breakdown fields of air, nitrogen, hydrogen, SF<sub>6</sub> and two SF<sub>6</sub>/air mixes as a function of pressure, polarity, and applied voltage stress times. Data is presented for both the mildly-enhanced monocone (enhancement factor  $\sim 1.38$ ) and highly-enhanced point-plane electrode geometries. Note that in a number of plots the data points did not print so only the trend line is shown.

### 2.2.1 Near Uniform Field Breakdown Dependency on Pressure

The monocone breakdown field data for the various gases with negative polarity on the cone tip are plotted as a group in Figure 59 and show the scaling relationship of breakdown field with pressure. The breakdown field versus pressure relationships applies to the stress times tested, which were in the range of approximately 1 to 5 ns.

A power law regression was fitted to the data to derive the equation for the indicated trend line. For mildly-enhanced electrodes using air, nitrogen, and hydrogen in the pressure range of roughly 30 to 100 atmospheres (absolute), the gas breakdown fields scale with pressure as roughly between  $p^{0.5}$  and  $p^{0.6}$ . Table 3 summarizes the pressure-scaling exponent for the monocone breakdown data in both negative and positive polarities.

Table 2. Gas breakdown data plots.

Fig. #	Configuration	Gas Type	Polarity	Variables Plotted
19	Monocone	Air	N	Breakdown field vs. pressure
20	Monocone	Air	N	Breakdown field vs. $t_{eff}$ at various pressures
21	Monocone	Air	P	Breakdown field vs. pressure
22	Monocone	Air	P	Breakdown field vs. $t_{eff}$ at various pressures
23	Monocone	Nitrogen	N	Breakdown field vs. pressure
24	Monocone	Nitrogen	N	Breakdown field vs. $t_{eff}$ at various pressures
25	Monocone	Nitrogen	P	Breakdown field vs. pressure
26	Monocone	Nitrogen	P	Breakdown field vs. $t_{eff}$ at various pressures
27	Monocone	Hydrogen	N	Breakdown field vs. pressure
28	Monocone	Hydrogen	N	Breakdown field vs. $t_{eff}$ at various pressures
29	Monocone	Hydrogen	P	Breakdown field vs. pressure
30	Monocone	Hydrogen	P	Breakdown field vs. $t_{eff}$ at various pressures
31	Monocone	SF6	N	Breakdown field vs. pressure
32	Monocone	SF6	N	Breakdown field vs. $t_{eff}$ at various pressures
33	Monocone	15% SF6/85% Air	N	Breakdown field vs. pressure
34	Monocone	15% SF6/85% Air	N	Breakdown field vs. $t_{eff}$ at various pressures
35	Monocone	15% SF6/85% Air	P	Breakdown field vs. pressure
36	Monocone	15% SF6/85% Air	P	Breakdown field vs. $t_{eff}$ at various pressures
37	Monocone	30% SF6/70% Air	N	Breakdown field vs. pressure
38	Monocone	30% SF6/70% Air	N	Breakdown field vs. $t_{eff}$ at various pressures
39	Monocone	30% SF6/70% Air	P	Breakdown field vs. pressure
40	Monocone	30% SF6/70% Air	P	Breakdown field vs. $t_{eff}$ at various pressures
41	Point-Plane	Nitrogen	N	Breakdown field vs. pressure
42	Point-Plane	Nitrogen	N	Breakdown field vs. $t_{eff}$ at various pressures
43	Point-Plane	Nitrogen	P	Breakdown field vs. pressure
44	Point-Plane	Nitrogen	P	Breakdown field vs. $t_{eff}$ at various pressures
45	Point-Plane	Hydrogen	N	Breakdown field vs. pressure
46	Point-Plane	Hydrogen	N	Breakdown field vs. $t_{eff}$ at various pressures
47	Point-Plane	Hydrogen	P	Breakdown field vs. pressure
48	Point-Plane	Hydrogen	P	Breakdown field vs. $t_{eff}$ at various pressures
49	Point-Plane	SF6	N	Breakdown field vs. pressure
50	Point-Plane	SF6	N	Breakdown field vs. $t_{eff}$ at various pressures
51	Point-Plane	15% SF6/85% air	N	Breakdown field vs. pressure
52	Point-Plane	15% SF6/85% air	N	Breakdown field vs. $t_{eff}$ at various pressures
53	Point-Plane	15% SF6/85% air	P	Breakdown field vs. pressure
54	Point-Plane	15% SF6/85% air	P	Breakdown field vs. $t_{eff}$ at various pressures
55	Point-Plan	30% SF6/70% air	N	Breakdown field vs. pressure
56	Point-Plan	30% SF6/70% air	N	Breakdown field vs. $t_{eff}$ at various pressures
57	Point-Plan	30% SF6/70% air	P	Breakdown field vs. pressure
58	Point-Plan	30% SF6/70% air	P	Breakdown field vs. $t_{eff}$ at various pressures

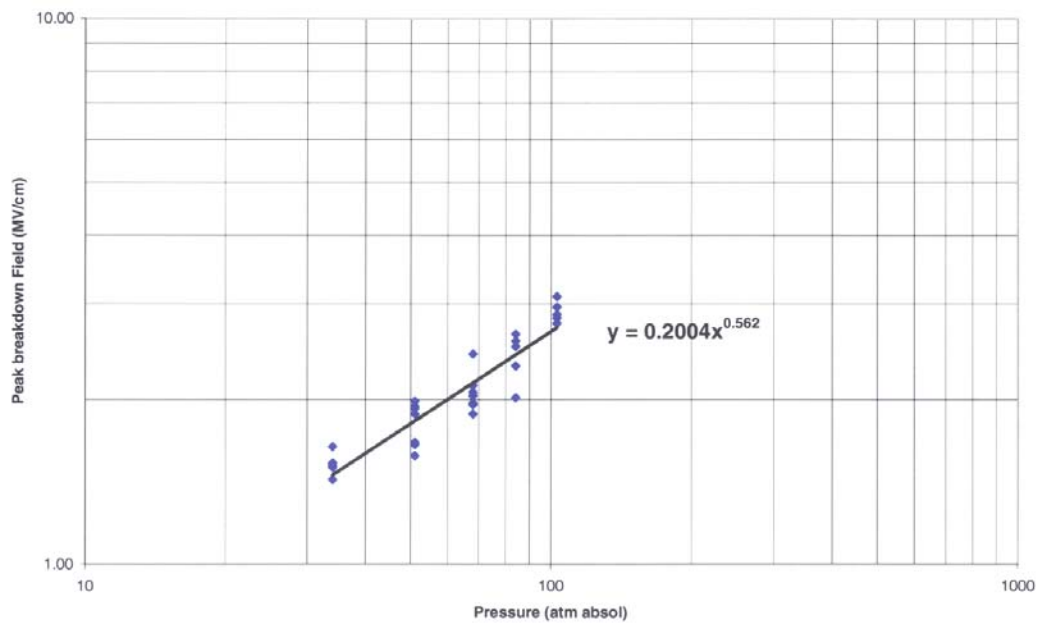


Figure 19. Monocone air negative polarity.

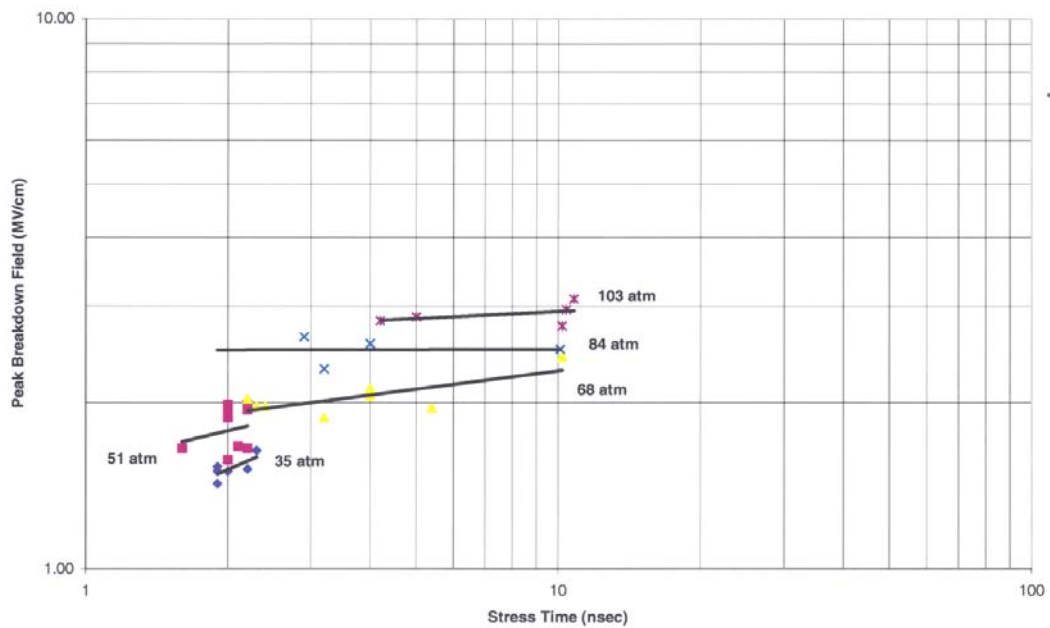
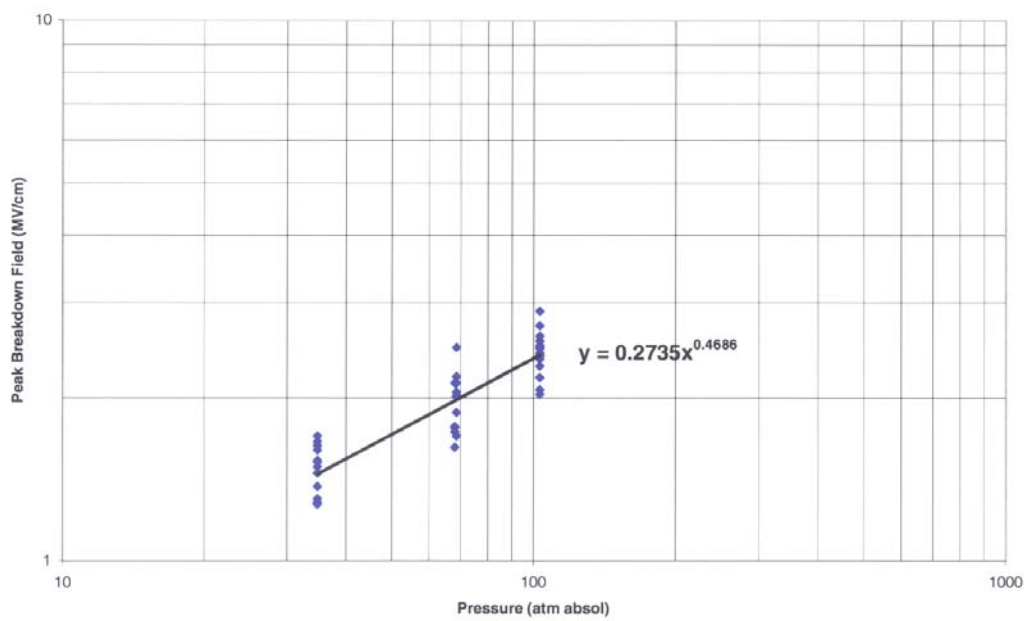


Figure 20. Monocone air negative polarity.



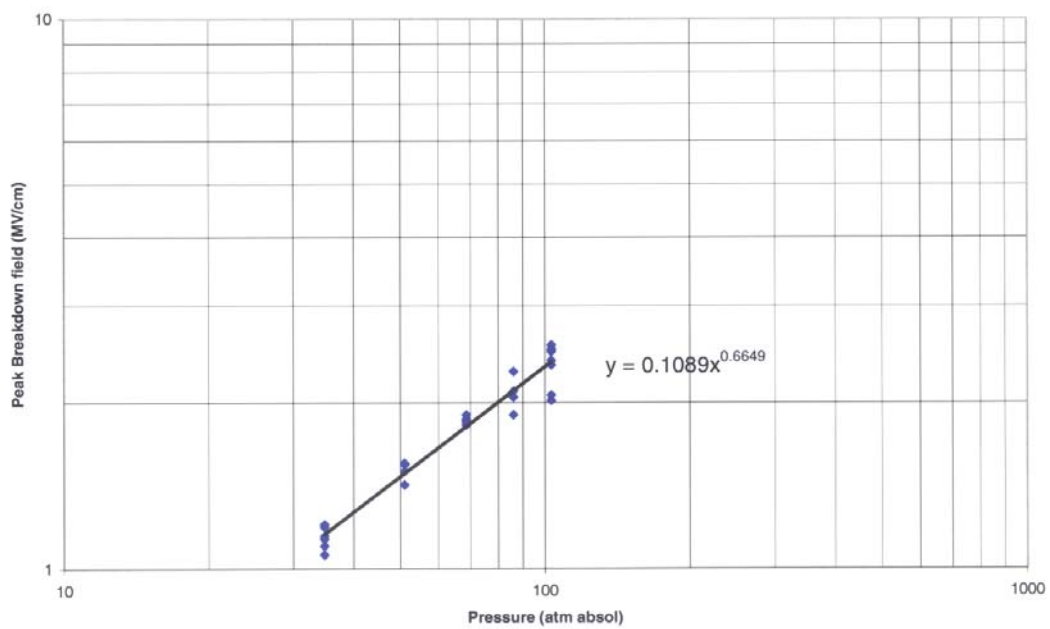


Figure 23. Monocone nitrogen negative polarity.

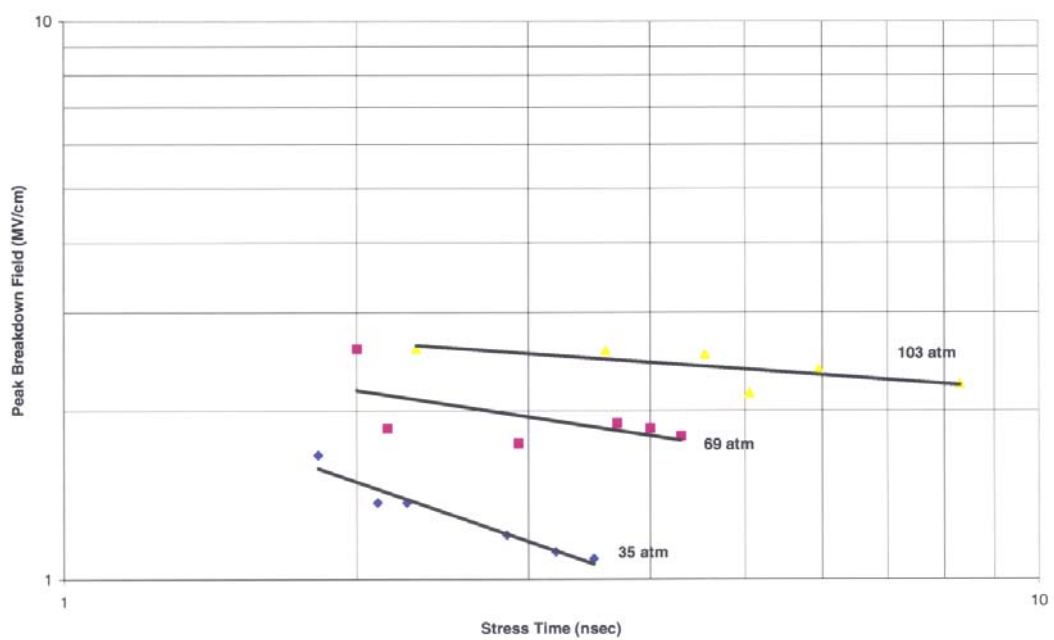


Figure 24. Monocone nitrogen negative polarity;.



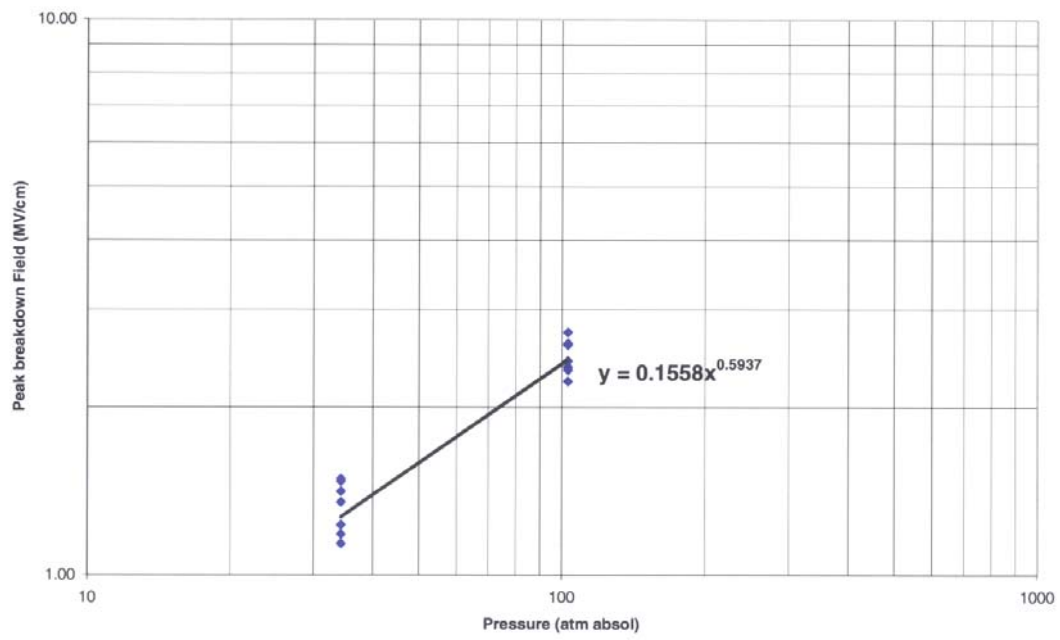


Figure 25. Monocone nitrogen positive polarity.

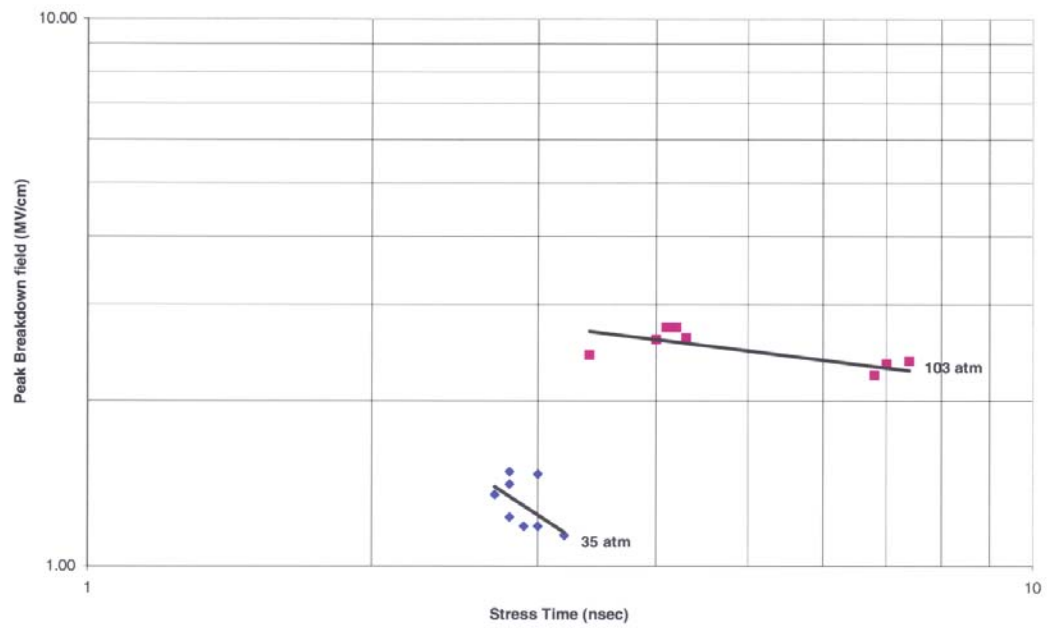


Figure 26. Monocone nitrogen positive polarity.

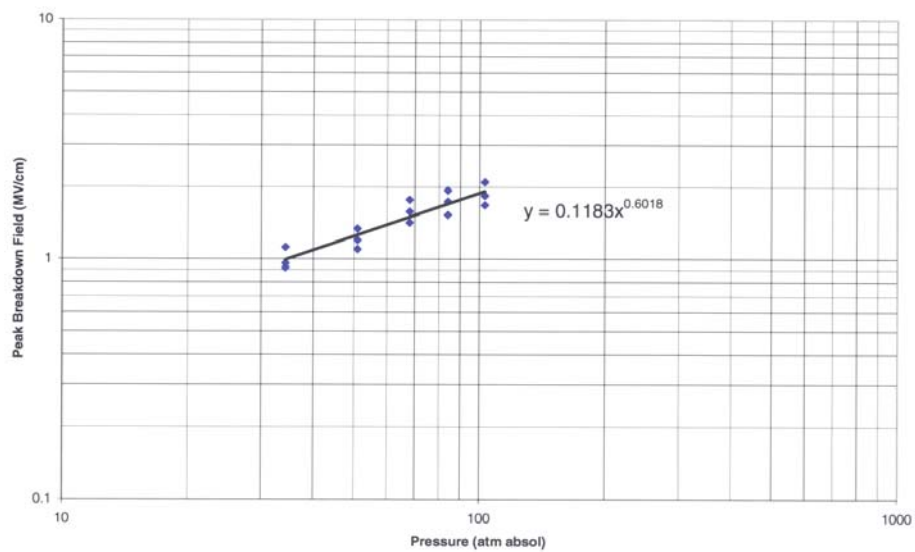


Figure 27. Monocone hydrogen negative polarity.

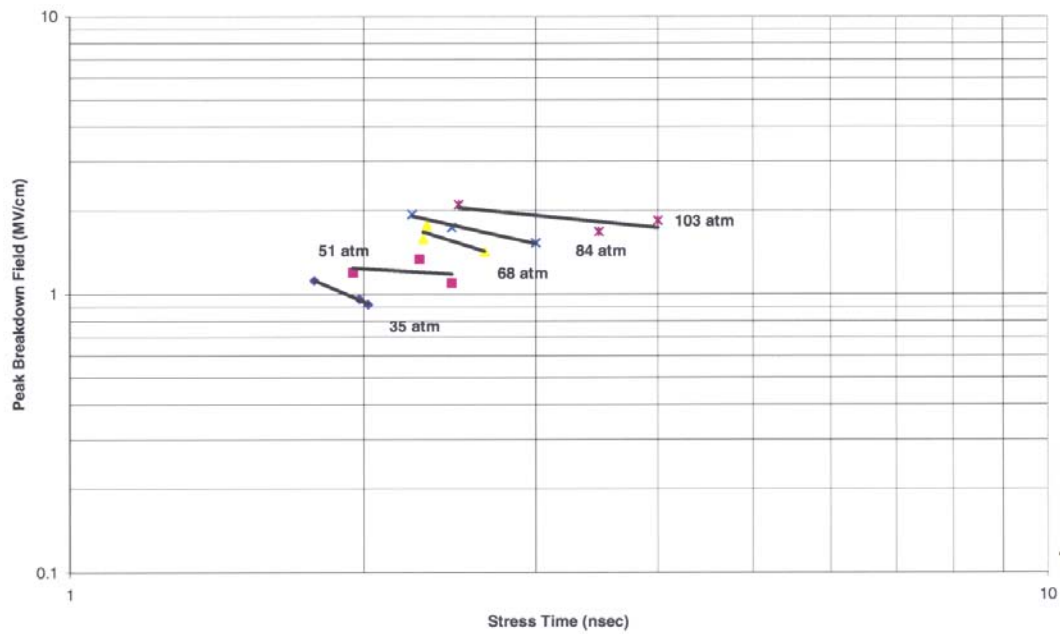


Figure 28. Monocone hydrogen negative polarity.

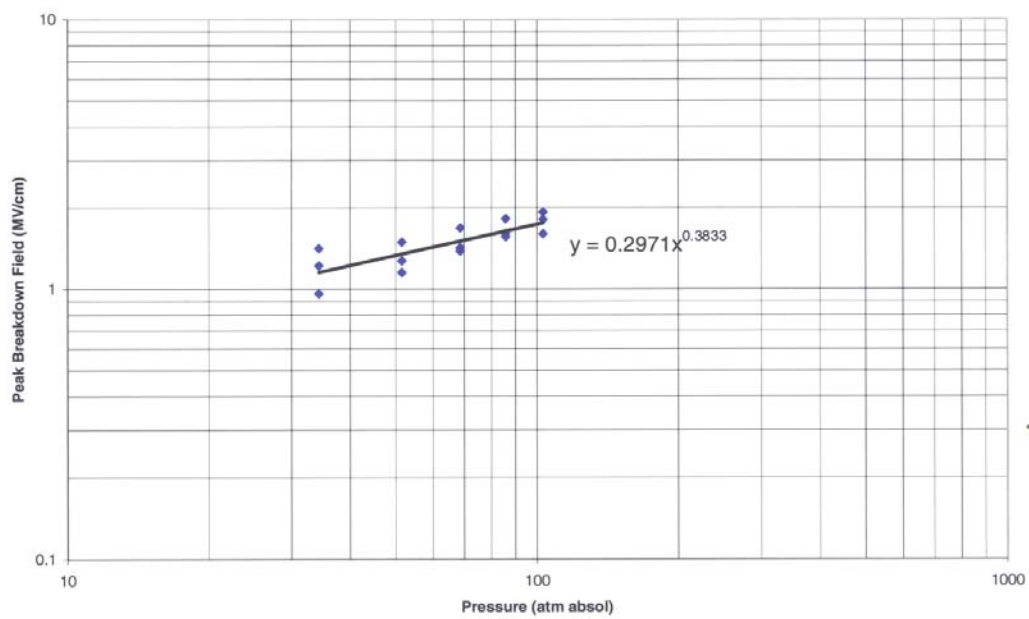


Figure 29. Monocone hydrogen positive polarity.

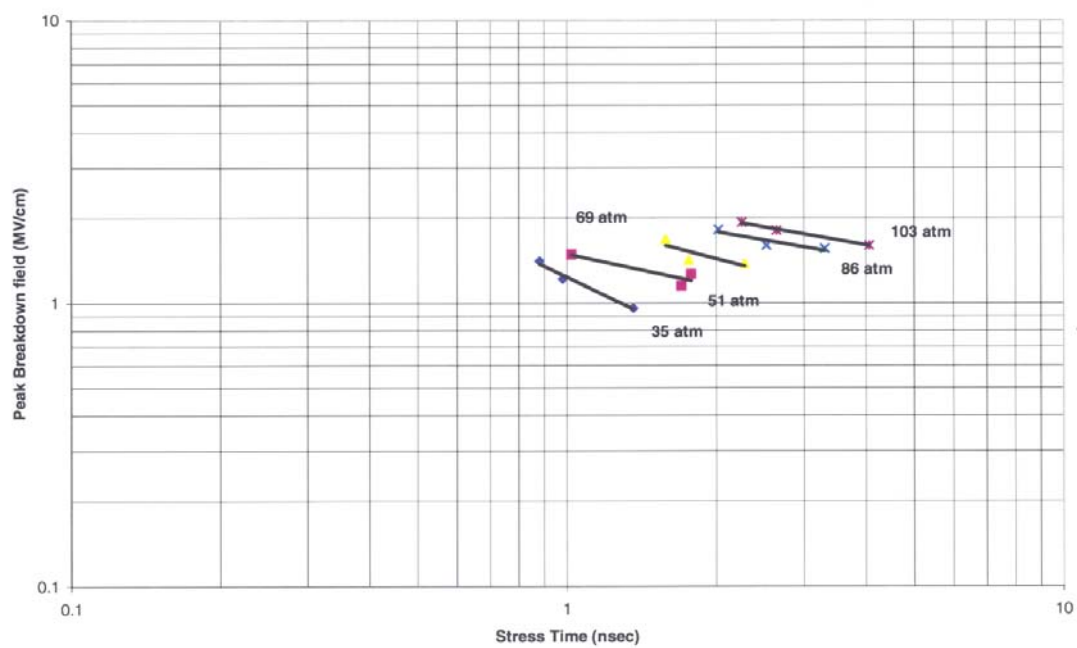


Figure 30. Monocone hydrogen positive polarity.

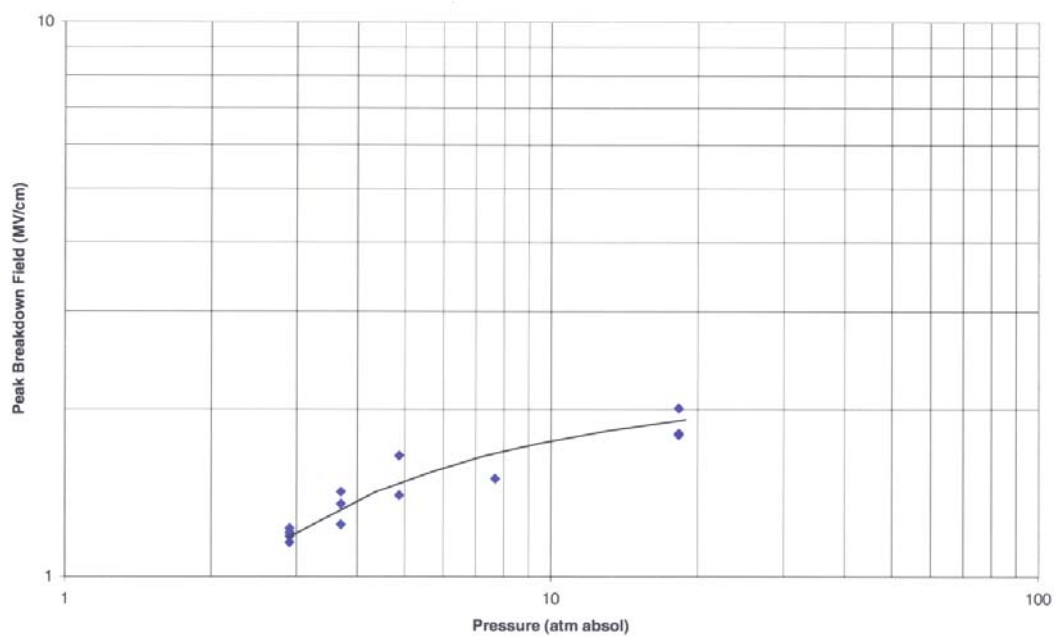


Figure 31. Monocone SF6 negative polarity.

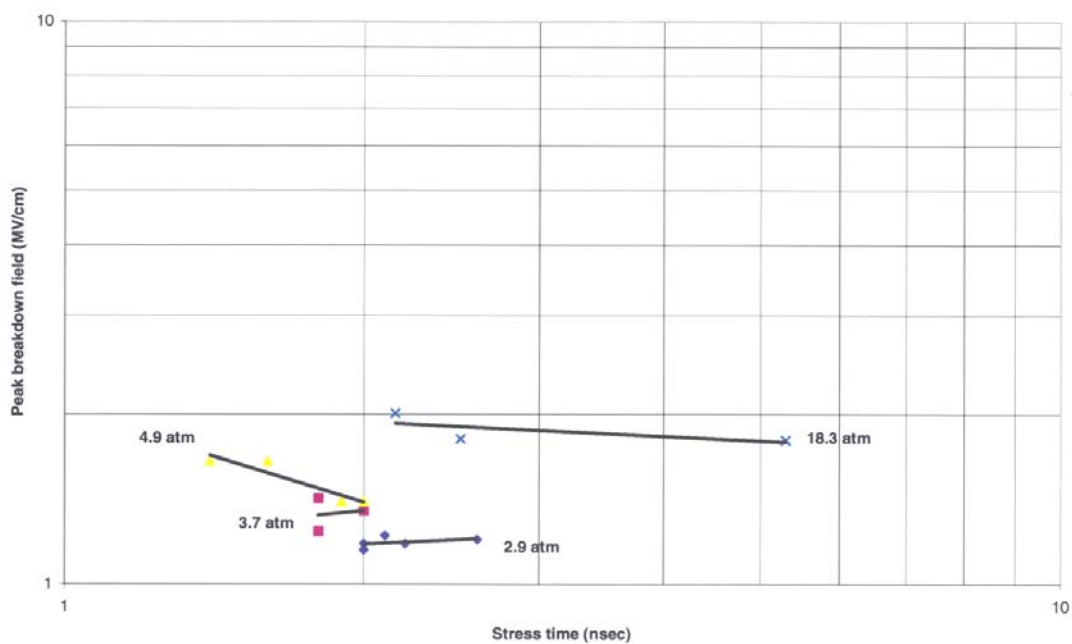


Figure 32. Monocone SF6 negative polarity.

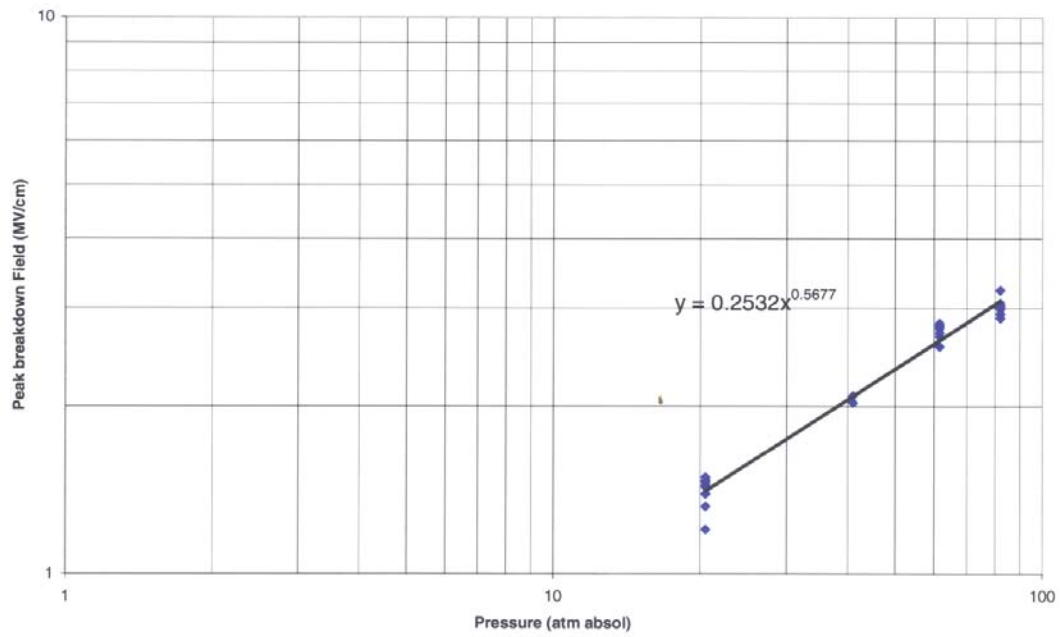


Figure 33. Monocone 15% SF6/85% air negative polarity.

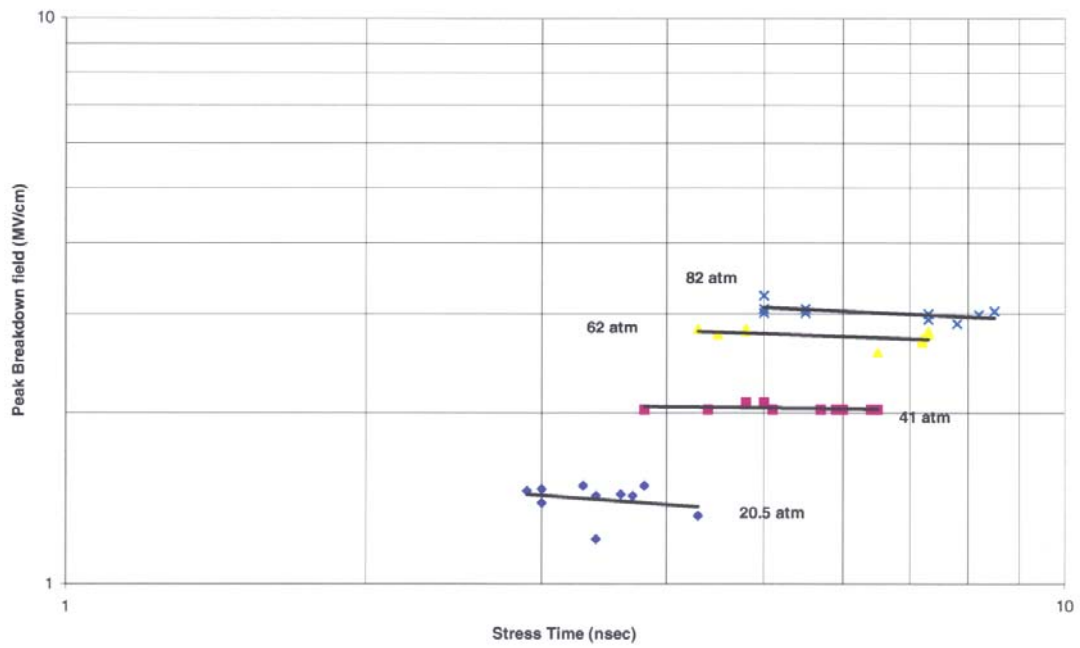


Figure 34. Monocone 15% SF6/85% air negative polarity.

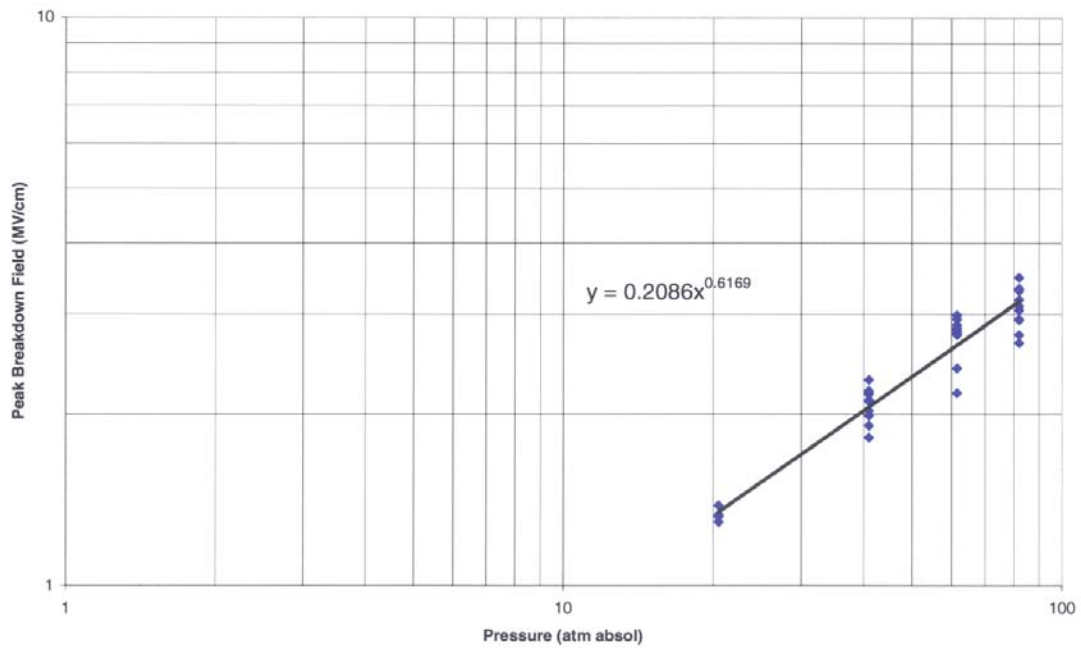


Figure 35. Monocone 15% SF6/85% air positive polarity.

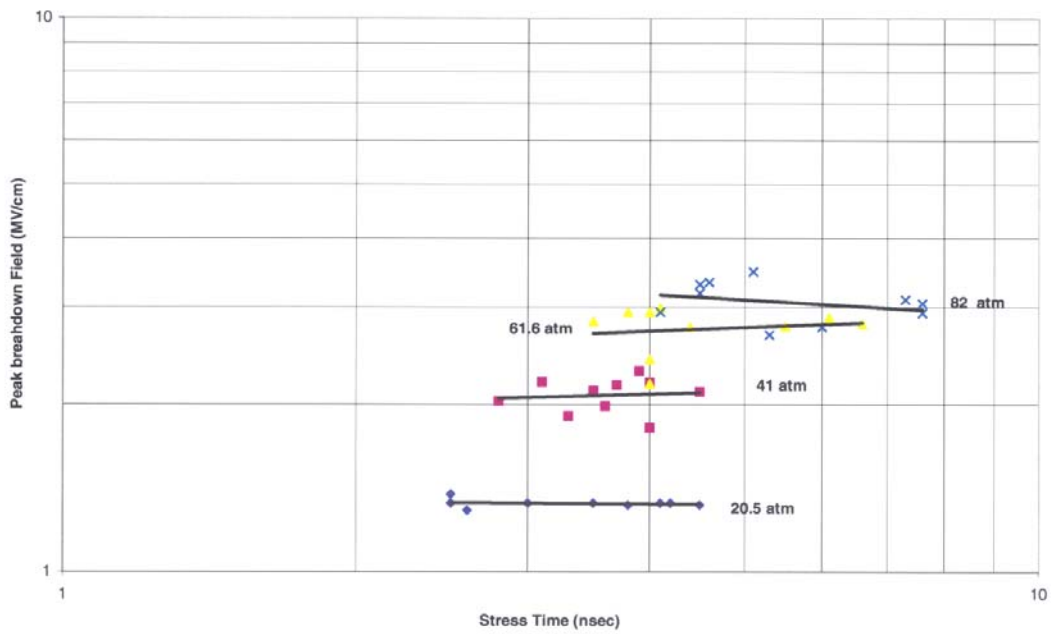


Figure 36. Monocone 15% SF6/85% air positive polarity.

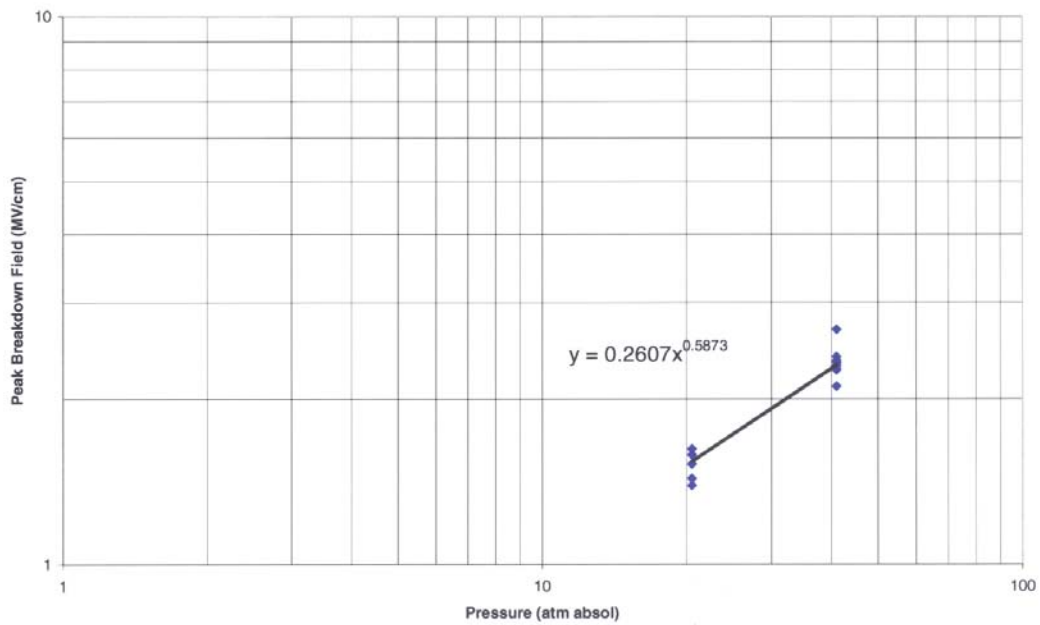


Figure 37. Monocone 30% SF6/70% air negative polarity.

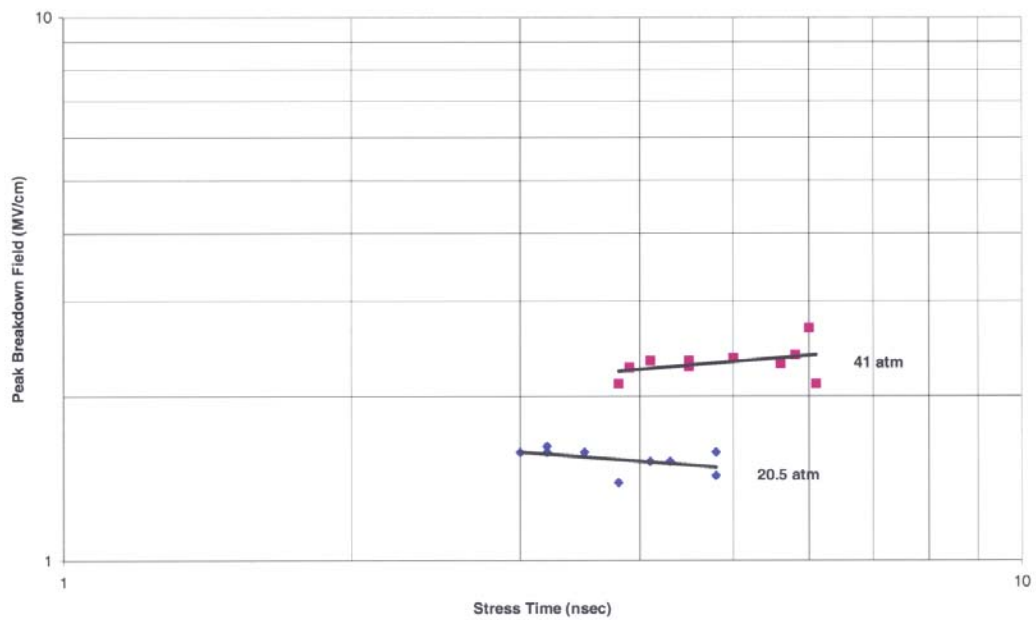


Figure 38. Monocone 30% SF6/70% air negative polarity.

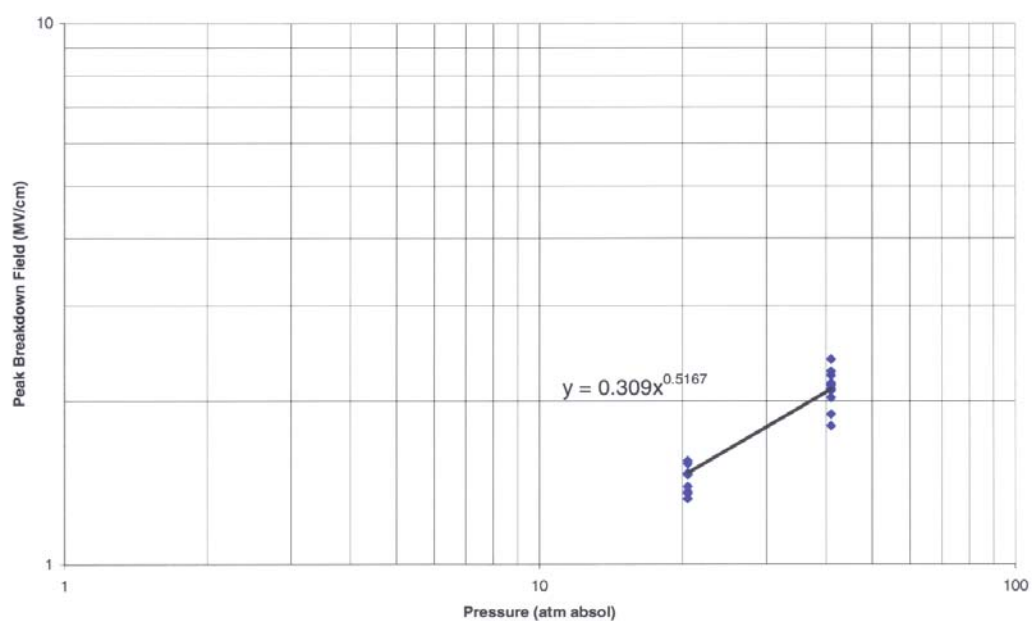


Figure 39. Monocone 30% SF6/70% air positive polarity.

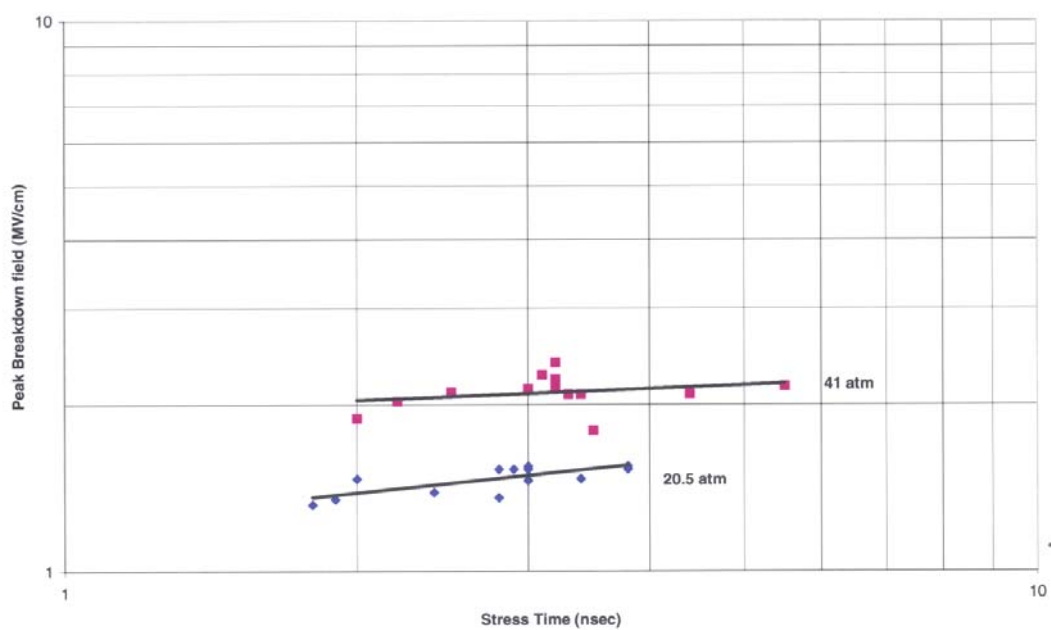


Figure 40. Monocone 30% SF6/70% air positive polarity.



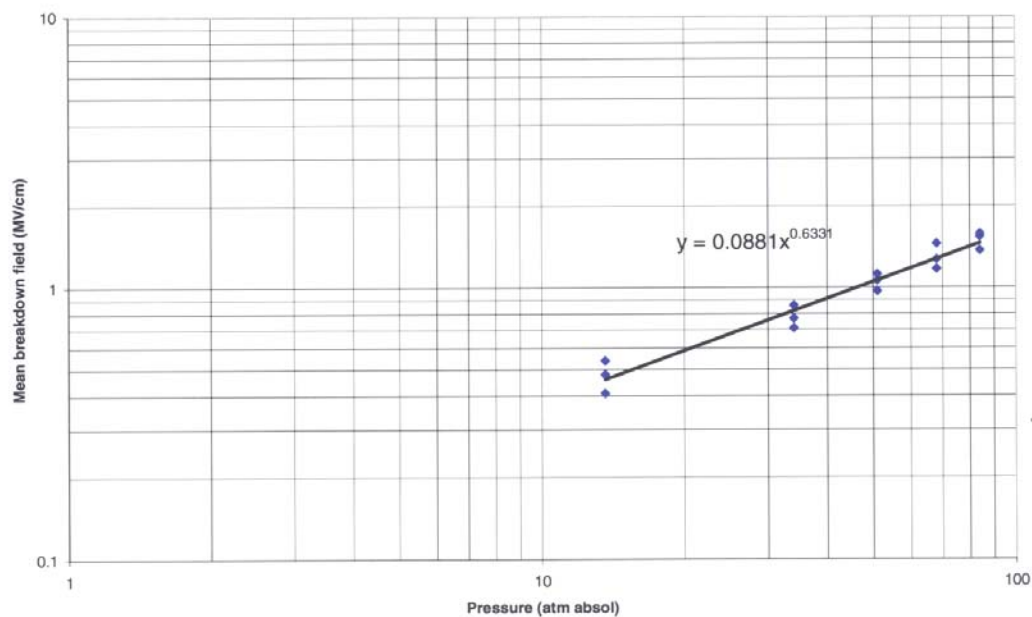


Figure 41. Point plane nitrogen negative polarity.

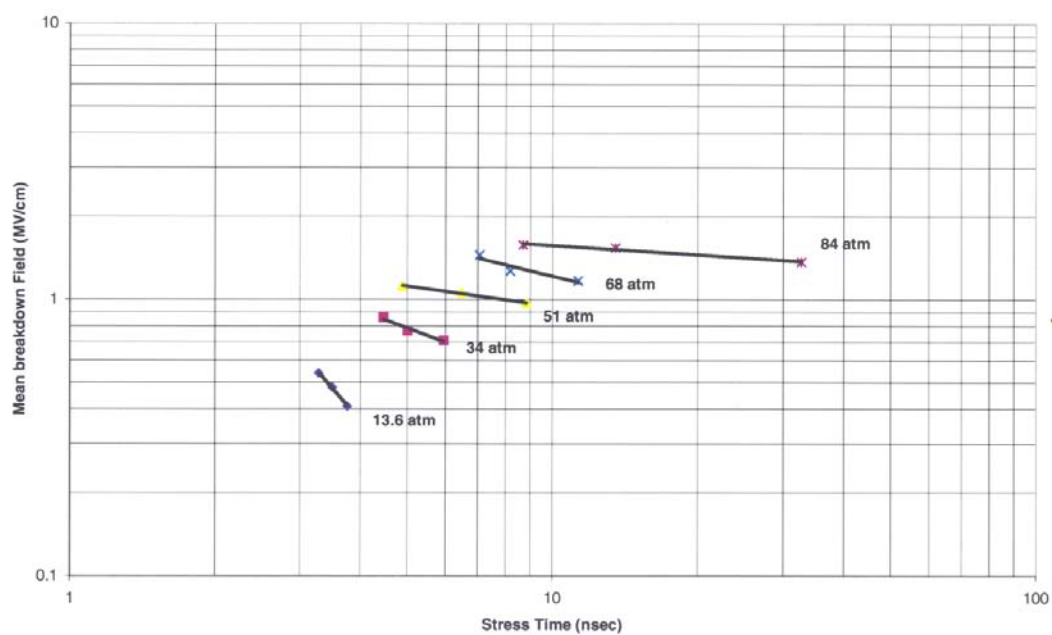


Figure 42. Point plane nitrogen negative polarity.

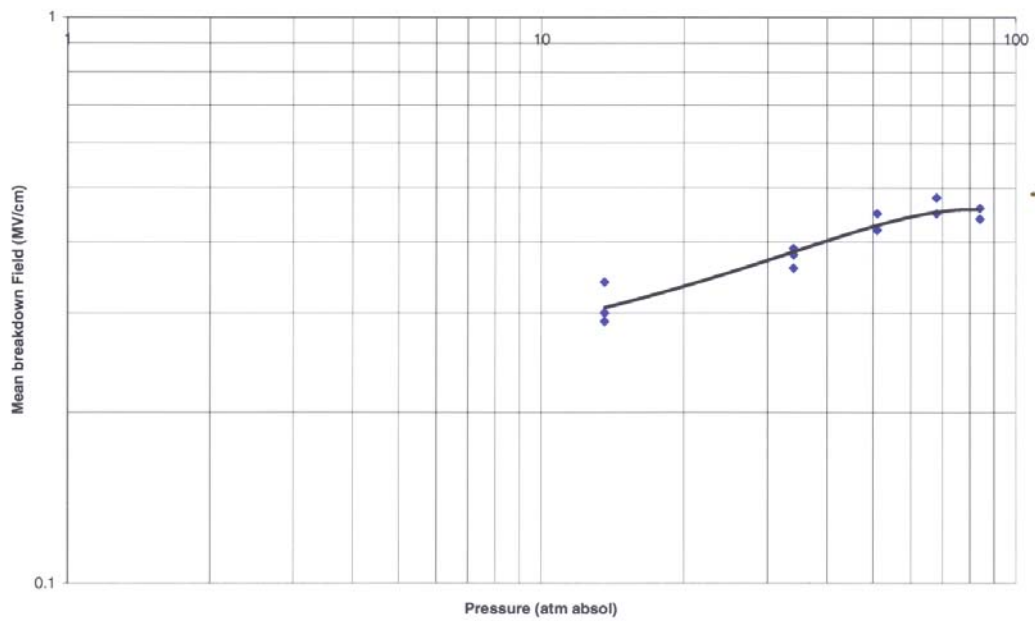


Figure 43. Point plane nitrogen positive polarity.

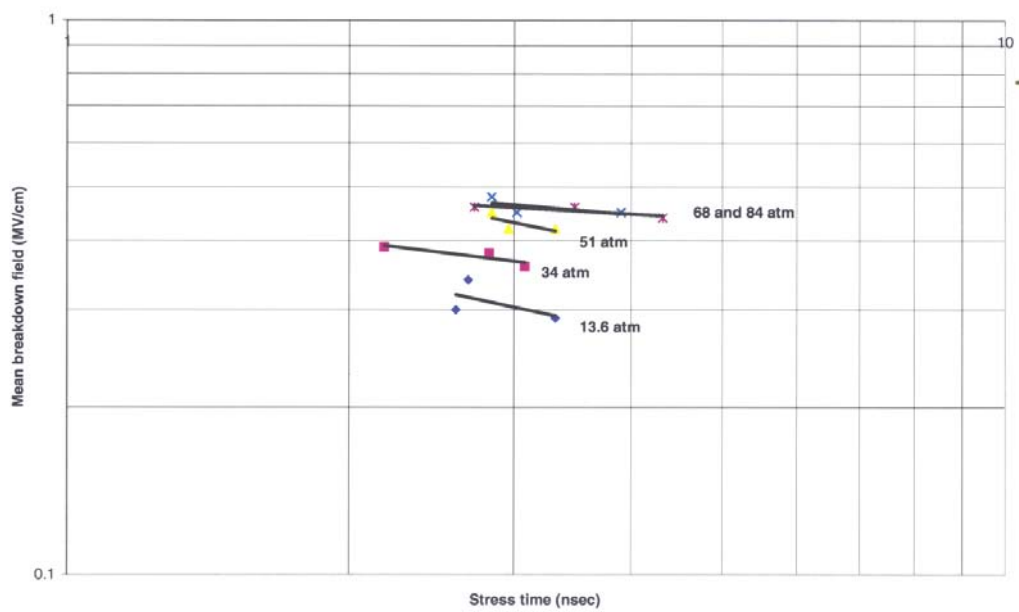


Figure 44. Point plane nitrogen positive polarity.

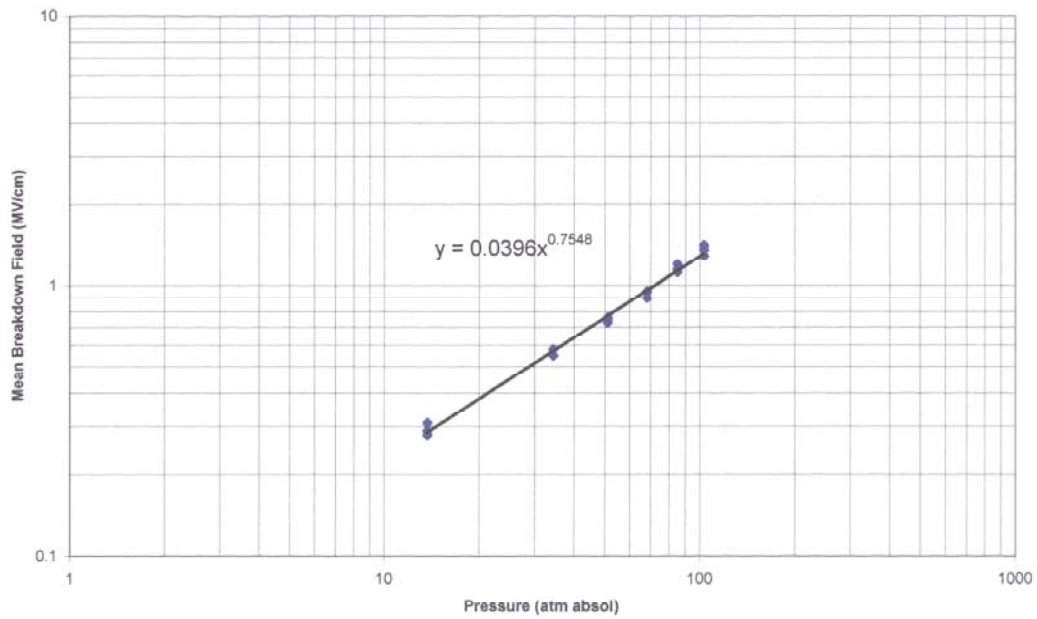


Figure 45. Point plane hydrogen negative polarity.

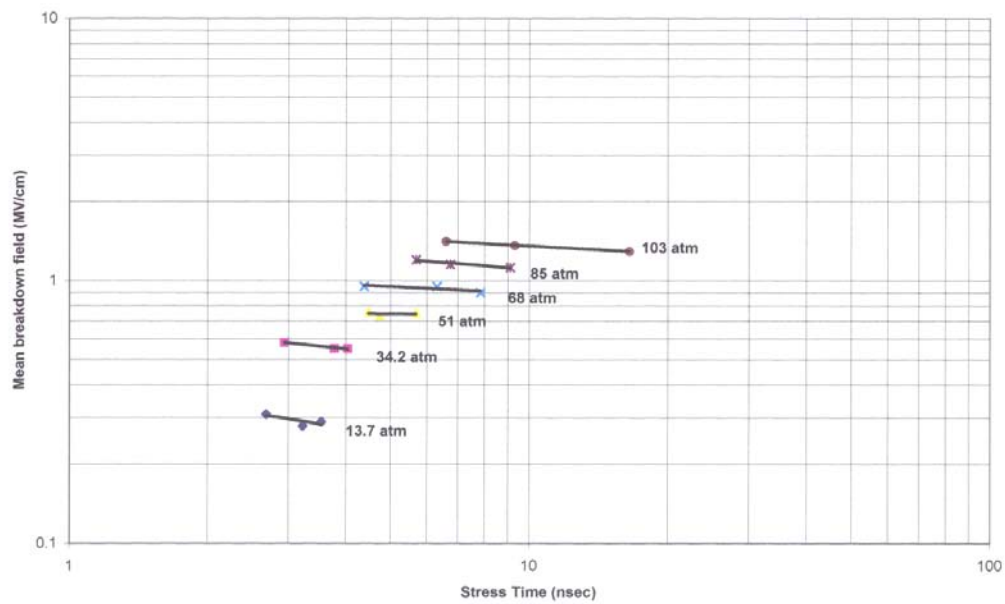


Figure 46. Point plane hydrogen negative polarity.

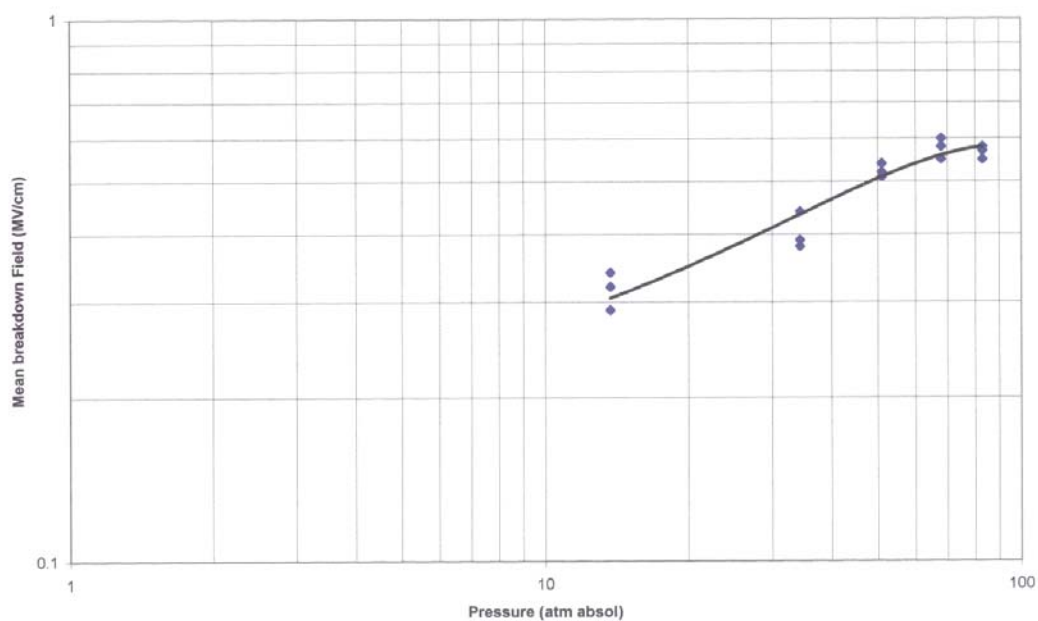


Figure 47. Point plane hydrogen positive polarity.

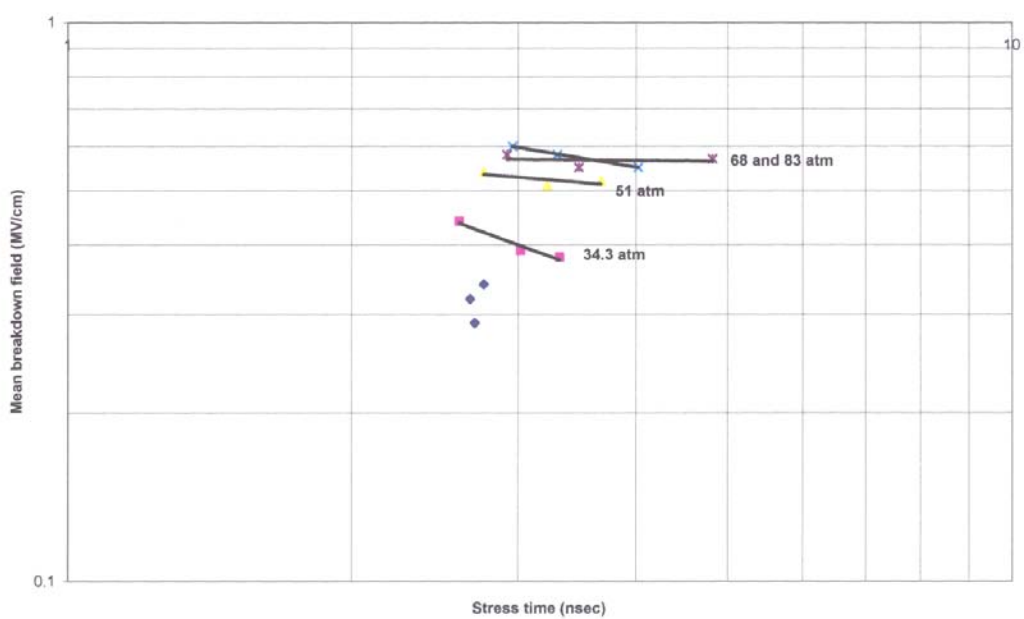


Figure 48. Point plane hydrogen positive polarity.

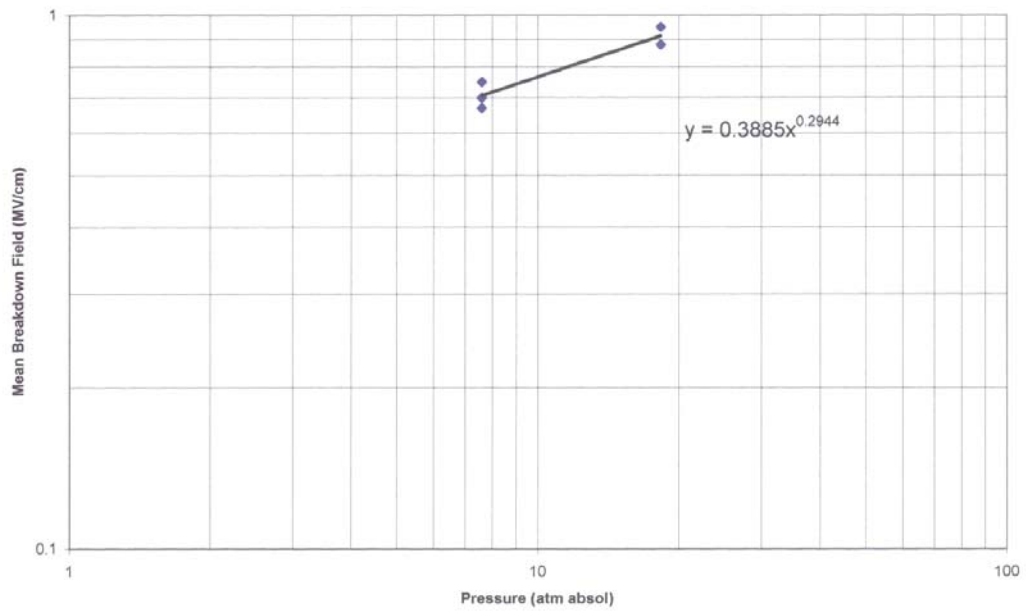


Figure 49. Point plane SF6 negative polarity.

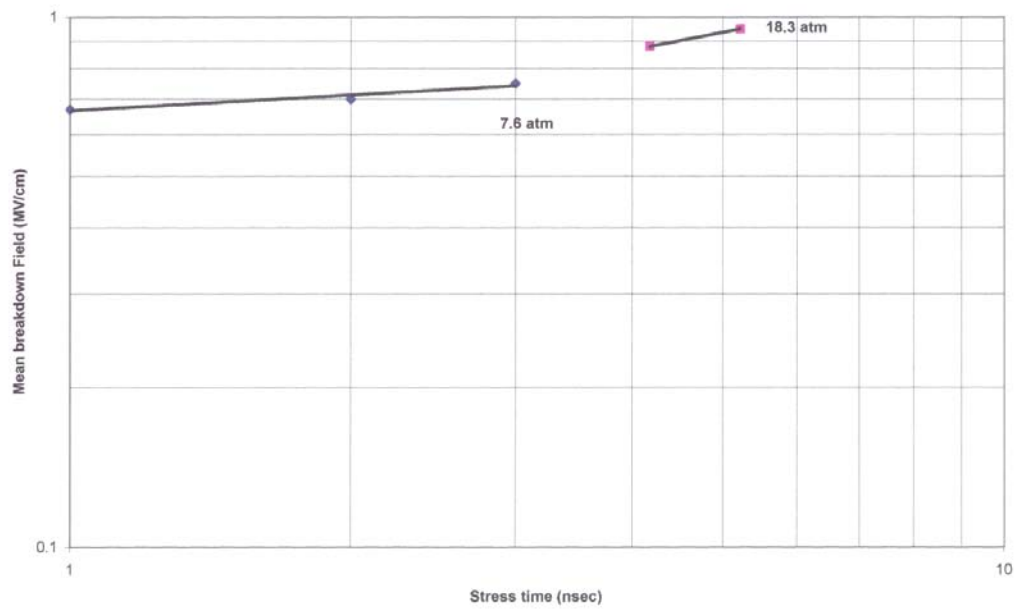


Figure 50. Point plane SF6 negative polarity.

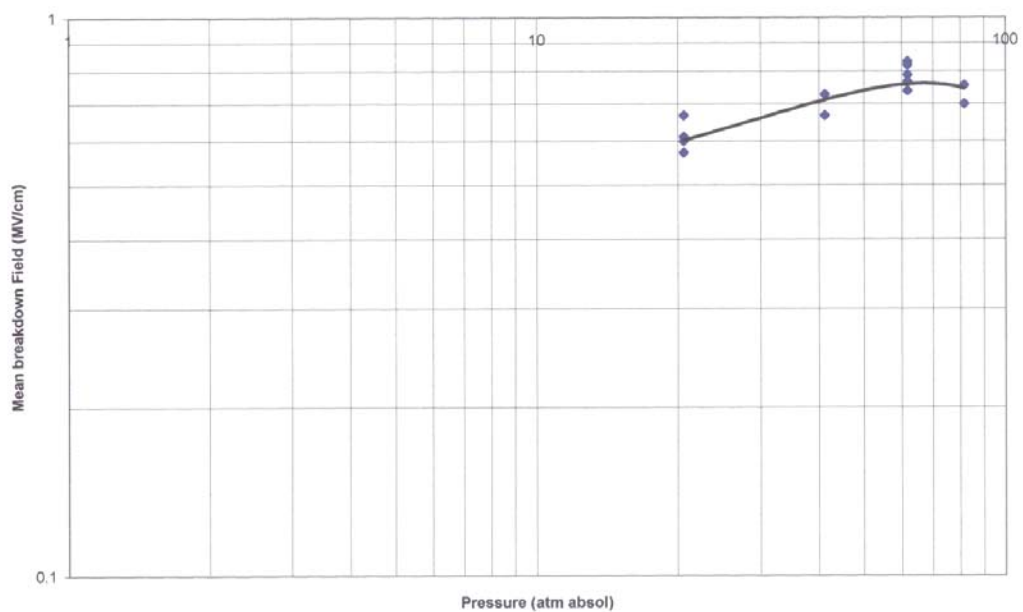


Figure 51. Point plane 15% SF6/85% air negative polarity.

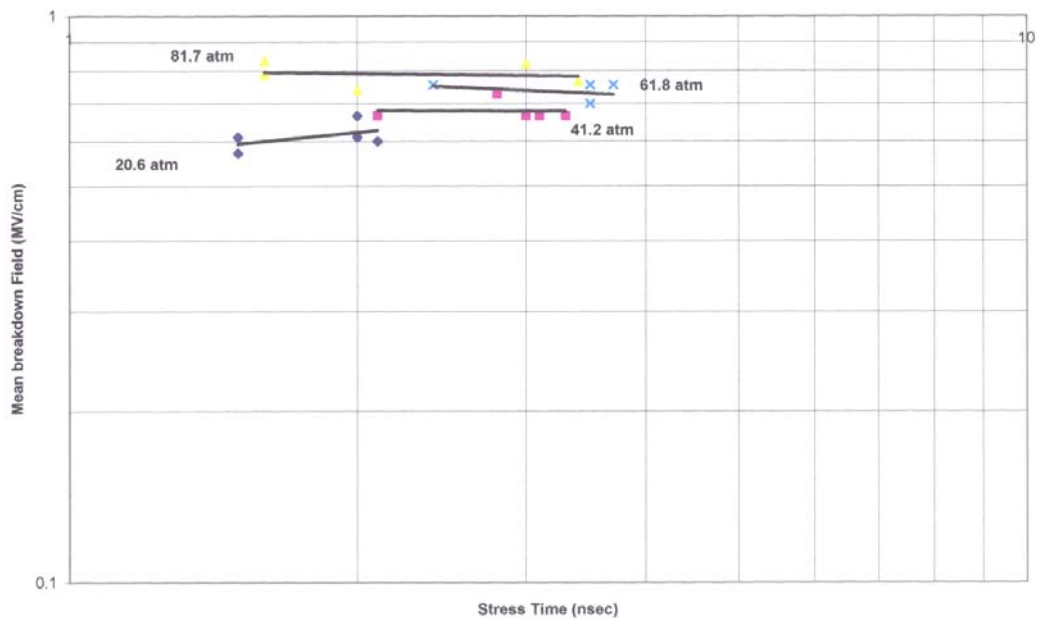
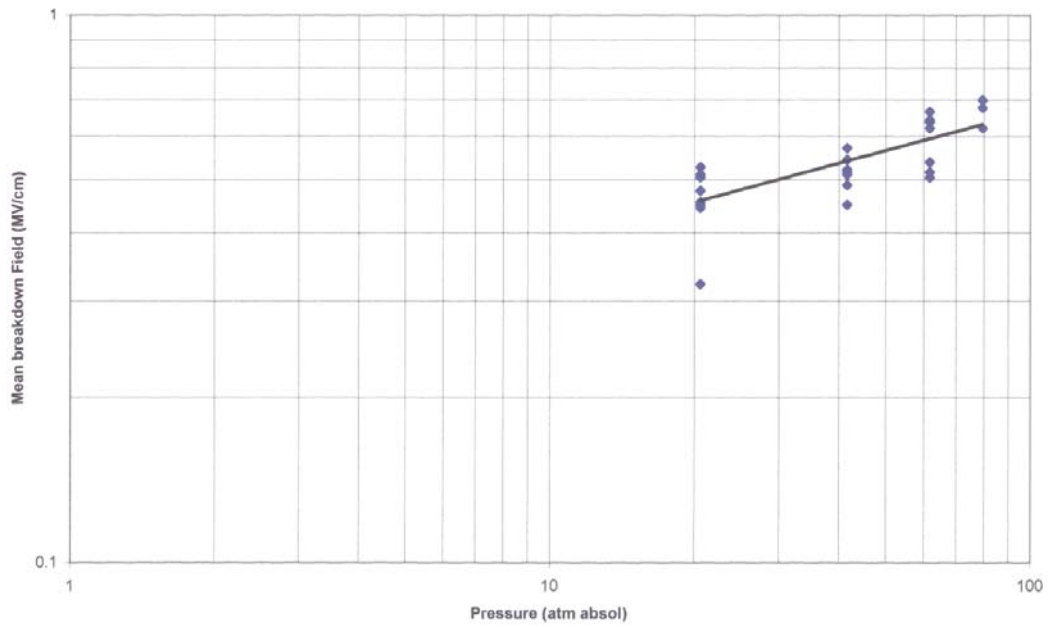
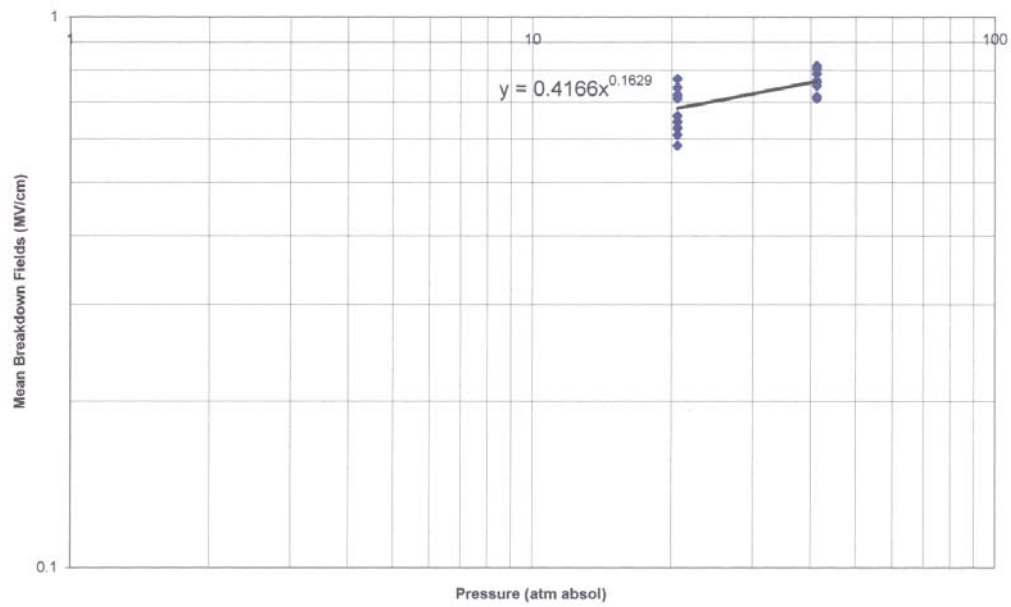
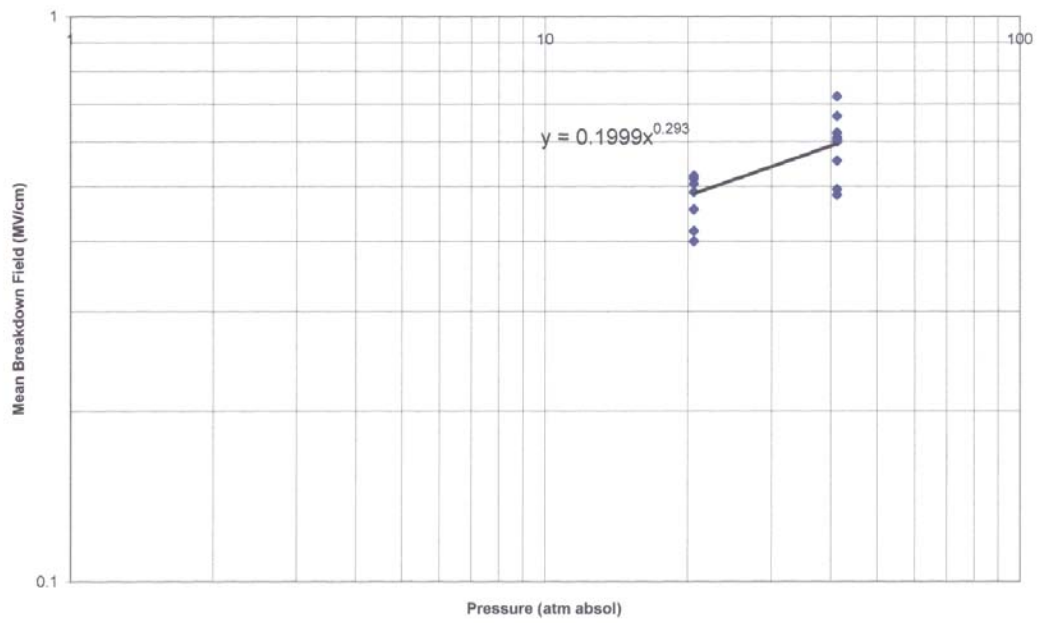


Figure 52. Point plane 15% SF6/85% air negative polarity.









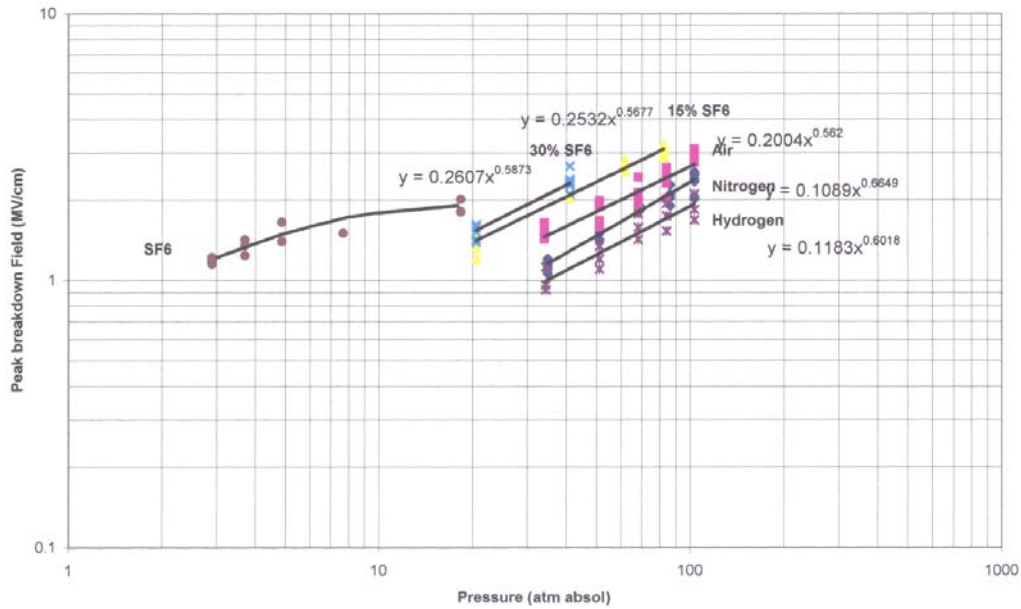


Figure 59. Monocone negative breakdown for all gases.

Table 3. Pressure dependency of monocone breakdown field.

Gas Type	Negative Polarity Pressure Scaling Exponent n Where $F=Kp^n$	Positive Polarity Pressure Scaling Exponent n Where $F=Kp^n$
Air	0.56	0.47
Nitrogen	0.66	0.60
Hydrogen	0.60	0.40
15% SF6/85% Air	0.57	0.62
30% SF6/70% Air	0.59	0.51

A pressure dependency of  $p^{0.7}$  is generally used for scaling the gas breakdown fields for the more normally used pressure ranges of  $\leq 10$  atmospheres. The weaker dependencies observed at the higher pressures used here may simply be due to the tendency for the breakdown fields to slowly roll off at these higher pressures.

A comparison of the breakdown fields of the tested gases in the monocone geometry is shown in Table 4 for the pressures indicated. Both peak and mean fields are listed.

At a common pressure of 85 atmospheres and based on air breakdown being 100%, nitrogen breakdown is 88%, hydrogen breakdown is 71% and the 15% SF6 mix breakdown is 127%. Nitrogen breakdown should be 10% or so higher than air according to published data, so the result reported here is a little surprising. Whether this is due to errors in the measurements or something related to the higher pressure and shorter stress time ranges used here is not known.

It should be noted that SF6 liquefies at about 20 atmospheres at room temperature and thus the pressure was limited to about 18 atmospheres. The 30% SF6 mix pressure was limited to about

41 atmospheres and the 15% was limited to about 85 atmospheres due to the partial pressures of SF6 causing them to liquefy at pressures somewhat higher than these pressures.

**Table 4. Summary of breakdown field strengths for the mildly-enhanced monocone gap.**

Gas	Pressure (atm. absolute)	Polarity	Peak Breakdown Field (MV/cm)	Mean Breakdown Field (MV/cm)
SF6	18.3	Neg	1.86	1.35
Air	85	Neg	2.40	1.74
Air	85	Pos	2.15	1.56
N2	85	Neg	2.10	1.52
N2	85	Pos	2.10	1.52
H2	85	Neg	1.70	1.23
H2	85	Pos	1.65	1.20
15% SF6/85% Air	85	Neg	3.05	2.21
15% SF6/85% Air	85	Pos	3.10	2.25
30% SF6/70% Air	41	Neg	2.25	1.63
30% SF6/70% Air	41	Pos	2.05	1.49

It is evident that with moderate electrode enhancement, the differences between the positively and negatively enhanced electrode breakdown fields are slight. The differences are less than 10% for air, nitrogen, hydrogen and the SF6 mixes. No data is available for the SF6 in the positive polarity.

## 2.2.2 New Uniform Field Breakdown Dependency on Stress Time

The breakdown field dependency on the voltage stress time for the gases tested tended to be strongest at the lower pressures near 30 atmospheres and diminished and in some cases disappeared as the pressure was raised towards 100 atmospheres. This is shown in the appropriate plots of breakdown field versus stress time in Figures 19 to 58.

For example, in the monocone tests using hydrogen in the positive polarity (Figure 28) at 34 atmospheres, the breakdown field dependency on stress time ( $t$ ) followed the relationship  $t^{-0.85}$  while at 103 atmospheres it was  $t^{-0.31}$ . Similar trends were observed in both the mildly-enhanced monocone and point-plane cases. There are only a few exceptions to this observed trend.

Negative air breakdown in the monocone geometry is one notable exception where the breakdown seems to increase with longer stress times. Similar exceptions occur in the 30% SF6 mix, monocone, and the negative point-plane SF6 cases. These are not expected results based on theoretical arguments and probably are due to general measurement errors and errors introduced by the short ranges of stress times tested. One possible explanation is that the slow rise of voltage could lead to more stable shielding by corona.

However, the observance of this tendency for the breakdown field dependency on time to diminish as the pressure increases in the vast majority of the test results would seem to suggest that this tendency is indeed real.

The weaker breakdown field dependency on time at higher pressures can possibly be explained in terms of the formative time of the gap. The formative time of a gap is the time that streamer growth develops just prior to the gap closing. Figure 60 illustrates the concept of formative time. When the static breakdown field of a gap is reached at a time  $t_1$  after a pulse is applied, there is a delay time  $t_2 - t_1$  during which free electrons must appear and begin the avalanche process that leads to the ultimate closure of the gap.

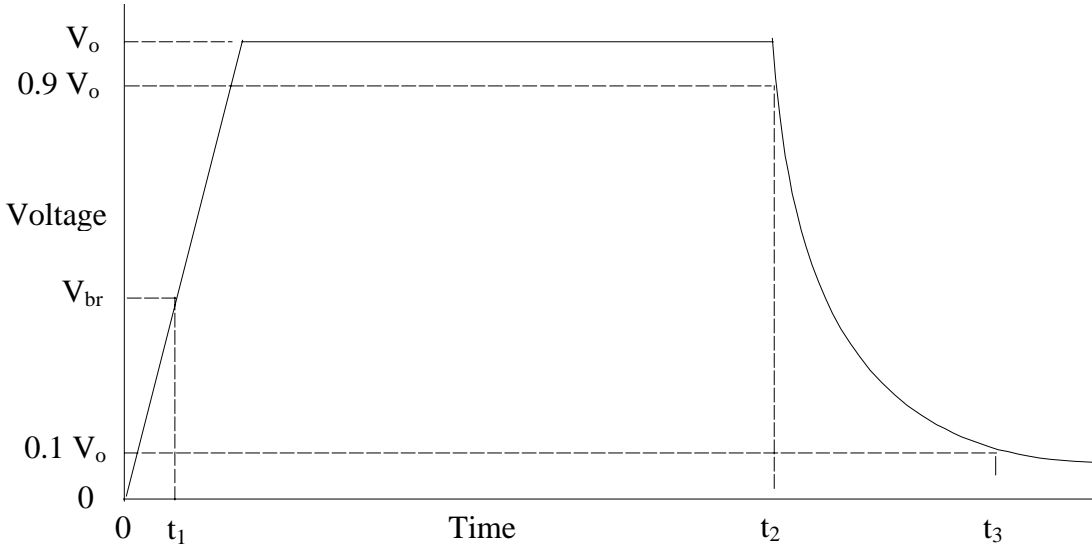


Figure 60. Breakdown delay time.

Within this delay time, ionization and electrode emission processes produce free electrons. The electrons appear not instantaneously but in some statistical manner which contributes to the jitter of the closing gap. Once the free electrons appear, the avalanche and streamer generation processes take over and eventually the gap closes. This time duration during which the actual avalanching and streamer generation process occurs is referred to as the formative time. The formative time is a function of gas type, pressure, field level, and other factors.

Representative formative times reported in the literature for gaps operating in the regimes studied in these reported tests can be in the range of one to many tens of nanoseconds with higher pressures and higher fields producing the shortest formative times. If a gap is charged rapidly enough, the gap will be able to be charged to a significantly higher voltage than its static breakdown field before it finally breaks down. The over-voltage is related to the  $dV/dt$  of the pulse and how much more voltage rise occurs during the formative time lapse.

In the gas tests, the stress times were typically approximately 1 to 5 ns, resulting from charge times of 5-20 ns. These charge times were well over the formative times for the high pressure, high field cases. Formative times under these conditions of high pressure and high fields were actually measured as 1-2 ns in the pulser tests that will be described in the section related to these tests.

On the other hand, although they were never measured in this program, the formative times at the low-end pressures can only be assumed based on the literature reports. Reported formative times under these conditions can be tens of nanoseconds.

When the formative time is much shorter than the range of charge times as it is at the high pressure, little over-voltage occurs during this formative time lapse even as the charge time decreases within this range. This results in little or no dependence of breakdown field on time as observed. Just the opposite effect occurs when the formative time is longer than the charge time as it is at the lower pressures.

It is interesting to note that if the plotted monocone breakdown field trend lines for the various pressures are extrapolated towards lower stress times, they seem to intersect at stress times in the range of 0.1 to 0.5 ns. An example of this is shown in Figure 61. This seems to imply that with a small enough stress time the breakdown fields are independent of pressure. The stress times where these plotted lines intersect represent charge times of between 1 to 5 ns that coincidentally seem to be typical formative times at 100 atmospheres and at high fields.

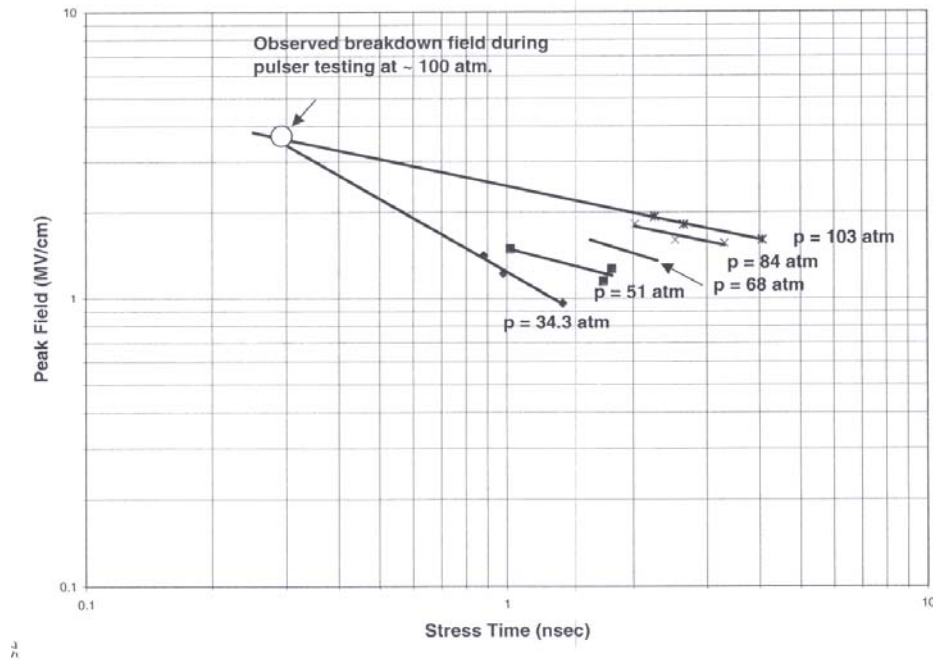


Figure 61. Hydrogen positive monocone tip.

Realistically, a gap hold off voltage independent of pressure even for very fast charge times does not seem feasible. The observed trends would ultimately end when the voltage and fields increase sufficiently to produce even shorter formative times and/or other mechanisms begin to dominate the gap breakdown.

We have evidence that the lower pressure breakdown fields must ultimately level-off as the stress times decrease. The actual measured breakdown field of the hydrogen filled output gap of the demonstration pulser is added to the plot in Figure 61. It shows that at 103 atmospheres and a very short stress time of about 0.3 ns the breakdown field falls on the extrapolated trend line for

103 atmospheres of hydrogen, which suggests that the trend continues to very small stress times. It was also observed that the gap broke down at lower voltages when the pressure was decreased thus confirming that the trend for the lower pressures does not continue indefinitely.

### 2.2.3 Point-Plane Breakdown

For a point-plane gap using nitrogen, hydrogen or either of the two SF6 mixes, the breakdown fields over the tested pressure range are generally weaker when the highly enhanced electrode is positive polarity as illustrated in Figures 62, 63 and 64. The only exception is hydrogen shown in Figure 62 where at 14.3 atmospheres the breakdown fields in both polarities are the same.

Further, the positively enhanced point-plane hydrogen and nitrogen fields peak out and begin to decrease at about 80 atmospheres (see Figure 62). With the same gap with negative enhancement the fields seem to continue to increase with pressure and not exhibit such a roll over.

The 15% SF6 mix behaves differently. Although the negatively enhanced field is still stronger than the positive, the negatively enhanced field rather than the positive is observed to peak out and roll over (see Figure 63). Insufficient 30% SF6 mix data precludes drawing any conclusion about its behavior.

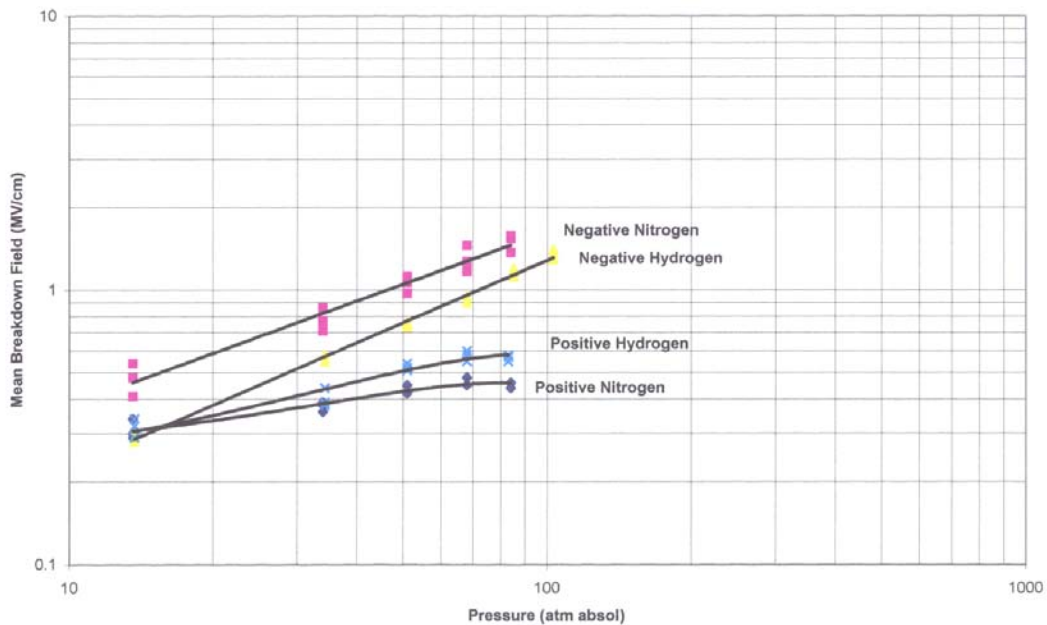


Figure 62. Point plane hydrogen and nitrogen.

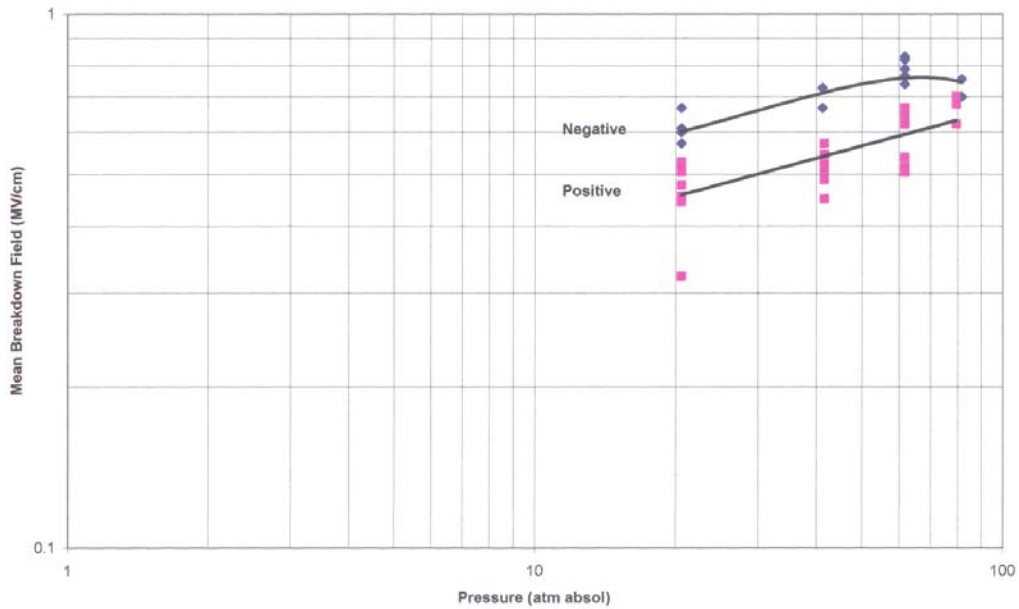


Figure 63. 15% SF6 point plane positive and negative.

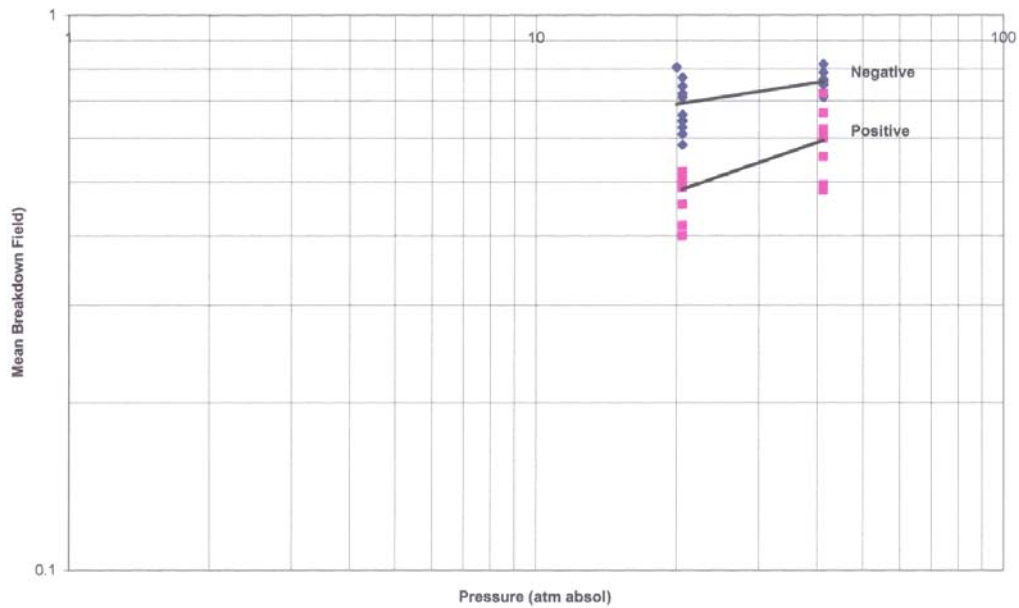


Figure 64. 30% SF6 point plane positive and negative.

Table 5 lists the point plane mean positive and negative breakdown fields for SF6, nitrogen, hydrogen and the SF6 mixes and compares them to one another and to the mean monocone breakdown fields.

Table 5. Summary of enhanced breakdown field strengths.					
1	2	3	4	5	6
Gas	Pressure (atm. Absolute)	Mean Breakdown Field (MV/cm) (Neg)	Mean Breakdown Field (MV/cm) (Pos)	Mean E(Pos)/E(Neg)	Mean (neg and pos) E(PP)/E(Uniform)
SF6	14.3	0.92	-----	-----	0.71(Neg)
N2	14.3	0.46	0.31	0.67	
N2	85	1.4	0.47	0.34	0.85 (Neg) / 0.30 (Pos)
H2	14.3	0.29	0.31	~1	
H2	85	1.25	0.59	0.47	~1 (Neg) / 0.5 (Pos)
15% SF6/ 85% Air	21	0.60	0.45	0.75	
15% SF6/ 85% Air	80	0.78	0.49	0.79	0.35 (Neg) / 0.28 (Pos)
30% SF6/ 70% Air	21	0.68	0.49	0.72	
30% SF6/ 70% Air	41	0.76	0.60	0.79	0.47 (Neg) / 0.40 (Pos)

For nitrogen and hydrogen the polarity effect for an enhanced geometry is more apparent at higher pressures. Column 6 in Table 5 compares the mean field breakdown levels. For nitrogen with a positively-enhanced electrode, the mean breakdown field at a pressure of 14.3 atmospheres is about 67% of the mean field with the negatively-enhanced electrode. At 85 atmospheres the positively enhanced mean breakdown field drops to 34% of that with negative enhancement.

For hydrogen at 14.3 atmospheres, the positively enhanced mean field is approximately equal to that with negative enhancement. At 85 atmospheres the positive mean field drops to 47% of that with negative enhancement.

For the SF6 mixes, the ratio of positive to negative enhanced field breakdown is approximately 72-79% over the entire pressure ranges tested.

For nitrogen and hydrogen and even pure SF6, the point plane geometry with the enhanced electrode charged negative seems to only moderately degrade the mean breakdown fields when compared to the mildly enhanced monocone. Column 6 of Table 5 compares the point plane and near-uniform field breakdown. The results indicated that the mean fields with nitrogen at 85 atmospheres are reduced to 85%, and the mean fields with hydrogen at 85 atmospheres showed no degradation. With SF6 operating at 14.3 atmospheres, the mean breakdown fields are reduced to 71%.

When the enhancement is charged positive, the breakdown fields are dramatically decreased when compared to the mildly enhanced monocone gap. At 85 atmospheres the mean breakdown field drops quite dramatically to 50% and less of the monocone mean field for the nitrogen, hydrogen and the SF6 mixes.



## 2.2.4 Resistive Phase Risetime

Risetime data was obtained for the near-uniform field configurations for nitrogen and hydrogen as well as the SF6 mixes. The data is summarized in Table 6.

The risetimes and breakdown fields were measured for nitrogen and hydrogen at pressures of 85 and 34.3 atmospheres. Similar measurements were made for the 15% SF6 mix at pressures of 82.4 and 21 atmospheres and for the 30% mix at 41 and 21 atmospheres.

An SCD 5000 4.5 GHz oscilloscope was used with the previously described D-dots. The risetime of the measurement system, which included the cables and DC11 delay line was estimated to be 100 psec. Measured risetimes were corrected for the measurement system risetime by using quadrature subtraction and the resulting corrected risetimes are tabulated in column 6 of Table 6. Because the measured risetimes include both inductive and resistive phase contributions, these must be separated. Estimating an inductance of the arc channel using approximately 12 nH/cm for the 0.091 cm gap and using Equation 4 resulted in a risetime associated with the inductance that is listed in column 7. Subtracted this out in quadrature from the corrected measured risetime results in the estimated resistive phase risetime component, which is shown in column 8 of Table 6.

Applying the resistive phase formula in Equation 2 and using the measured breakdown fields and pressures, the calculated risetimes are shown in column 9.

Table 6. Monocone risetime data summary.								
<u>1</u> <b>Gas</b>	<u>2</u> <b>Polarity</b>	3 Pressure Absol atm	4 Breakdown Field MV/cm	5 Measured Risetime psec	6 Corrected Risetime <sup>1</sup> psec	7 Est. Inductive Risetime <sup>2</sup> psec	8 Imputed Resistive Phase Risetime <sup>3</sup> nsec	9 Calculated Resistive Phase Risetime nsec
N2	N	85	2.25	300	282	160	232	430
N2	P	85	2.20	324	308	160	269	430
N2	N	34.3	1.20	292	274	160	222	594
N2	P	34.3	1.28	325	309	160	264	594
H2	N	85	1.82	207	181	160	84	155
H2	P	85	1.78	231	208	160	132	155
H2	N	34.3	.91	200	173	160	66	253
H2	P	34.3	.90	240	218	160	148	253
15% SF6	N	82.4	3.02	259	239	160	178	204
15% SF6	P	82.4	3.07	272	253	160	196	204
15% SF6	N	21	1.36	255	235	160	172	297
15% SF6	P	21	1.3	274	255	160	199	297
30% SF6	N	41	2.35	247	226	160	160	231
30% SF6	P	41	2.02	290	272	160	220	285
30% SF6	N	21	1.52	267	248	160	189	298
30% SF6	P	21	1.38	285	267	160	214	339
(1) assumes measurement system risetime, ~100 psec; (2) assumes inductance, ~15 nH/cm; (3) $\tau(\text{measured})^2 - \tau(\text{inductive})^2 = \tau(\text{resistive})^2$								

It is interesting to note that in all of the test cases the faster risetimes are obtained when the monocone tip is negative rather than positive. For the 30% gas mix, the differences in fields are enough to explain this according to the formula; but for the other cases the fields are almost independent of polarity. This suggests that a negatively initiated streamer has a shorter resistive phase risetime.

For nitrogen with the negatively-charged tip, the inferred resistive phase is approximately 85% of that with the positively-charged tip for both the high and low pressures. For hydrogen, the negatively-charged tip resistive phase is 63% of that of the positive tip at 85 atmospheres and 45% of the positive tip at 34.3 atmospheres. For the 15% SF6 mix, the negatively-charged tip resistive phase is approximately 90% of that for the positively-charged tip at 82.4 atmospheres and 86% at 21 atmospheres. For the 30% SF6 mix, the negatively-charged tip resistive phase is 73% of that of the positive tip at 41 atmospheres and 88% at 21 atmospheres.

When comparing the risetimes with similar pressures and polarities, the hydrogen risetime is always observed to be faster as would be expected from Martin's formula (which was obtained at lower pressures). At 85 atmospheres with negative tip polarity, the hydrogen resistive phase imputed from the measurements is 36% of that of nitrogen and with a positive tip this becomes 49%. At 34.3 atmospheres with a negative tip, the hydrogen resistive phase is 29% that of nitrogen and with a positive tip this becomes 56%.

In going from nitrogen to hydrogen with no pressure change, the formula would compute a hydrogen resistive phase approximately 41% of nitrogen as a result of the density change and the hydrogen breakdown field being about 75% that of nitrogen. The resulting data seems to roughly confirm this ratio.

For a given gas, one would have predicted from the resistive phase formula that the risetime would have increased by about 40% in going from 85 to 34.3 atmospheres. This assumption is based on the changes in the measured breakdown fields and the gas density at the two pressures. No such change was observed. The accuracy of the resistive phase formula seems better for estimating the risetimes at higher pressures. It appears that the resistive phase does not increase with increasing gas pressure as postulated earlier based on Martin's formula. Even with the field varying as  $p^{0.5}$  to  $p^{0.6}$  rather than  $p^{0.7}$ , such a decrease is still predicted by the formula. Apparently the formula over-states the dependence of the resistive phase on field or understates the dependence on density. Note that for a given voltage the total risetime will still decrease with increasing pressure because of the reduced inductive risetime.

The resistive phase formula is pessimistic in most cases in calculating the resistive phase. Although the calculated risetime for the 15% SF6 mix is in close agreement with the measured value, for the others the calculated risetimes are factors of 1.5 to 2 and more higher than the measurements.

## **3.0 PHASE II PULSER FABRICATION AND TESTING**

### **3.1 Pulser Design**

#### **3.1.1 General**

The design of the demonstration pulser incorporates the features described in Section 1.3. The pulser test bed hardware consists of five major components that includes (1) the control consoles; (2) the Marx generator; (3) the oil box, Marx enclosure and cart; (4) the pulser; and (5) the coaxial feed and antenna.

Figures 65 through 69 show views of these components.

The circuit concept is based on a voltage source (Marx generator) that charges the pulser that contains a two-stage pulsewidth and risetime shortening circuit. This two-stage circuit consists of a transfer stage that is discharged into a peaking stage and ultimately into the load. A simplified circuit schematic of the pulser test bed is shown in Figure 70.

#### **3.1.2 Marx Circuit**

Referring to the nomenclature of Figure 70, the 500 kV Marx generator has an erected capacitance (CM) of 425 pF. The Marx is constructed of a total of twelve 50 kV rated capacitor half-stages oriented horizontally in a linear stack. At the beginning and end of the stack is a single 50 kV half-stage while the rest of the stack is composed of 5-100 kV full stages each made up of two series half-stages. Each half-stage is built from three parallel, 50 kV rated TDK 1.7 nF ceramic capacitors.

Model 40264 gas spark gaps connect each of the stages. A total of six spark gaps are used. The gaps use air as the insulant.

The full open-circuit voltage rating of the Marx operating at  $\pm 50$  kV dc charge is 600 kV. For reliability, the Marx is designed to operate at approximately 500 kV output using a dc-charge level of  $\pm 45$  kV or less. This gives more than a 10% safety margin to the capacitors, switches, and the Marx charge and trigger resistors.

The stray series inductance of the Marx (LM) is 1.5  $\mu$ H that can charge the pulser in 25 ns or less. No additional inductance was added in order to slow the charge during the pulser tests. The estimated stray series resistance (RM) is about 1 ohm. An equivalent shunt resistance (RSH) of 1000 ohms represents the various Marx resistors in the circuit during the discharge.

The polarity of the Marx is reversible simply by interchanging the input leads where they enter the Marx box.

(a) Gas control console



(b) Charging and triggering console



(c) Ancillary system console

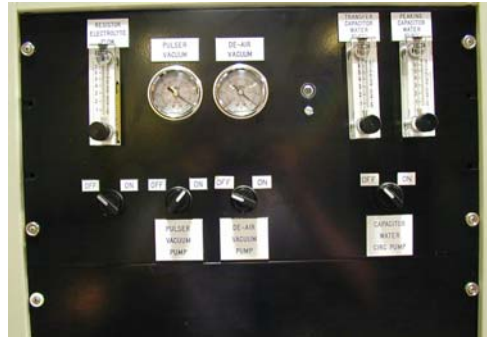


Figure 65. Control consoles.



Figure 66. Marx generator.



Figure 67. Marx enclosure, oil box and cart.

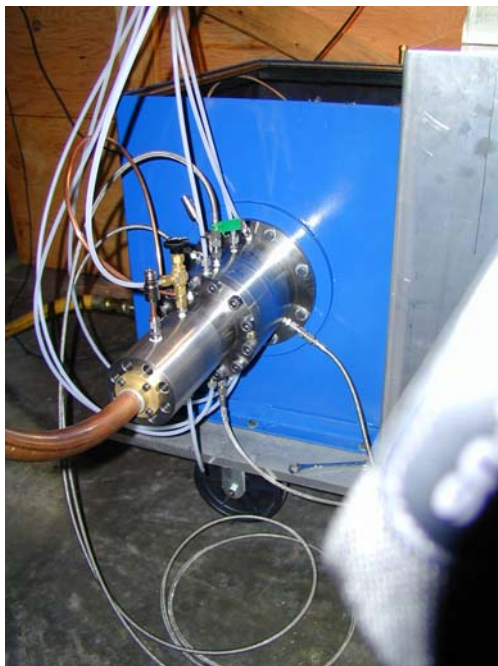


Figure 68. Pulser.

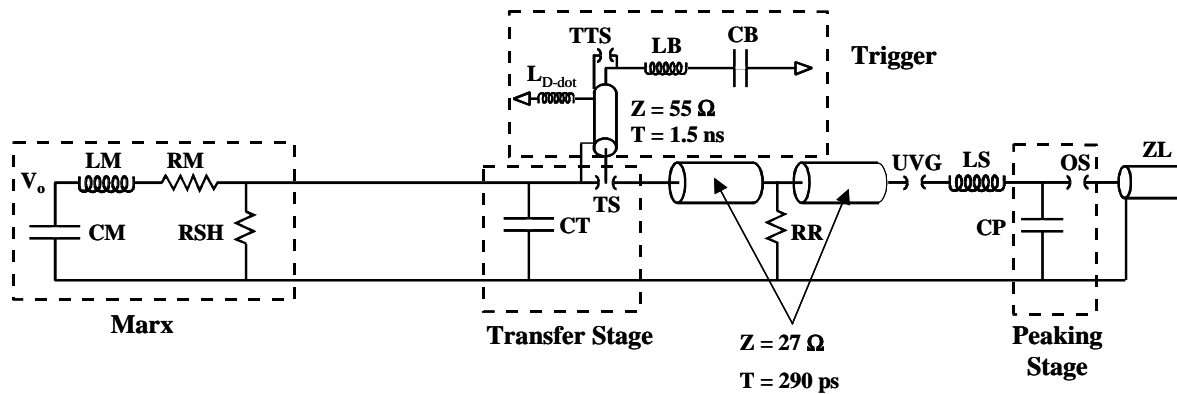


(a) Antenna



(b) Coaxial feed to antenna

Figure 69. Coaxial feed and antenna.



CM (Marx Capac) = 425 pF  
 LM (Marx Induct) = 1.5  $\mu$ H  
 RM (Marx Series R) = 1  $\Omega$   
 RSH (Marx Shunt R) = 1000  $\Omega$

$L_{D\text{-}dot}$  = 4.5  $\mu$ H  
 LB = 1  $\mu$ H  
 CB = 10-20 pF  
 CT = 98 pF  
 RR = 100  $\Omega$   
 LS = 40 nH

CP = 20 pF  
 ZL = 60  $\Omega$

TTS = Trigger Switch  
 TS = Transfer Switch  
 UVG = UV Illuminator Gap  
 OS = Output Peaking Switch

Figure 70. Simplified pulser circuit.

The Marx is triggered by a simple trigger circuit that is composed of a coaxial cable dc charged to 45 kV. The cable is shorted at its far end by a gas switch that launches a pulse of equal but opposite polarity to that of the dc charge voltage.

The cable is resistively coupled to the first two Marx switches through a blocking capacitor composed of two series TDK 1.7 nF, 50 kV ceramic capacitors and connected to the trigger electrodes of each of these two switches through approximately 500-ohm resistors. The other end of the cable is switched by means of a Model 40264 spark gap that uses air as its insulant.

This Model 40264 switch has its midplane resistively biased to half the charge voltage or approximately 22.5 kV when the full gap voltage is 45 kV. A PT-55, which is a 70 kV trigger amplifier, triggers this switch. The output of the PT-55 couples to the Model 40264 switch midplane through a series combination of a 100-ohm resistor and a 1.7 nF 50 kV TDK ceramic capacitor.

The Marx triggering scheme employed here results in a Marx output jitter of about 5 ns.

The entire Marx is housed within a sealed aluminum box that is filled with SF6 at ambient pressure to insulate the components from dc breakdown as well as pulsed breakdown. The Marx enclosure couples directly to an oil box in which the pulser is mounted. The oil insulates the input portion of the pulser which has exposed surfaces that are pulsed up to full voltage. The two containers are placed on a cart for mobility.



### 3.1.3 Pulser Circuit

The two stages of the pulser circuit form the primary and peaking stages of a traditional peaking circuit. The primary stage is referred to as the transfer stage and the other the peaking stage. These two stages are gas-switched with the primary switch being triggered and the peaking or output switch self-breaking (see Figure 70).

The value of the transfer capacitance (CT) determines the output decay time into the load. For the designed load impedance (ZL) of approximately 60 ohms and the desire to have at least a 5 ns e-fold decay time, the value of the transfer capacitance calculates to about 85 pF. For a little extra margin to allow for the actual waveform ripples and reflections etc. an additional 10% margin was added making the capacitance about 98 pF.

As discussed in earlier sections, an important aspect of the design is that the pulse charge times be rapid. The self-imposed specification placed on the charge time of the primary stage was for it to be less than 25 ns. This stage is charged by the Marx with a  $1 - \cos \omega t$  waveform and has been measured to be in the range of 10-25 ns to the time of switchout through the transfer switch (TS) depending on the firing angle. Thus, the charge time requirement is met.

After allowing for the mechanical strength requirements and reasonable electrical fields within the pulser, the resulting inductance feeding the peaking stage is approximately 50 nH composed of the equivalent inductance of the feed line amounting to about 20 nH and an additional lumped inductance (LS) of about 30 nH. Using Equation 5 for determining the peaking capacitance (CP), the correct value should be about 15 pF. The calculated value of the actual fabricated peaking capacitor was approximately 20 pF.

This stage is charged in about 1.5 to 2 ns as required. The output switch (OS) is UV- illuminated by a highly enhanced, small spacing gap referred to as UVG that is in the peaking capacitor charging path. The current passing through this switch during the charging of the peaking capacitor produces ultra-violet light that floods the entire output gap region which is in the line of sight. Electrons are produced and reports in the literature describe uniform bulk breakdown in the gap region under these conditions when the gap is charged within the formative time of the switch of about 1 to 2 ns.

A resistor referred to in the circuit as RR was required to reference the conductor downstream of the transfer switch to ground. Simulations showed this conductor to significantly jump up in voltage due to its coupling capacitance to the charged electrode during the charging of the transfer stage. With the resistor in place with a value of 100 ohms, the conductor remains at ground potential during the pulse charge.

As has been discussed, the transfer switch is the triggered switch. The triggering circuit scheme for the switch is also shown in Figure 70. The trigger source for the transfer switch is a charged coaxial line of 55 ohms and a one-way transit time of 1.5 ns. The coax feeds the mushroom trigger electrode of the transfer switch directly and thus must be voltage balanced correctly so that the mushroom floats on an equi-potential surface during the pulse charge.

To properly balance the coax voltage, the inner conductor potential must be pulled towards ground. Without any coupling to ground, the inner conductor potential is strongly capacitively-coupled to the outer conductor of the coax. Thus, the inner conductor and mushroom would be at the same potential as the transfer switch electrode.

Capacitive coupling to ground by itself would balance the coax voltage. However, in view of the launched trigger pulse sweeping past the balancing capacitor with an expected risetime of 200 ps, an inductor was added that provided a high impedance to the fast pulse while balancing the voltage during the slower 20 ns charge time. Simulations found the optimal values of LB and CB to be about 1  $\mu$ H and 10 pF for a V/4-V/5 gap configuration. Figure 71 shows these simulations of the transfer switch voltage (VTS) and mushroom voltage (VM) waveforms during the pulse charge.

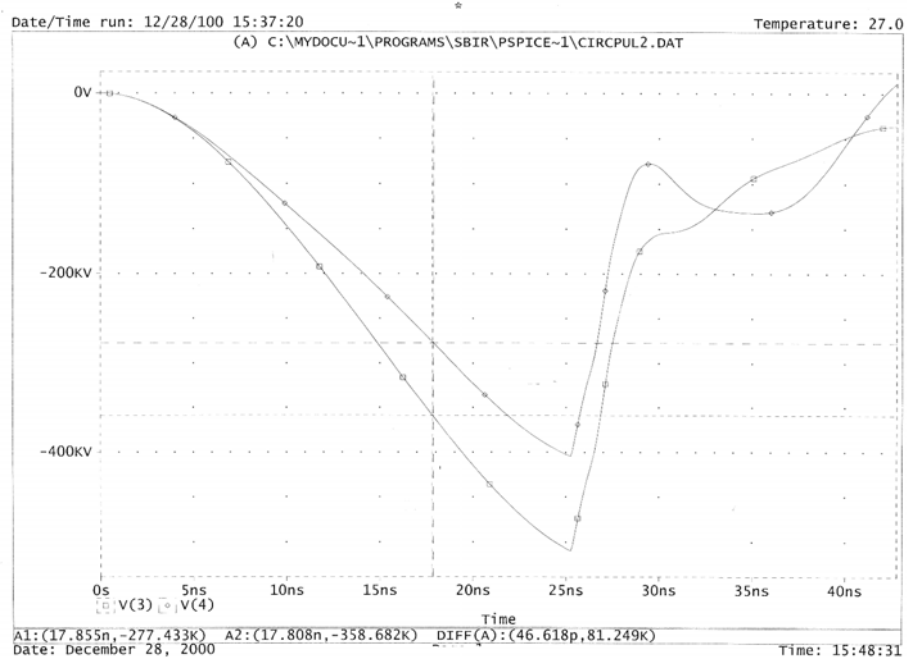


Figure 71. Simulated charging waveforms.

### 3.1.4 Mechanical Layout

Physically, the pulser is shown in schematic form in Figure 72. The actual dimensions can be scaled from Drawing E21700 titled “High Voltage, High Power SBIR Pulser” which is a deliverable with this program. Roughly, the maximum exterior dimensions of the pulser body without the trigger coax or antenna feed is 18 inches long by 6.5-inch diameter. The trigger coax added another 18 inches of length and is approximately 1.25 inches in outside diameter. The antenna coaxial feed is approximately 1.13 inches in outside diameter and starts out from the pulser body horizontally for about 6 inches before it makes a 90-degree turn upwards with a 12-inch radius where it feeds through the antenna ground plane. Its overall length is about 6 feet.



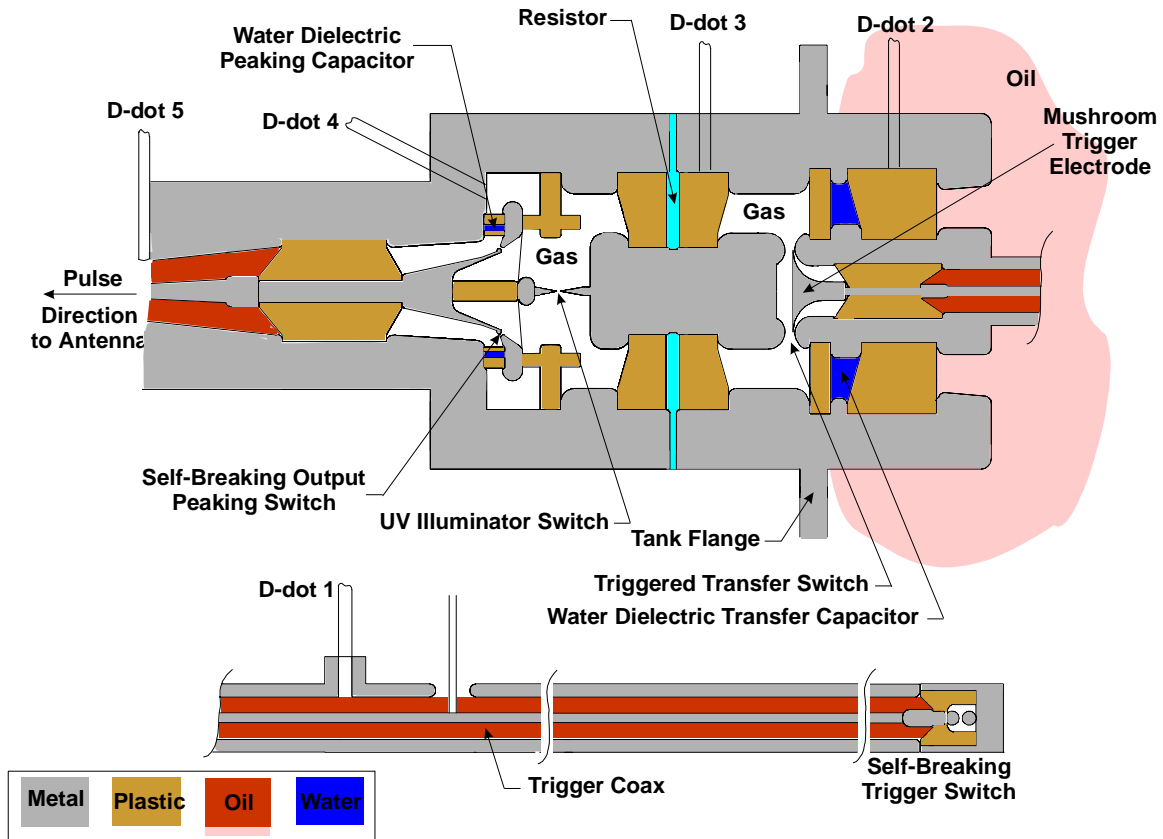


Figure 72. Low jitter triggered pulser.

There are eight main dielectric regions of the pulser. These include:

- the trigger switch gas volume
- the transfer switch gas region
- the output switch gas volume
- the transfer capacitor water volume
- the peaking capacitor water volume
- the trigger coax and surrounding oil volume
- the antenna feed oil volume
- the various plastic interfaces.

A challenging feature of the pulser design was to accommodate the high operating pressures up to 100 atmospheres while maintaining safe electric fields to avoid breakdown and maintain a smoothly transitioning and near constant impedance wave launching region. Compromises undoubtedly had to be made.

The resulting fields as computed with Quickfield are displayed in Figure 73 as well as the stress times. As will be described in a later section, breakdowns did occur with the initial design in the output switch region. Several attempts to reduce the local fields in the output region resulted in increasing the reliable operating output voltage to about 300 kV where the voltage was

ultimately limited to. The fields described in Figure 73 reflect those resulting after all of the modifications that were made and as the hardware exists in its deliverable form.

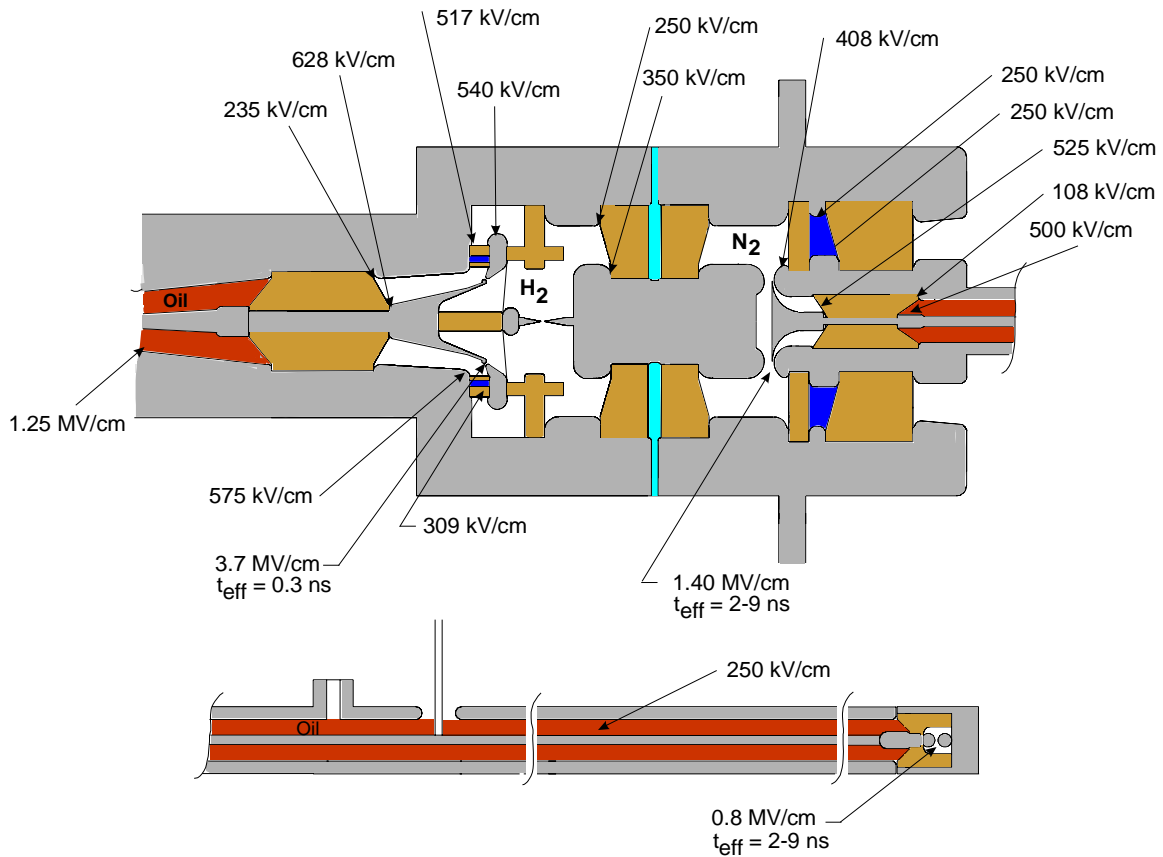


Figure 73. Typical fields at 300 kV.

The trigger switch referred to as the TTS for Transfer Trigger Switch shorts the trigger coax and launches the pulse that triggers the transfer switch. The risetime should be as fast as possible in the range of 200 ps so hydrogen was chosen as its switching medium. This switch sees approximately 20% of the transfer switch voltage or about 60 kV with 300 kV on the transfer stage.

The TTS electrodes were each 0.25-inch diameter balls with a gap of 0.0953 cm. Since this gap is self-breaking, 0.030-inch diameter holes were drilled in each ball in the gap region to add some local surface enhancement to stabilize its breakdown. The enhancement of the gap was about 1.2 without accounting for these holes. The peak field within the gap at 60 kV with a stress time in the range of 2 to 9 ns was estimated to be 0.8 MV/cm without accounting for the local enhancement from the small drilled holes. With the hydrogen gas this meant typically operating the gap at about 40-45 atmospheres.

The TTS body was fabricated from Torlon. A photograph of the disassembled switch is shown in Figure 74.



Figure 74. Self-breaking trigger switch.

The trigger coax is 18 inches long and has an impedance of about 55 ohms. The coax inner conductor diameter is approximately 0.18 inches and the outer 0.75 inches. The calculated peak field on the inner conductor for a full 100 kV (for full 500 kV operation) is 250 kV/cm. Using Equation 8 to determine the breakdown field for the oil, the inner conductor will be quite safe at far less than 20% of breakdown. Even the regions around the Torlon interface at 500 kV/cm are still conservative.

The trigger coax will apply a pulse to the transfer switch with a pulse width of twice its transit time resulting in a 4.6-ns trigger pulse length.

A photograph of the exterior of the trigger coax is shown in Figure 75. The entire coaxial assembly is immersed in oil that is contained in the oil box. This is necessary because the outer conductor of the coax is at the full potential of the transfer switch. The figure shows the Marx charging connection attached directly to the coax. At the same time the inner conductor must be at about 4/5 of this voltage resulting in the voltage differential between the mushroom and charged transfer switch electrode.

To maintain such a voltage differential between the coax inner and outer conductors, the inner must be coupled to ground with the appropriate circuit elements. As described in the circuit diagram in Figure 70, an inductor LB of about 1  $\mu\text{H}$  and capacitor CB of about 10 pF are introduced for this purpose. Figure 75 shows the physical placement of these elements. The inductor is a length of coiled  $\frac{1}{4}$ -inch diameter refrigerant tubing and the capacitor is an 8-inch diameter plate with a plastic spacer nominally 1 inch thick to ground.

Also shown in Figure 75 is the coax D-dot cable that must be coiled into an inductor as to isolate the D-dot from ground. The isolation inductance is about 2.5  $\mu\text{H}$  but with ferrite rings added this increases to at least 4.5  $\mu\text{H}$  which was the value used in the simulations.

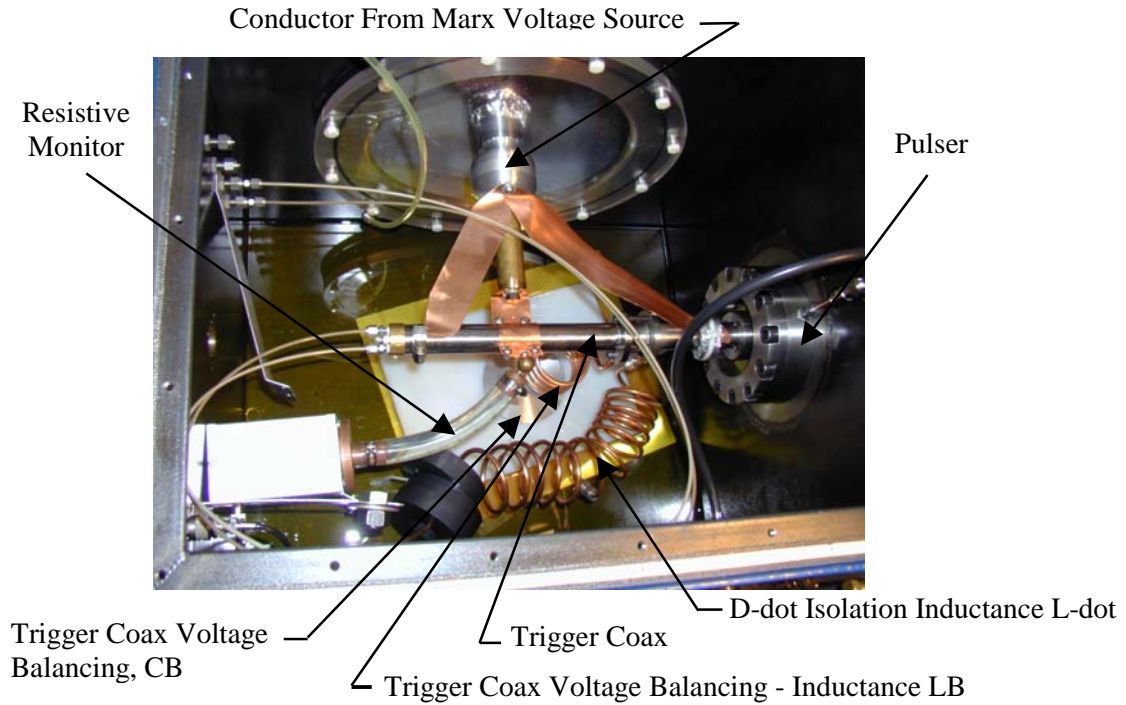


Figure 75. Interior of oil tank.

The resistive monitor is also shown in Figure 75 and monitors the pulse charge voltage on the transfer capacitor.

A view of the charged electrode side of the transfer switch that will be referred as the TS is shown in Figure 76. The Torlon interface that separates the transfer capacitor water from the gas volume is seen surrounding the central electrode. The outer diameter of the Torlon is about 3.5 inches and the diameter of the electrode is about 2 inches. The mushroom is about 1.5 inches in diameter and is set about 0.0345 inches (0.0876 cm) off the main electrode. With the most recent and successful total gap setting of 0.089 inches (0.226 cm), this makes the gap a  $V/2.58$  configuration. Balanced, the mushroom gap would be at 0.39 the total gap and the coax and mushroom would be balanced at  $0.61V_0$  where  $V_0$  is the total TS voltage. Previous TS gap settings have been as large as 0.144 inches (0.366 cm).

Figure 77 shows the TS charged electrode with the mushroom removed.

The annular water volume of the transfer capacitor behind the Torlon insulator interface is designed so that the inner and outer conductor areas are nearly equal. This is seen in Figure 73. This produces a field distribution nearer uniform than what would be the case for a coaxial geometry resulting if the lengths of the inner and outer conductors were equal.

The peak fields on the conductors in the water at 500 kV as determined by Quickfield are about 420 kV/cm. Equation 6 computes the breakdown field to be about 900 kV/cm. Thus, the water transfer capacitor operates at ~ 50% of breakdown making it quite safe.

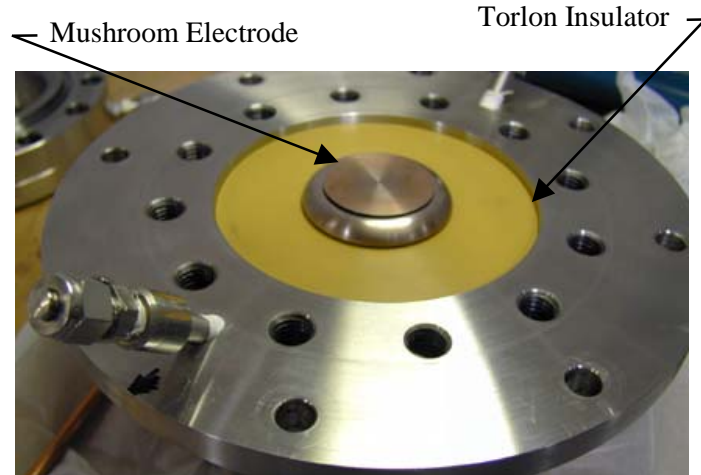


Figure 76. Transfer switch mushroom electrode.

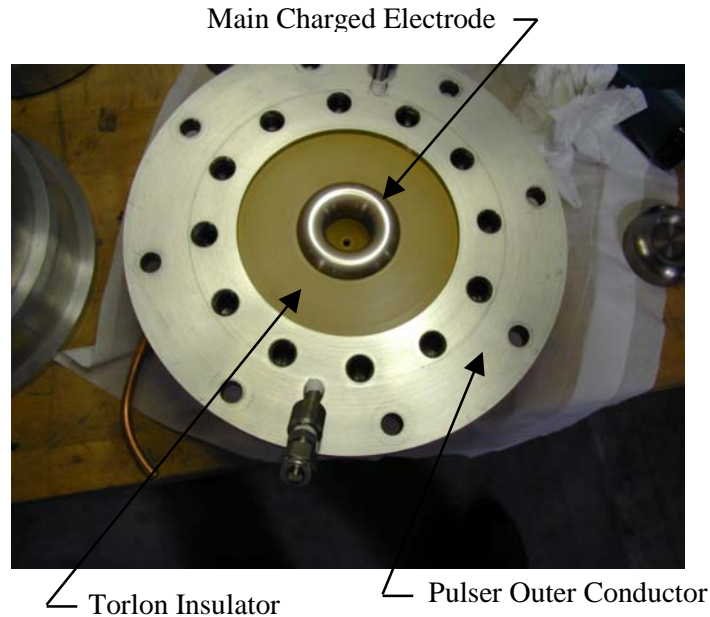


Figure 77. Transfer switch charged electrode with mushroom removed.

The highest design fields surrounding the TS gap region in the gas do not exceed 408 kV/cm at 300 kV operation that is only about 20-25% of the nitrogen gas hold-off field.

The downstream TS electrode is shown in Figure 78. The diameter of the electrode is about 2-inches and the central-most section of it has been removed to minimize the stray capacitance between it and the mushroom. This reduces feed-through pre-pulse during the fast trigger and minimizes the capacitive loading of the mushroom during triggering.



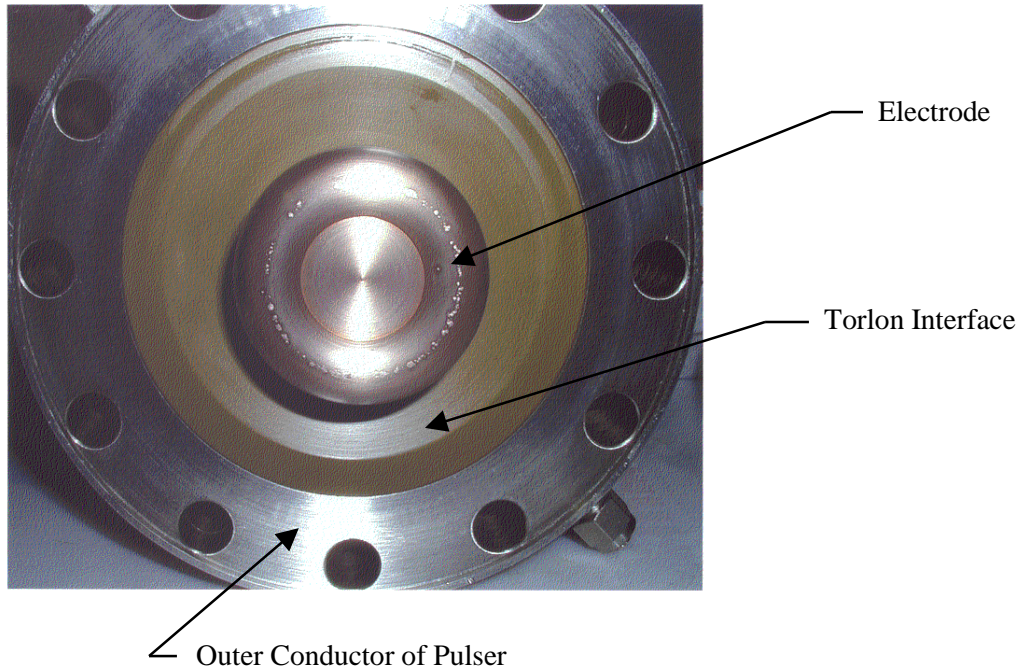


Figure 78. Transfer switch downstream electrode.

The gap field at 300 kV with the 0.226 cm spacing is about 1.40 MV/cm. For the 2 to 9 ns stress time and the intended operation at about 80% of self-break voltage, approximately 68 atmospheres of nitrogen would be required.

A Quickfield plot of the TS gap field distribution during the pulse charge and before the trigger pulse arrives is shown in Figure 79.

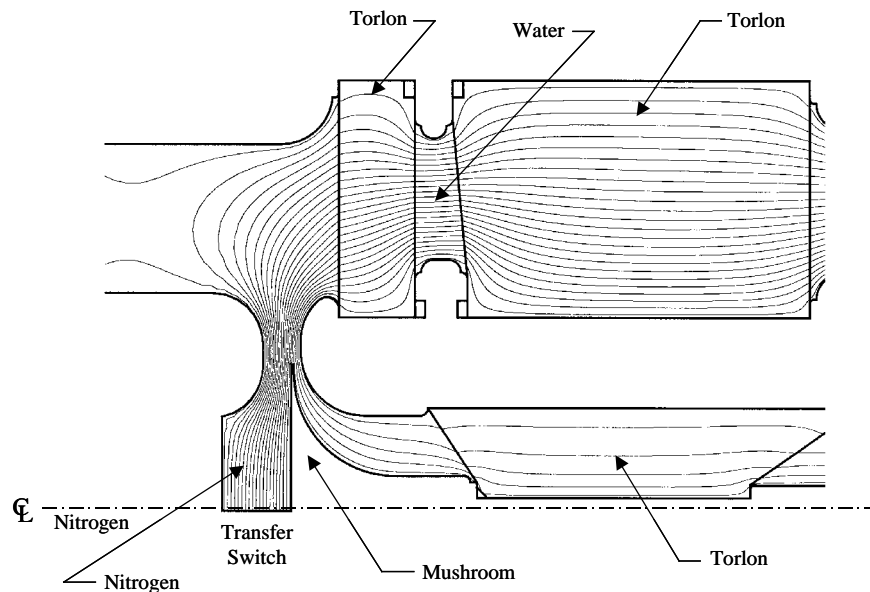


Figure 79. Transfer switch electric fields before triggering with balanced mushroom voltage.

Downstream of the TS is a coaxial feed section. Surrounding the feed is a Torlon block that holds the coaxial feed inner conductor in place (see Figure 72). This entire feed that links the TS with the UV-illuminator gap and ultimately to the peaking capacitor has an estimated total inductance of 50 nH.

The 50 nH feed is composed of a short 50-ohm gas section between the TS and the Torlon block interface with a transit time of about 125 ps equivalent to 7 nH. The 27-ohm Torlon insulated section having a transit time of 290 ps follows this and is equivalent to about 8 nH. This is followed by a 50-ohm, 60 ps long gas section of 3 nH and a 200-ohm, 110 ps long section equivalent to 22 nH that includes the UV gap. Four spokes feed the current to the peaking capacitor charged plate and charge the peaking capacitor. This contributes an additional 10 nH and is approximately 50 ps long.

In all, the transit time between the TS and the output switch that will be referred to as the OS is approximately 635 ps.

The feed section is resistively coupled to ground by two parallel resistors that together amount to 100 ohms. These are two 0.25-inch-diameter holes drilled radially through the Torlon block and filled with a flowing solution of 18 ohm-cm sodium thiosulphate. Without this resistance, the prepulse on the feed's center conductor during the transfer stage charging was shown in the simulations to be quite high. This was thought not to be desirable because of the uncertain pre-breakdown effects it could have on the downstream UV and OS gaps. With the resistor, the prepulse is negligible.

Figure 80 shows the downstream UV gap electrode and the Torlon structure that holds the peaking capacitor and the OS electrodes in place. The UV gap is set to have a very small gap of about 0.018 inches and is designed to break immediately by greatly enhancing the fields by pointing its electrodes. The gap is aligned so that it is in direct line of sight of the OS electrodes and the gas region between the OS electrodes as to illuminate these regions as soon as current begins to flow to charge the peaking capacitor.

The four spokes feeding the peaking capacitor are intended to minimize inductance while allowing the maximum transparency for the UV illumination of the OS. These spokes are more easily viewed in Figure 81 where the Torlon structure and the pulser outer conductor have been removed. In the figure, the charged peaking capacitor plate and charged OS electrode are shown as well as the downstream OS electrode.

The peaking capacitor body is shown in Figure 82 with the charged plate comprising the peaking capacitor plate and OS electrode removed. The present dimensions of the annular peaking capacitor are approximately 2-inches inner diameter and 2.75-inches outer and the length is 0.385 inches. Thirty-six holes each 0.100-inch-diameter form the water dielectric volume and are filled with flowing de-ionized water. The value of this capacitor is approximately 20 pF as determined necessary from Equation 5.



Figure 80. UV illuminator downstream electrode with Torlon support for peaking capacitor.

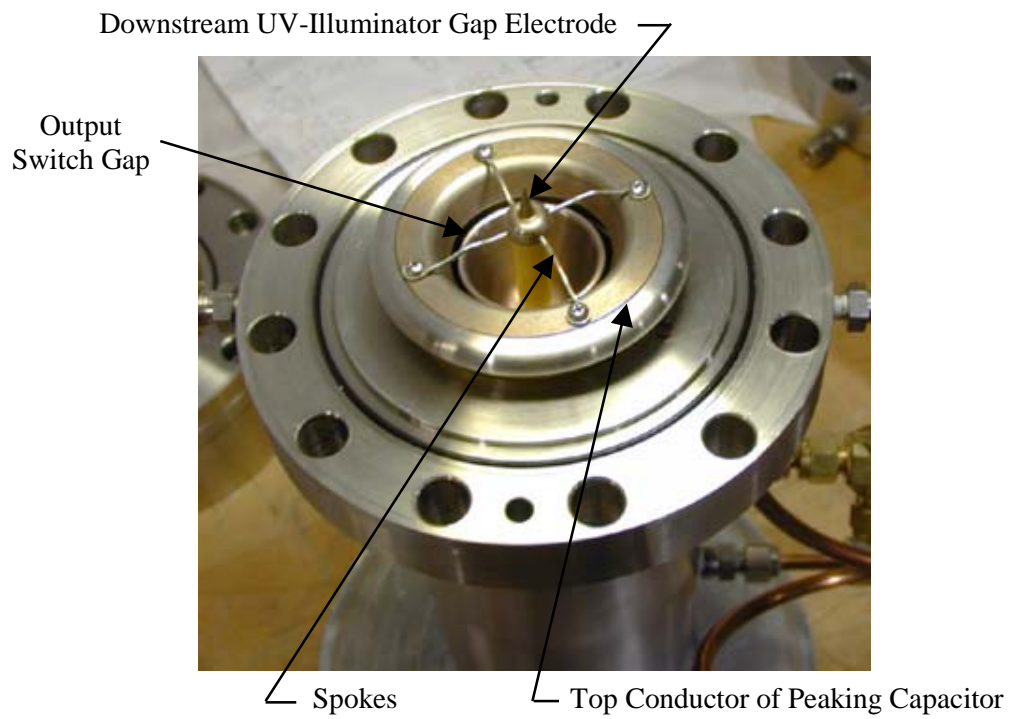


Figure 81. Peaking capacitor and output switch charged electrode assembly.



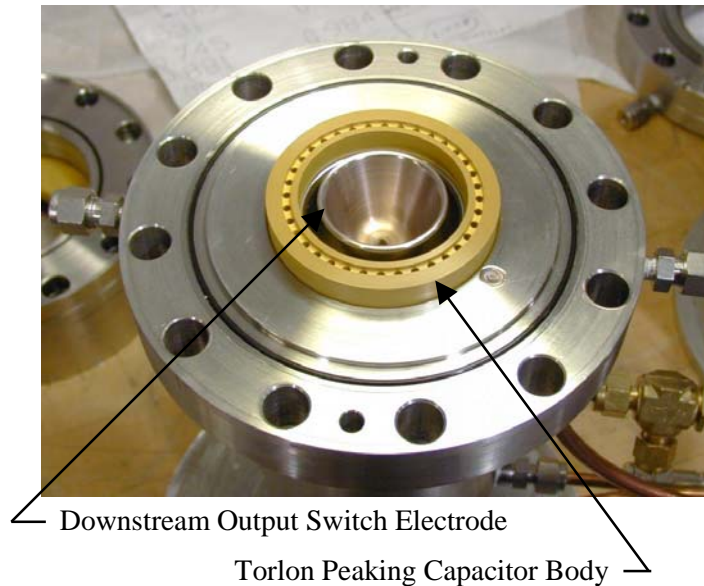


Figure 82. Peaking capacitor and downstream output switch electrode with charged electrode removed.

Using Quickfield, the design fields in the water of the peaking capacitor are about 300 kV/cm at 300 kV. The stress time for the capacitor is about 1.5 ns. Using Equation 8, the water breakdown fields compute as about 1.7 MV/cm. Thus, operation is at only about 33% of the water breakdown, which is very conservative.

The downstream OS electrode is shown with the peaking capacitor body removed in Figure 83. The electrode is an integral part of the tapered feed into the oil coaxial line. The OS electrodes are K-33 alloy and the most recent and successful gap spacing for 300 kV operation is 0.0415 inches (0.105 cm). The radius of curvature of each of the electrodes is 0.0375 inches (0.0953 cm). This gives an enhancement factor of about 1.3 resulting in switching fields of 3.7 MV/cm. The OS uses hydrogen and for a stress time of about 0.3 ns the breakdown field data for the positive monocone extrapolates to about 3.7 MV/cm at a pressure of about 100 atmospheres, which is where the OS switch operates.

In other regions in the OS hydrogen gas volume, Figure 73 indicates the fields to be as high as 575 kV/cm nearby the base of the peaking capacitor plastic interface and 628 kV/cm near the gas side ID of the Torlon gas/oil interface. At the OS operating pressures this would have been considered safe but breakdown problems were experienced at the edge adjacent to the capacitor plastic interface which will be described in Section 3.1.7.

The oil coaxial line that connects the antenna to the pulser output is a 60 ohm line with an inner conductor diameter of 0.25-inches and an outer of 1.125-inches. The fields on the inner conductor at 300 kV operation are about 1.25 MV/cm. Equation 6 computes the breakdown fields at about 3.8 MV/cm for a 1 nanosecond stress time. Thus, the line operates at only about 33% of breakdown making it very conservative.

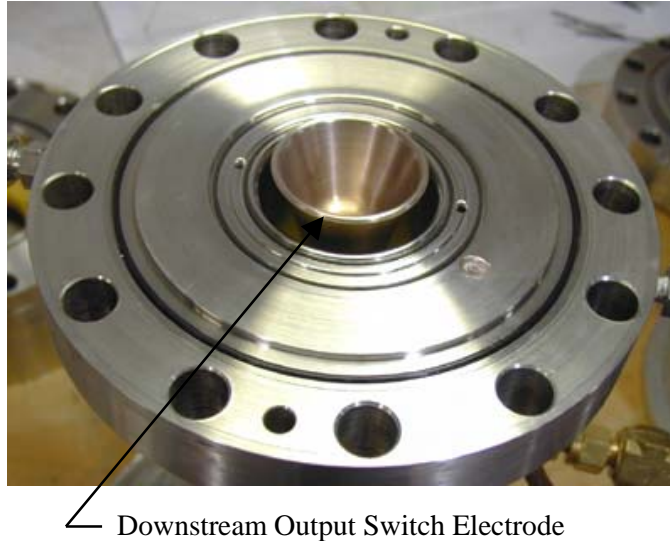


Figure 83. Downstream output switch electrode and coaxial feed section.

### 3.1.5 Diagnostics and Instrumentation

There were six primary diagnostics used in the tests. These were as follows:

- a 2400-ohm calibrated resistive voltage monitor
- a D-dot probe (D-dot 1) located on the trigger coax
- a D-dot probe (D-dot 2) located at the transfer capacitor
- a D-dot probe (D-dot 3) located at the coaxial feed section between the TS and the OS
- a D-dot probe (D-dot 4) located at the peaking capacitor
- a D-dot probe (D-dot 5) located at the oil line.

The resistive monitor was used to measure the relatively slow pulse charge time of the transfer capacitor which occurs typically is about 20 ns. The monitor was approximately 9 inches long and its tap-off is connected to a secondary divider contained in a metal box. Figure 75 shows the monitor location where it is connected to the trigger coax outer conductor. Being in the oil box, the signal from this monitor tended to be somewhat noisy with ripples and oscillations on the waveform. This introduced a level of uncertainty as to what the peak voltage was at the time of TS closure.

The D-dot locations are indicated in Figure 72.

The construction of the D-dot on the trigger coax as with all the D-dots used, is a cut-off 0.25-inch diameter semi-rigid cable. Its risetime is on the order of the transit time of a wave sweeping across its end diameter that is about 25 ps.

Because the outer conductor of the trigger coax is at the full charge voltage of the transfer stage, the D-dot must be isolated from ground. This is accomplished by coiling up a 12-foot long length of the semi-rigid to form a 12-inch long, 3-inch diameter, 12-turn inductor. With ferrite rings, the total inductance was about 4.5  $\mu\text{H}$  which the simulations confirmed was adequate.

This D-dot was used to detect the trigger pulse arrival time and the trigger pulse amplitude and risetime. Its use as a time mark formed the basis for measuring TS jitter where the arrival of the TTS pulse was defined as  $t_0$ .

This D-dot was calibrated by dc charging the inner coax to a known voltage with the outer grounded and letting the TTS self-break. The launched pulse amplitude is of equal but opposite polarity as the dc charge voltage allowing a calibration factor to be determined for the integrated waveform. For the calibration, a dc voltage of 15.5 kV was used. A calibration waveform (integrated) is shown in Figure 84 that resulted in a calibration factor for the integrated D-dot 1 waveform of  $1.73 \times 10^{12}$  V/V-s. The waveform shows the main pulse and then the reflection from the open-end which doubles the amplitude.

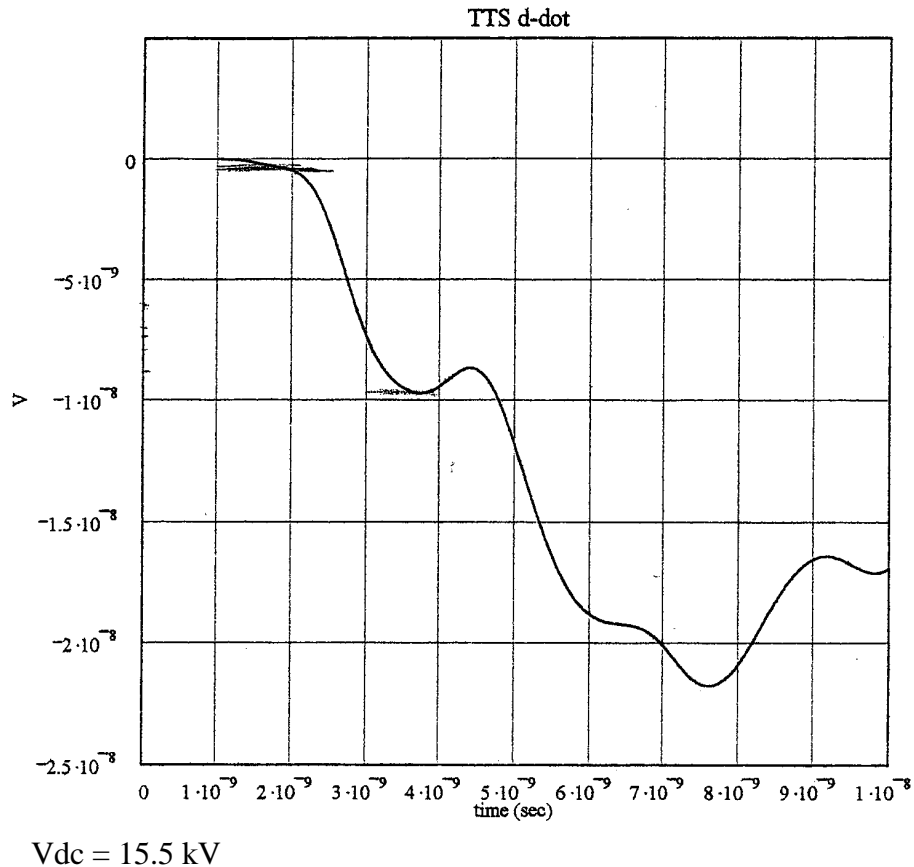


Figure 84. Trigger coax calibration pulse (integrated D-dot).

D-dot 1 provided the method for determining the mushroom balance voltage by enabling a comparison of the launched trigger amplitude (a value equal and opposite to the differential voltage between the mushroom and the TS charged electrode) to the total TS voltage.

The transfer capacitor D-dot 2 was used to view the charging waveform of the transfer capacitor. This signal was integrated and compared to the resistive monitor waveform to derive a calibration factor. The D-dot and resistive monitor waveforms were used interchangeably though

the integrated D-dot 2 was cleaner and smoother. A typical transfer capacitor D-dot waveform (passively integrated) is shown in Figure 85.

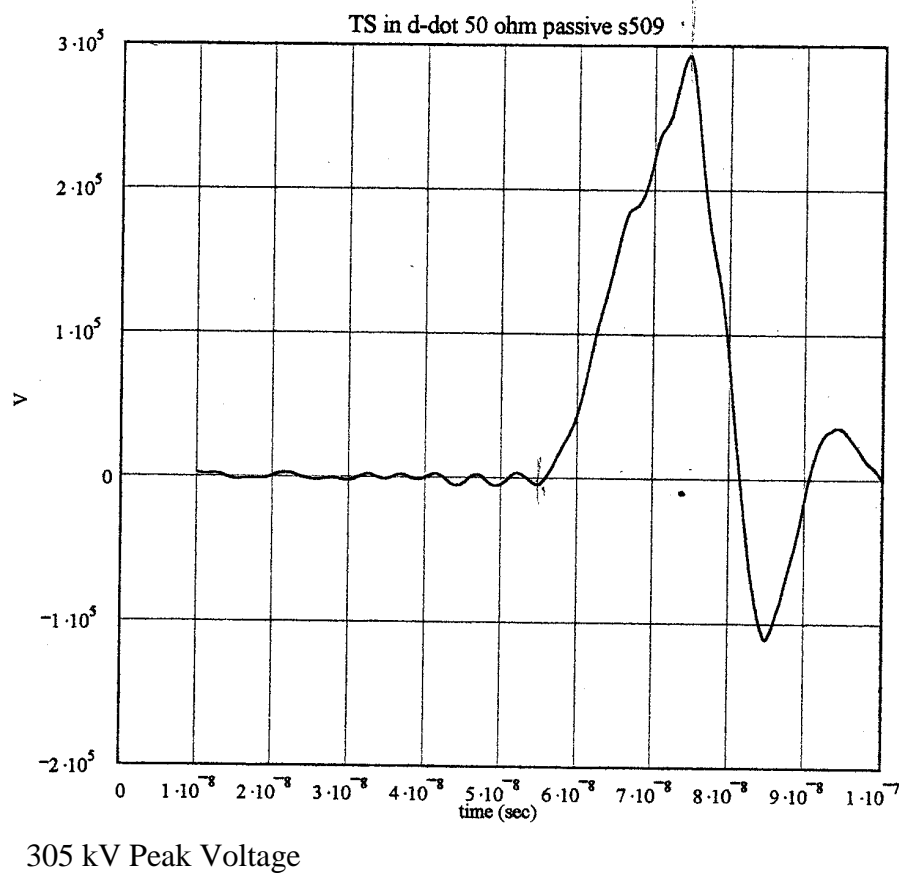


Figure 85. Transfer switch charging voltage waveform (integrated D-dot).

The D-dot 3 located in the coaxial feed between the TS and OS allowed the output waveform from the TS to be viewed. This D-dot was not calibrated. The signal from this D-dot was used as a time mark that when compared to the  $t_0$  time mark from the TTS D-dot enabled the delay and jitter of the TS closure to be determined.

When integrated this signal provided a limited means of viewing the TS risetime. The risetime measurement was limited because of the gross impedance mismatch where the large diameter TS to OS coaxial feed line makes a sudden turn to the UV gap and the UV gap itself. This results in a clear time (two-way transit time) from the D-dot position of only about 300 ps before a reflection from the mismatch and gap is observed. An example of the D-dot 3 software integrated signal is shown in Figure 86.

D-dot 4 at the peaking capacitor location is used to view the peaking capacitor charging waveform when integrated. It is roughly cross-calibrated to the oil line D-dot 5 which itself was calibrated. A sample of the peaking capacitor charging waveform from D-dot 4 is shown in Figure 87.

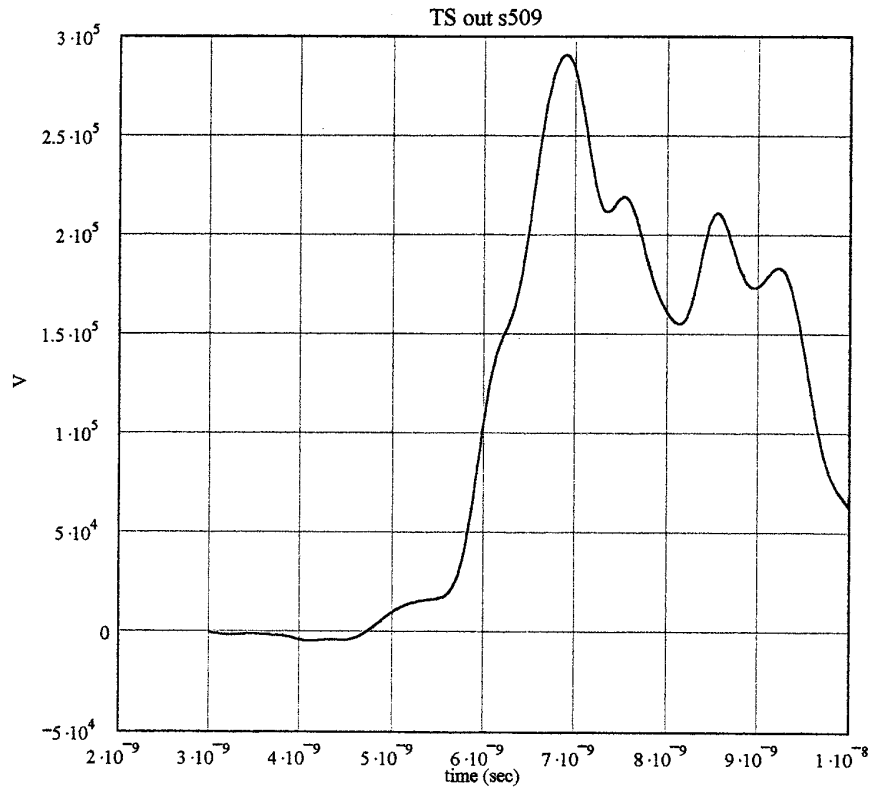


Figure 86. Transfer switch output waveform (integrated D-dot).

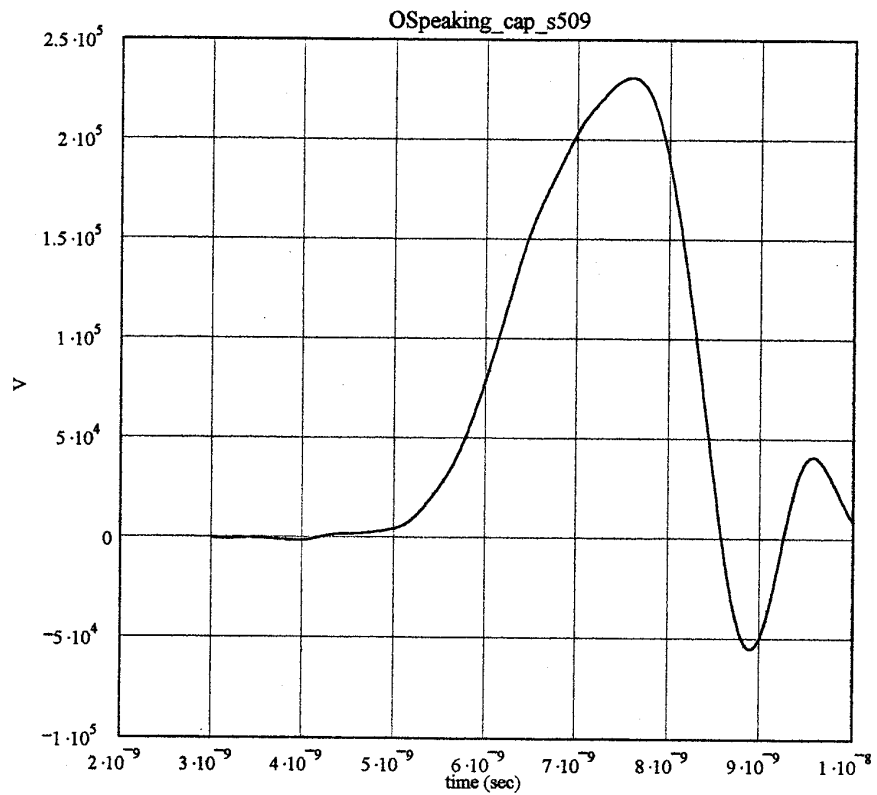


Figure 87. Peaking capacitor charging waveform (integrated D-dot).

The oil line D-dot, D-dot 5, is located approximately 0.8 ns downstream from the OS. This D-dot has been calibrated by dc charging the oil filled line to a known voltage and switching the OS end with a low inductance tack switch. The voltage used for the calibration was 1745 V. The resulting signal is integrated and its amplitude compared to the dc voltage amplitude to obtain the calibration factor of  $7.09 \times 10^{12}$  V/V-s. The calibration waveform is shown in Figure 88 where the reflection from the mismatch at the end of the line tends to try and double the amplitude.

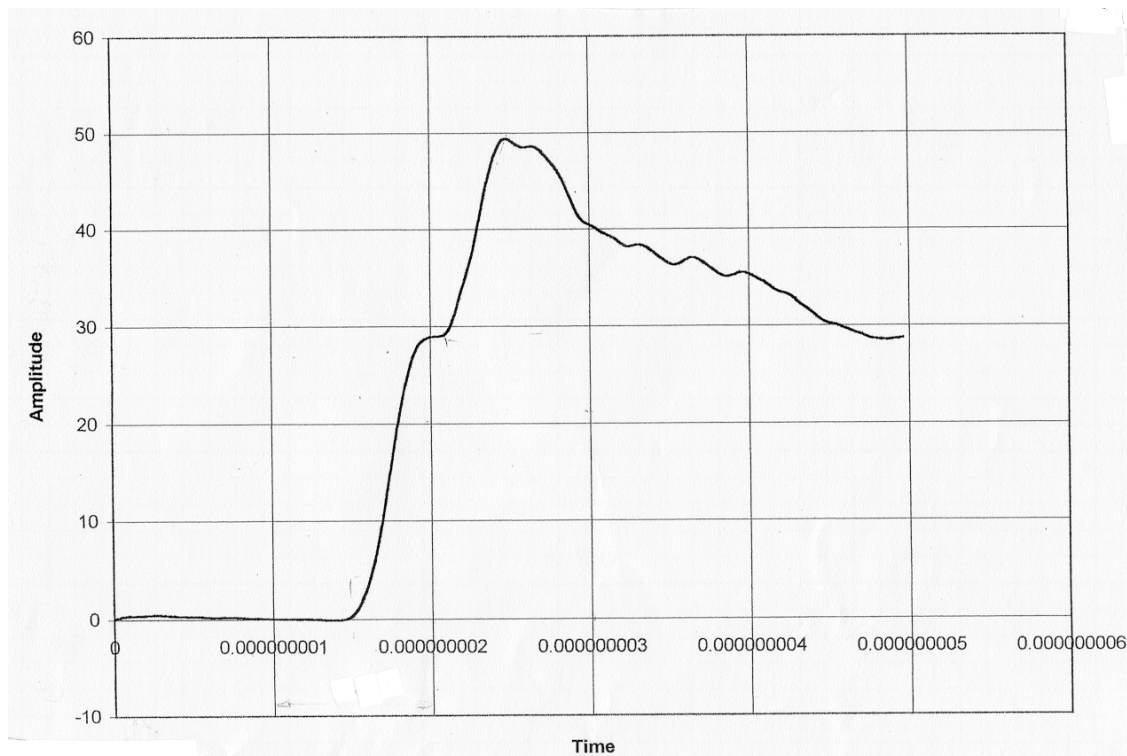


Figure 88. Oil line calibration signal (integrated D-dot).

This D-dot was used as a time mark to measure the overall jitter of the pulsers two switches and when integrated it was used to measure the output risetime.

The instrumentation used for the tests included a TEK540B having a bandwidth of 500 MHz, a TEK684C having a bandwidth of 1 GHz, and two SCD5000 scopes with bandwidths of 4.5 GHz. The SCD's were equipped with 50 ns compensated delay lines (Model DC-11) that virtually maintained these bandwidths. The delay lines were necessary to extract a trigger from the input signal 50 ns prior to the displayed signal arrival.

A cabling diagram for the diagnostics and instrumentation used for the jitter and delay measurements is shown in Figure 89. The cables used were of Andrews 0.5 inch Heliax and splitters were from Barth having an advertised 50 ps risetime. Attenuators were rated at a minimum bandwidth of 10 GHz.

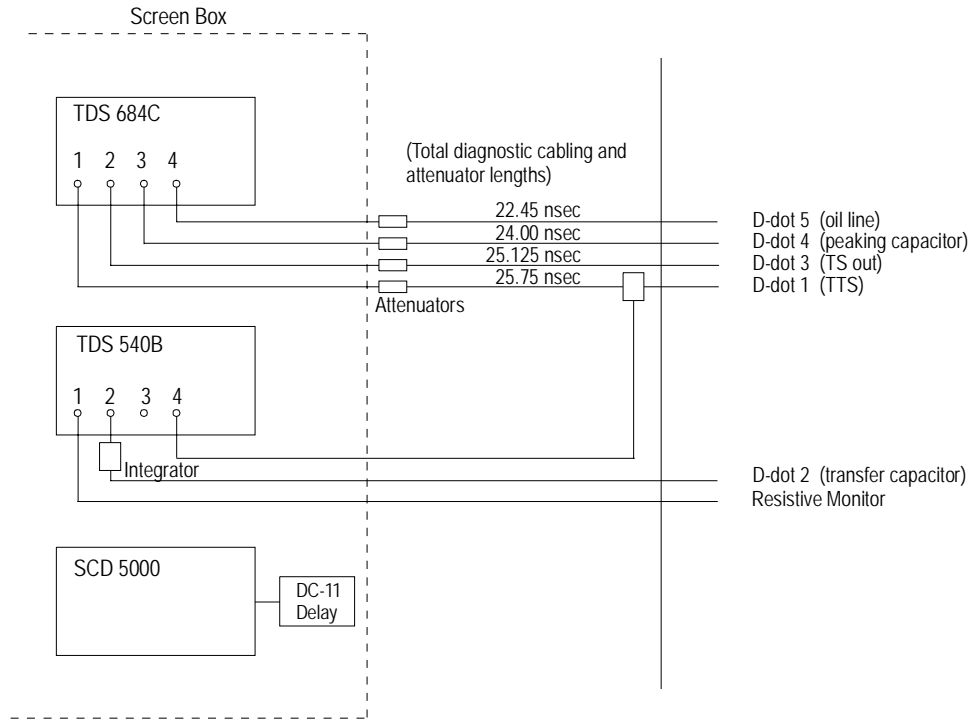


Figure 89. Trigger coax calibration pulse (integrated D-dot).

The cable lengths including attenuators are indicated in Figure 89. Table 7 summarizes these cable lengths in column 2 and lists the physical separation in terms of transit times between the D-dot positions in column 3. If a pulse were driven through the pulser from the TTS to the antenna without regard to switch closure times, i.e. these times being ignored and considered zero, the arrival times at the oscilloscope of each detected D-dot signal is calculated and given in column 4. Column 5 indicates the relative time arrivals referenced to the TTS signal arrival and accounts for the charging and closure times.

Table 7. Normal triggered shot arrival times of the D-dot signals at the oscilloscope.				
D-dot	Diagnostic Path Length (nsec)	D-dot Separation from D-dot 1 (nsec)	Arrival Time at Scope (nsec)	Arrival Time at Scope Relative to D-dot 1 (psec)
TTS D-dot 1	25.75	0	25.75	0
TS out D-dot 2	25.125	1.1	26.225	475 + TS closure time
CP D-dot 3	24.00	1.58	25.58	-170 + TS closure time
Oil Line D-dot 4	22.45	2.39	24.84	-910 + TS closure time + Cp charge time

The interpretation of Table 7 is as follows. After the TTS dot signal arrives, the TS output is detected in a time 475 ps plus the switch closure delay. Thus measuring the time difference between the two and subtracting 475 ps yields the closure delay.

The peaking capacitor  $C_p$  signal will arrive after the TTS signal in a time of the TS closure delay minus 170 ps.

The oil line D-dot signal detecting the OS closure will arrive after the TTS signal a time of TS closure delay plus the  $C_p$  charge time minus 910 ps.

The 684C scope was used to measure the jitter between the recorded signals by overlaying the TTS D-dot, the TS output D-dot, the peaking capacitor D-dot, and the oil line D-dot on the same screen. The measured time differences were recorded and their standard deviation calculated. An example of such a grouping of signals for the same shot is shown in Figure 90.

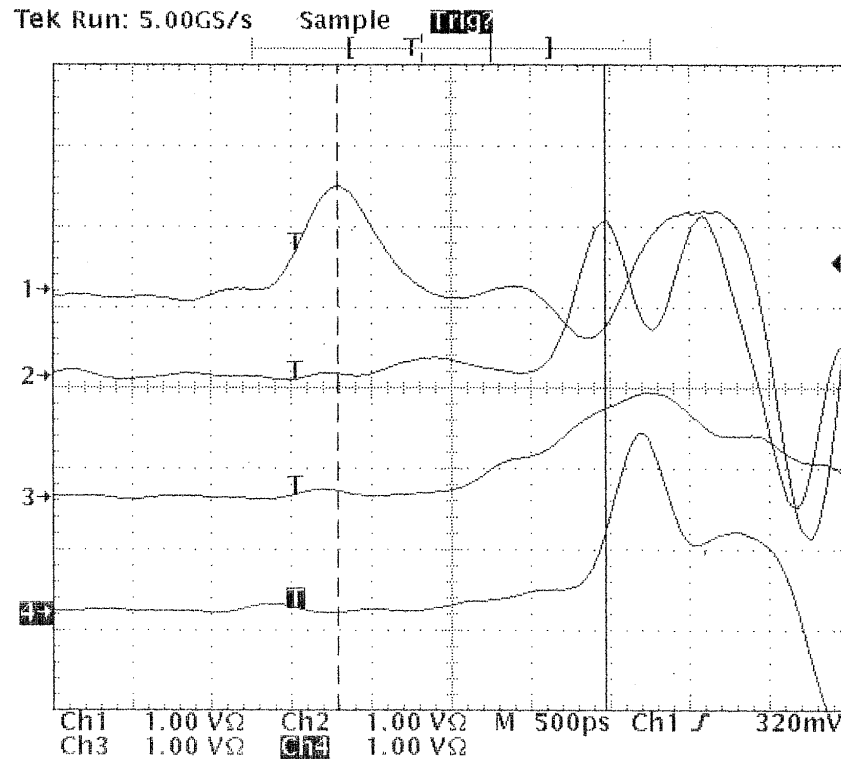


Figure 90. Example of un-integrated pulser D-dot signals used to characterize its operation.

Figure 90 also shows the raw, non-integrated D-dot waveforms. Channel 1 is the TTS signal which will be designated as  $t_0$ . The TS signal appears 1.675 ns after TTS. Referring to Table 7, 475 ps is subtracted from the 1.675 ns to obtain the apparent closure delay or formative time of the gap which calculates to be 1.20 ns.

Further, by referring to Table 7 for the arrival of the  $C_p$  D-dot, it should arrive at  $t_0 - 0.170$  ns + 1.20 ns (closure time of TS) or 1.03 ns after the TTS signal which it does.

Finally, the oil output should arrive 0.29 ns + the  $C_p$  charge time after the TTS signal.  $C_p$  is approximately 1.5-2 ns so the oil output arrival should be at a time of 1.8-2.0 ns after the TTS signal which is approximately where it is.



Table 8 indicates the relative arrival times of the TTS and TS D-dot signals at the oscilloscope in the event of the TS switch prefiring.

Table 8. Prefire arrival times of the D-dot signals at the oscilloscope.				
D-dot	Diagnostic Path Length (nsec)	D-dot Separation from the TS gap (nsec)	Arrival Time at Scope (nsec)	Arrival Time at Scope Relative to D-dot 1 (nsec)
TTS D-dot 1	25.75	0.89	26.64	0
TS out D-dot 2	25.125	0.21	25.335	-1.30 + TS closure time

If a prefire of the TS occurs, the waveform signatures will be quite different. The event begins with the pulse originating at the TS gap. The TS gap is located 210 ps from the TS output D-dot port and 890 ps from the TTS output D-dot port. Thus, ignoring closure delay times, the TTS output D-dot pulse will arrive after 890 ps plus the cable length of 25.75 ns for a total time of 26.64 ns. The TS output waveform will arrive at the scope after 210 ps plus the cable length of 25.125 ns for a total of 25.335 ns.

Since the two sides of the TS gap do not necessarily close at the same time, there would be expected to be a delay on the order of the observed closure delay of 1.2 ns. Thus, the TS would precede the TTS signal by about 0.20 ns. We observe the TTS and TS arrivals coming in at about the same time when a prefire occurs which is within the accuracy of the prediction.

The inherent jitter of the 684C scope was measured by splitting a common signal and injecting one into one scope channel and the other into another scope channel simultaneously and displaying both. From the measured time differences over a series of shots, a standard deviation was calculated. In two 20 shot runs, the rms standard deviations were 8 ps and 13 ps. A value of 10 ps must be subtracted in quadrature from the standard deviations measured during the actual pulser tests to determine the actual jitter.

### 3.1.6 Parameter Variability

During the course of optimization of the TS jitter and the pulser output risetime, there were a number of important parameters that were scanned. These included the following:

- Pressure and gas type.
- Polarity.
- Stress time by dc charging the Marx to a higher or lower voltage for constant TS gap. pressure. This allowed a range of stress times on the TS of between 2 ns and 9 ns.
- Gap spacing changes. This allowed the switching fields to be varied and the mushroom stick-out distance ratio to be varied without changing the actual stick-out distance.
- The mushroom bias voltage by varying the balance circuit component values.

### 3.1.7 Chronology of Problems and Changes

Approximately 1600 shots were accumulated on the pulser test bed during the optimization. Early in the tests within about the first 400 shots, obvious problems were solved such as readjusting the gap spacings and adjusting the pressure ranges. For example, the UV gap was incorrectly set to a very large gap and this caused it to close erratically. It was then set to its present gap of about .018 inches (0.046 cm). The TTS self-break voltage also seemed erratic so the small holes previously described were drilled in the electrode tips.

During this time breakdowns were observed in the output switch region at transfer stage voltages of only 250 kV. The downstream output electrode cone shorted to ground after the OS closed within about 1 ns. This is shown in Figure 91. This problem brought about modifications that included opening the spacing between the OS switch downstream electrode cone and the adjacent ground and increasing the radii of the edge profiles in the vicinity of the peaking capacitor plastic. These changes reduced the fields in the active breakdown regions by about 10%.

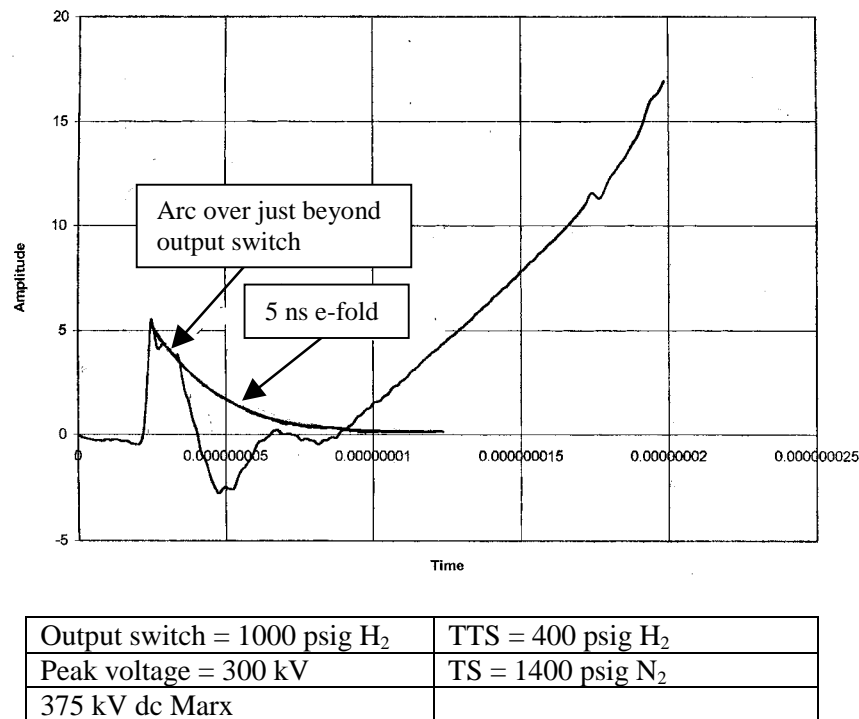


Figure 91. Oil line output (integrated D-dot).

One other problem was too large a gap spacing in the OS that caused the Cp voltage to climb too high for nominal pressures. This was closed to about 0.076 inches (0.193 cm.) down from the original 0.125 inches (0.317 cm.) so that higher pressures could be used that would better insulate the adjacent regions.

This had limited success so another modification was later made that increased the original peaking capacitor length from 0.320 inches to 0.385 inches and re-contoured the radii adjacent to

the peaking capacitor body to the extent possible. The extent of the modification was limited because the critical radii surrounding the peaking capacitor body are part of a large stainless steel plate that forms a major section of the pulser vessel. This part is very complex and expensive and in its existing form left little material to significantly increase the radius with.

The latter modification seemed to correct the output breakdown problem up to voltages of 300 kV. Because of these breakdown problems in this region of the pulser and the limits on how much improvement could be made without redesigning and fabricating the housing, the voltage limit of the test bed has been set at 300 kV.

Also encountered were extrusion problems with the O-rings under the high pressures. The flanged surfaces had to be re-machined so that the tops of the O-ring grooves would bottom-out onto the adjacent surface. If the flange bottomed somewhere else and left a tiny gap above the groove, the O-ring would extrude through this gap and the seal would fail.

Generally, jitter in the TS was found to be on the order of 300 ps to 1400 ps throughout the problem solving stage.

### **3.1.8 Results**

This program was successful in developing a high power, fast risetime, and ultra-low jitter pulser. The final performance specifications that were demonstrated were as follows:

- Output voltage: 300 kV
- Output risetime into 60-ohm oil line (10-90%): ~100 ps
- Decay time: ~5 ns
- Jitter (transfer switch trigger through output pulse): < 50 ps rms
- Triggered switch jitter: ~30 ps rms
- Transfer switch output risetime (10-90%): ~50 ps

The results are described in the following sections. The transfer switch (TS) jitter results were based on measuring the time differences between the TTS and the TS D-dot pulses as illustrated in Figure 90.

#### **3.1.8.1 Polarity**

Initially the pulser was operated by charging it with the Marx in negative output polarity. This put the charged electrode of the triggered transfer switch (TS) at a negative voltage  $V$  with the mushroom floating at approximately negative 0.8 V. The opposing electrode remained at about 0 volts prior to triggering the switch. The switch configuration at this time was a V/5 gap with the TS gap set at 0.365 cm and the mushroom sticking out 20% of this gap or 0.075 cm.

When the trigger switch (TTS) closed to launch the pulse that triggered the TS, the mushroom is driven more negative with respect to the charged TS electrode as well as with respect to the grounded electrode.

Initial results showed that the total gap was too large to enable interesting pressures of nitrogen to be used and triggering was not consistent making interpretation of the results difficult and questionable. The fields in the TS gas at practical voltages were less than 1 MV/cm for a gas that could sustain fields over 2 MV/cm at the pressures used. In addition, the possibility that the mushroom stick-out ratio of 20% of the total gap was too small was considered. The TS gap was shortened to 0.206 cm by removing a shim with no change in the stick out distance. This put the mushroom stick out ratio at 36% of the total TS gap.

With the shorter gap, triggering continued to be inconsistent because the TS gap prefired often. The mushroom external balancing components were adjusted to try to balance the voltage on the mushroom but this was not effective possibly due to inexperience with the balancing inductor and capacitor components. It seemed that the measured jitter between D-dots 1 and 2, which at times was very small (on the order of 50 ps), was erratic and subject to misinterpretation.

The early results showing low jitter between the D-dots on either side of the TS was simply the result of the TS gap prefiring. The measured jitter was the jitter of one of the two TS gaps relative to the other. Ascertaining whether a shot was a prefire or command trigger was possible only after very accurately measuring the physical distances of the D-dot locations from the TS gap and the cable lengths. Tables 7 and 8 exhibit the arrival times of the pulses for either event.

The negative triggering polarity is usually not the preferred configuration for low jitter triggering based on prior experience with conventional gaps. Thus, the Marx output polarity was reversed such that the TS charged electrode was positive giving the mushroom a positive pulse relative to ground when triggered by the closure of the TTS gap.

After reversing the polarity, the jitter was more consistent and quite small with fewer prefires. Jitter of the TS with nitrogen gas was in the range of 45 to 90 picoseconds that was measured over five series of 10-12 shots taken with approximately 220 kV on the transfer capacitor. The results are listed in Table 9.

Table 9. TS jitter (gap 0.206 cm, mushroom stick-out 36% nitrogen).							
Vch (kV)	Series	Shot No.	# of Shots in Series	TS Pressure (psig)	TS Jitter (ps)	TS Switch-out Voltage (kV)	Mean Closure Delay of TS (ns)
25	1	413-422	10	1400	89	230	1.72
25	2	438-448	11	1100	79	225	1.43
25	3	449-460	12	1000	55	222	1.34
25	4	461-472	12	900	55	220	1.29
37.5	5	516-527	12	1400	45	310	1.33

Table 9 also lists the closure delays of the TS. This is measured as the time lapse between trigger arrival to the TS and a pulse out of the TS. This delay ranged from approximately 1.7 ns to 1.3 ns. The delay tended to decrease as the pressure decreased. This is equivalent to the delay decreasing as the percent of self-break operation was increased.

However, when the Marx dc voltage was increased to 37.5 kV from 25 kV, this effectively decreased the charge time of the transfer stage. This allowed the voltage to climb to an amplitude of 310 kV on the TS (up from ~220 kV) resulting in lower jitter as well as low closure delay even at 1400 psig. Presumably this higher voltage shot was at a higher percent of self-break of the gap. The delays are plotted in Figure 92.

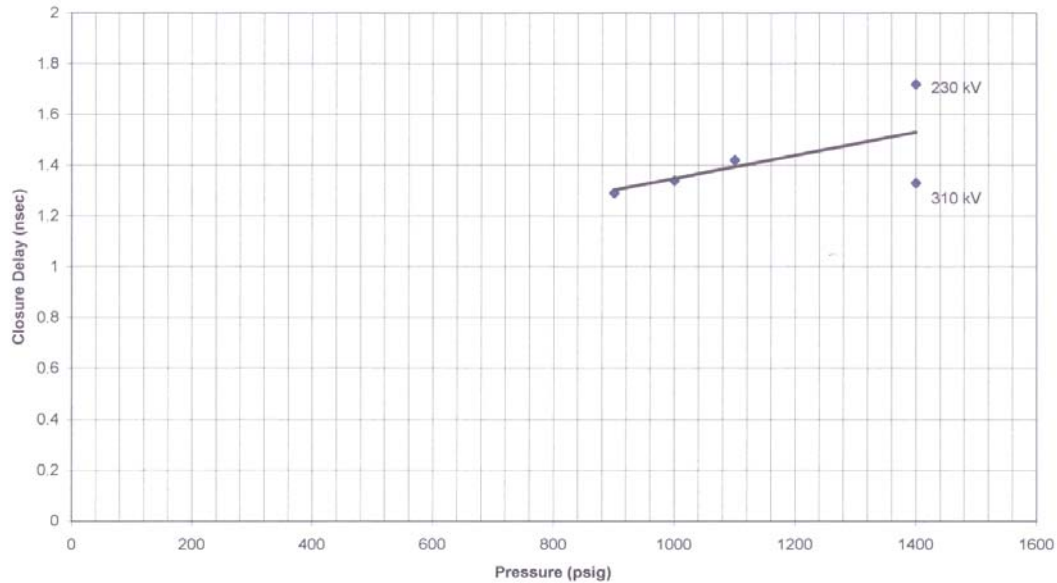


Figure 92. TS closure delay versus pressure, TS gap 0.206 cm, stick-out 35% nitrogen.

Using hydrogen in the TS resulted in too many prefires at all TS pressures and was thus, discontinued.

Triggering with positive polarity was used throughout the remainder of the pulser testing.

### 3.1.8.2 Mushroom Stick-out Distance and Gap Length

Although in the previous section the conclusion was that the jitter with a mushroom stick-out of 36% was better than that with a stick-out of 20%, the TS gap operational range topped out at only about 220 kV with a dc charge level of  $\pm 25$  kV on the Marx. The desirability to operate at up to 500 kV necessitated opening the TS gap. The gap was opened to 0.257 cm. and the mushroom was set at a stick out distance 0.0857 cm or 33% of the total gap.

The results of this TS configuration are summarized in Table 10. The table shows the TTS and TS pressures, the peak TS voltages at switch time and the estimated percent of self-break operation. The closure delays and jitter are shown for both nitrogen and hydrogen in the TS gap.

Figures 93 and 94 show plots of the TS closure delays for nitrogen versus percent of self-break operation and peak voltage respectively. These Figures compare the composite results for the runs listed in Table 10. Neither exhibits any noticeable trend unless the data from an individual run is examined. Figures 95 and 96 plot the closure delay (without subtracting the 0.475 ps correction factor) for individual shots within two of the shot runs in Table 10. A definite trend is

seen where the delay is less when the voltage is higher at fixed pressure which corresponds to operating at higher percent of self-break.

Figure 10. TS closure delay and jitter for a TS gap of 0.257 cm with 33% mushroom stick-out and positive trigger output switch gap 0.194 cm.

Marx dc Charge Voltage (kV)	Shot #	# of Shots	TTS Pressure	TS Pressure (psig)	Peak TS Voltage (kV)	TS % of Self-Break	TS Closure Delay (nsec)	TS Jitter (psec)	Gas
37.5	667-679	13	400	1000	288	85	1.90	118	N2
37.5	682-691	10	400	1100	276	80	2.02	185	N2
37.5	692-701	10	600	1500	324	72	2.07	142	N2
37.5	703-713	11	700	1500	335	73	1.83	135	N2
37.5	714-723	10	500	1200	290	80	1.60	127	N2
45	787-796	10	1200	1200	309	82	1.78	110	N2
45	797-807	11	1400	1200	312	83	2.00	302	N2
45	819-828	10	400	1000	279	85	1.63	309	N2
45	829-838	10	800	1000	274	85	2.03	128	N2
37.5	740-750	11	800	1500	225	~72	1.77	445	H2
37.5	752-761	10	900	1500	219	~70	1.07	424	H2
30	771-780	10	800	1500	213	~70	1.49	330	H2

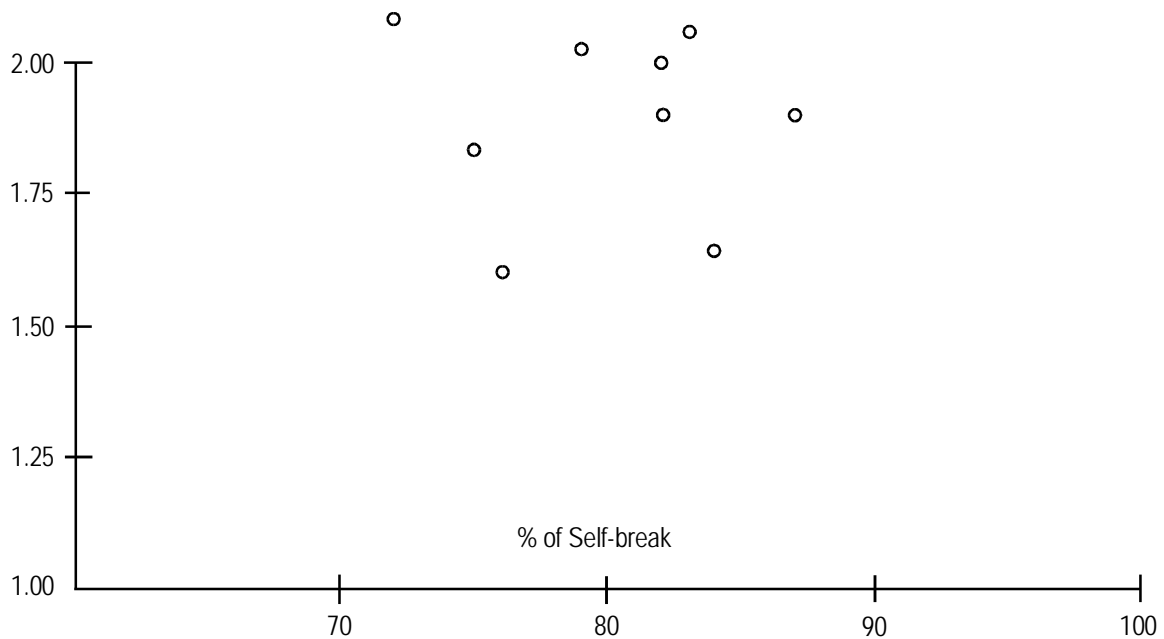


Figure 93. TS closure delay as a function of % of self-break; TS gap 0.257 cm, nitrogen gas, mushroom stick-out 33% (data from Table 10).

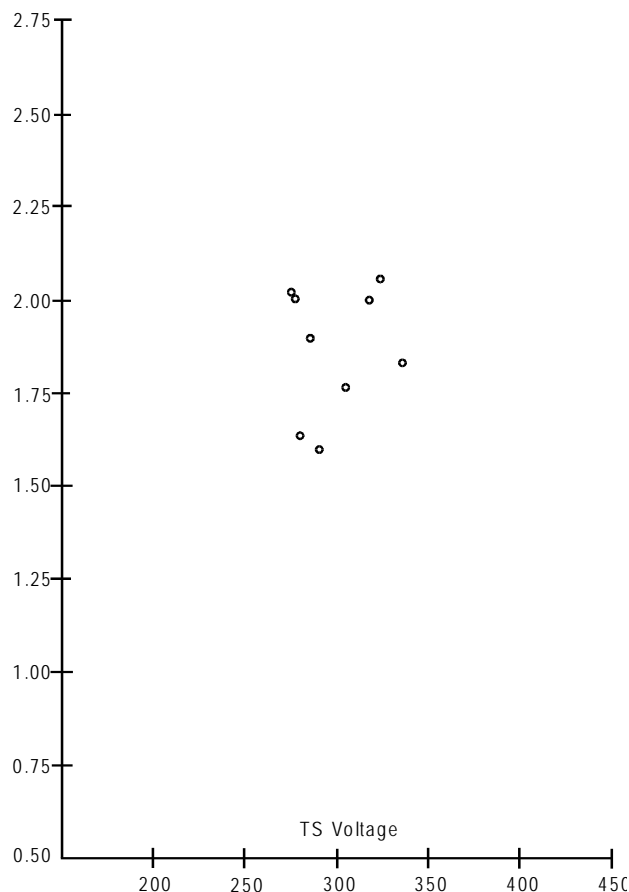


Figure 94. TS closure delay versus voltage with nitrogen gas; TS gap is 0.257 cm, stick-out 33% (data from Table 10).

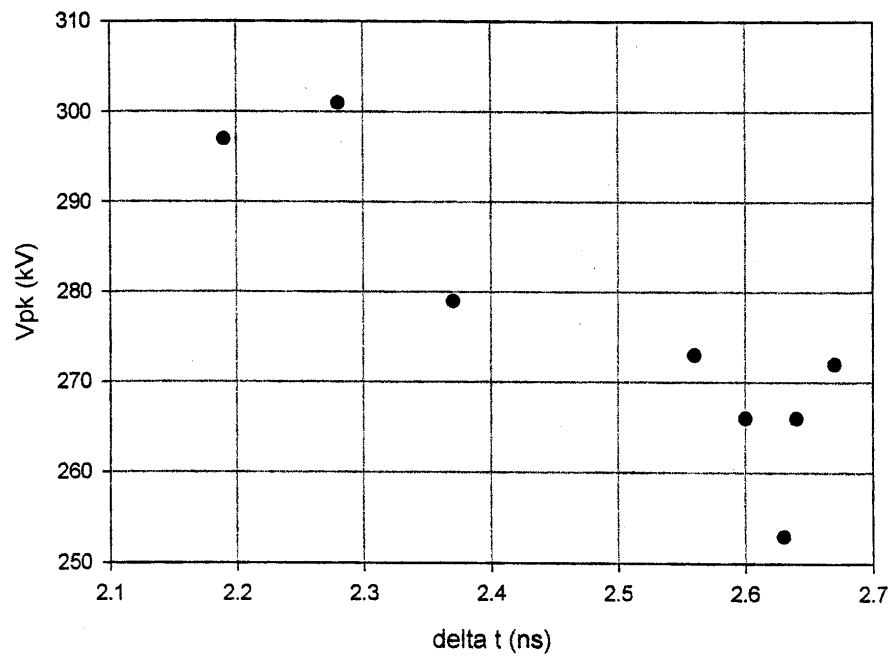
The typical variation in the switch-out voltage, which is illustrated in Figures 95 and 96, was caused by the jitter in the self-breaking TTS switch. Recall that this switch self-breaks and the jitter of the TS is determined simply by the standard deviation between the trigger input and pulse output times of the TS switch only. Thus, the jitter in the TTS equates to amplitude jitter in the TS voltage. This can also contribute to the TS jitter.

Figure 97 plots the TS jitter from Table 10 as a function of percent of self-break for both the nitrogen and hydrogen. There is a noticeable trend for the jitter to decrease as the percent of self-break increases for nitrogen. Hydrogen performance shows no trend and remained high. Generally, the jitter performance with nitrogen was orders of magnitude better than with hydrogen as had been the observation previously.

Since the performance of the 0.257 cm TS was never as good as that observed when the gap was 0.206 cm, the gap was changed to 0.226 cm. This spacing was chosen to enable the desired high voltage operation while being closer to the previous successful operating parameters.

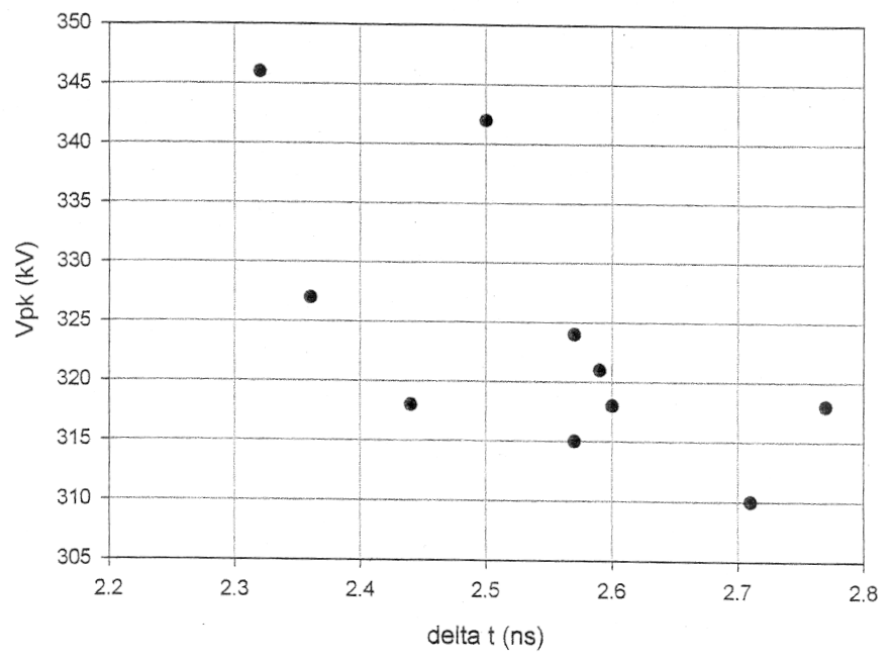
Table 11 shows the runs taken with the gap of 0.226 cm with nitrogen. Beginning with these runs, the mushroom voltage was recorded for each shot. This enabled the degree of the balancing of the mushroom voltage to be observed. Ideally, by conventional wisdom, the mushroom should

be balanced by the external inductance and capacitance to float prior to triggering at the equipotential that would exist if there were no mushroom.



Estimated % of Self-break | 85% | 79% | 74%

Figure 95. TS closure delay versus peak voltage for shots 682-691; TS gap 0.257 cm.



Estimated % of Self-break | 76% | 72% | 70%

Figure 96. TS closure delay versus peak voltage for shots 692-701; TS gap 0.257 cm.



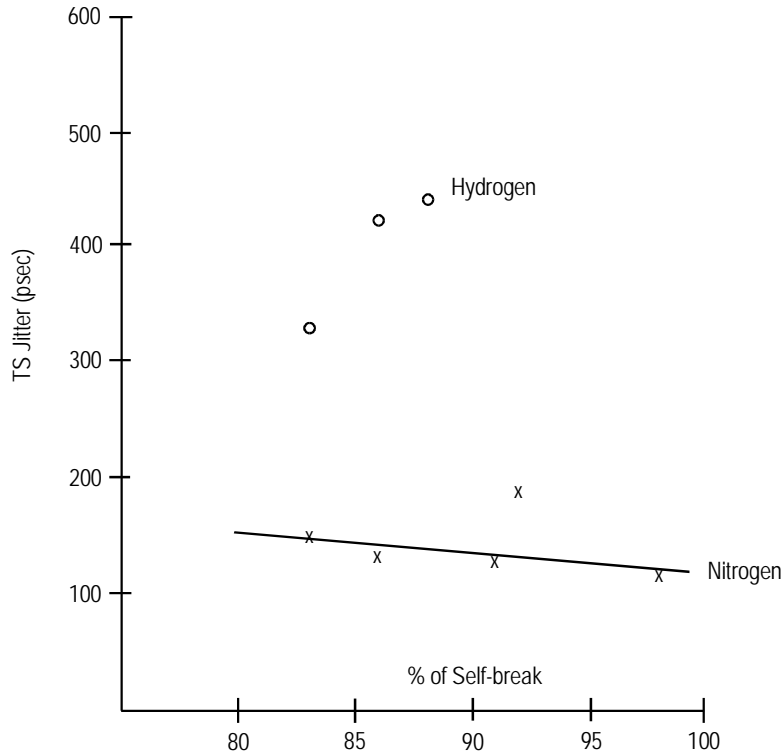


Figure 97. TS jitter vs percent of self-break for gap 0.257 cm and stick-out 33% (data from Table 10).

Marx dc Voltage (kV)	Shot #	# of Shots	Pressure		Peak Voltage		Balance %	TS % of Self-Break	TS Closure	
			TTS (psig)	TS (psig)	TTS (kV)	TS (kV)			Delay (nsec)	Jitter (psec)
30	870-890	21	600	600	29	147	22	78	1.70	151
30	924-933	10	600	800	33	157	21	70	2.13	272
30	934-943	10	600	1000	36	161	24	56	2.62	250
30	944-953	10	800	600	31	156	22	82	1.56	112
30	954-963	10	800	800	38	163	24	68	1.94	121
30	964-973	10	800	1000	35	168	23	60	2.71	186
30	974-983	10	800	1200	43	183	24	55	2.89	252
30	984-993	10	800	1400	41	194	23	53	3.37	292
30	994-1003	10	1000	800	46	185	27	76	1.69	112
30	1004-1013	10	1000	1000	45	178	28	64	2.03	182
30	1014-1023	10	1000	1200	47	191	27	60	2.75	287
30	1024-1033	10	1000	1400	45	195	25	55	3.07	383
30	1034-1043	10	1200	800	51	191	29	81	1.17	450
30	1044-1053	10	1200	1000	45	182	27	62	2.54	478
30	1054-1063	10	1200	1200	52	223	26	66	2.16	166
30	1064-1073	10	1200	1400	46	208	24	56	2.90	356
30	1074-1084	10	1380	800	48	192	27	82	1.09	496
30	1085-1094	10	1380	900	47	179	29	68	1.73	139
30	890-899	10	1400	1000	53	208	28	72	1.56	184
	903-913	11	1400	1100	54	222	27	70	1.66	174
30	914-923	10	1400	1200	54	221	27	66	1.84	153

By measuring the amplitude of the integrated TTS D-dot waveform and comparing it to the voltage at the time of trigger arrival, one is able to estimate the degree of balancing within the gap. In the case of the data in Table 11, the mushroom stick out ratio is 38%. Thus, the mushroom should be balanced to be at this ratio before and at the time of triggering.

Before calculating the balance ratio from the waveforms, the switch out voltage measured by the transfer capacitor D-dot has to be adjusted. The adjustment is necessary to account for the transit time between the TTS trigger pulse sweeping past the D-dot and the time it arrives at the TS gap and the closure delay of the TS gap. The transfer capacitor D-dot does not know that the TS has been triggered and has closed for this time lapse and continues to climb in amplitude. These delays amount to about 2 to 2.5 ns in total.

A transfer capacitor D-dot waveform is shown in Figure 85 and taken from a shot where the Marx dc charge was 37.5 kV. Peak voltage is reached in 20 ns. By the time this D-dot recorded the peak voltage, the TTS voltage had been observed 2-2.5 ns earlier and the TS voltage was 88% of the observed peak. Thus, the mushroom voltage is compared to this lesser value to calculate the ratio.

For other Marx charge voltages, this time discrepancy will vary. For 45 kV, the time to switch out will be approximately 15 ns and for 30 kV it will be about 25 ns. For the faster charging at 45 kV, the actual TS voltage at the time of triggering will be only 84% of the peak measured by the D-dot. For the slower charging 30 kV case, the voltage at the time of triggering will be 91% of the measured D-dot peak.

In Table 11, the peak voltages cited are those actually measured by the transfer capacitor D-dot even though the balance ratios are calculated as previously described. The dc Marx charging voltage used throughout the runs in Table 11 was 30 kV.

The balancing ratios are on average about 25%. This is far less than 38% that is the physical ratio of the spacing.

Generally, the results are quite similar to those obtained with the 0.257-cm TS gap. If anything the percent of self-break operation for the runs in Table 11 may be somewhat lower than those in Table 10 which might imply better general performance based on the premise that performance improves with higher percent of self-break operation. Figure 98 plots the jitter of the TS versus the percent of self-break for nitrogen. The trend is similar to that of the 0.257 cm gap with the jitter decreasing as the percent of self-break increased.

Testing with the 0.226 cm gap continued with changes in the mushroom balancing components that would have been expected to decouple the mushroom from ground and reduce the balance ratio. To do this, the balancing capacitance was decreased. The Marx dc charge voltage was also raised to 37.5 kV. This change would have the effect of producing a faster charge time on the TS and also increasing the peak voltage at a given pressure due to the time dependence of the gas breakdown.

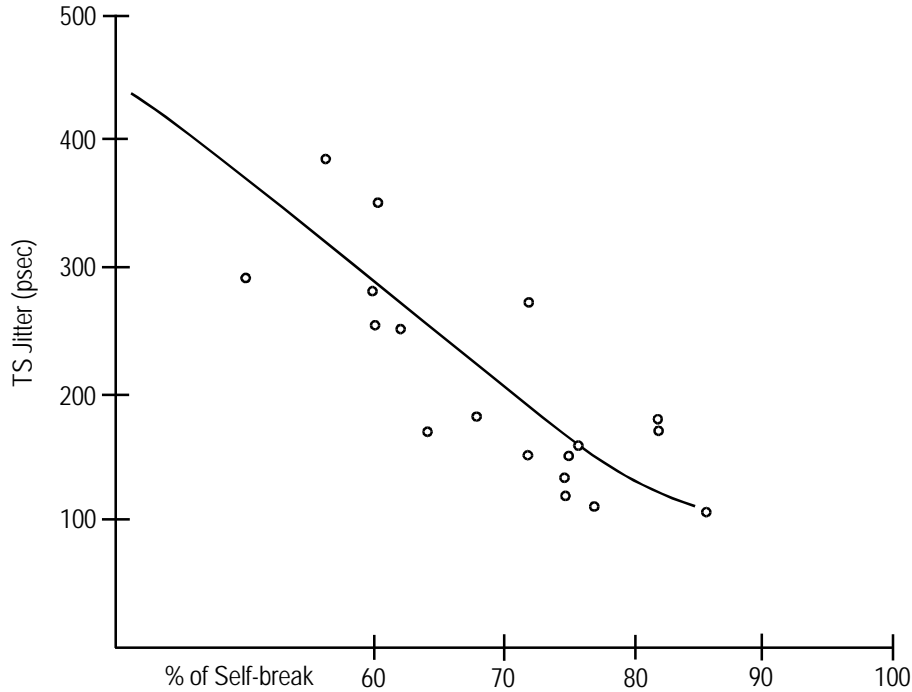


Figure 98. TS jitter vs. percent of self-break for a gap of 0.226 cm with nitrogen and mushroom stick-out 38% (from Table 11).

Table 12 summarizes the results of these higher Marx voltage runs with the decoupled mushroom. Although cutting the capacitance reduced the coupling by a factor of two, the calculated balance ratios were very similar to those previously determined. Evidently, other factors may have determined the balance ratio. Most likely, more dominant stray capacitance controlled the coupling to the ground as well as to the pulser body so that changes in the lumped components had little effect. The balance ratios in Table 12 were in the range of 24-26% or about the same as for the runs in Table 11. A further change in coupling by another factor of two in capacitance seemed to shift the balance ratio up a little to between 28-30%.

The operating percent of self-break for the Table 12 runs on average ran somewhat higher than the previous runs in Table 11 and perhaps explain some of the improvement in TS jitter. The percent of self-break was about 70-75%. The TS jitter in Table 12 was consistently below 100 ps and even touched 32 ps.

When the balance ratio was raised a little to between 28% and 33% and the Marx charge voltage was raised to 45 kV, the jitter seemed to improve a little to consistently hover around 30-50 ps.

Figure 99 plots the closure delay of the TS versus percent of self-break for the data presented in Table 12. There appears to be no trend. Figure 100 plots closure delay versus TS peak voltage and shows no trend.

Figure 101 plots the TS jitter versus percent of self-break taken from Table 12 without a noticeable trend.

Table 12. TS gap closure delay and jitter (0.226 cm, mushroom stick-out 38%, positive trigger polarity; OS gap 0.105 cm, 37.5 kV and 45 kV Marx charge).

			Pressure (psig)			Peak (kV)			TS			OS	
Marx dc Voltage (kV)	Shot No.	# of Shots	TTS	TS	OS	TTS	TS	Mush-room Balance %	% of Self-break	Closure Delay (ns)	Jitter (ps)	$\Delta t$ (ns)	Jitter (ps)
Coupling Change													
37.5	1245-1264	19	800	1200	1000		259		76	1.89	91		
37.5	1265-1277	12	900	1200	1000		260		76	1.89	100		
37.5	1291-1300	10	950	1400	1200	70	305	26	70	1.46	292		
37.5	1301-1311	11	900	1400	1200		301		74	1.39	60		
37.5	1312-1322	11	850	1400	1400	63	288	25	70	1.70	68		
37.5	1323-1336	13	880	1400	1200	64	290	25	71	1.49	62		
37.5	1340-1349	10	850	1500	1500	64.5	283	26	70	1.62	32		
37.5	1350-1359	10	900	1500	1500	64.3	305	24	74	1.63	125	0.36	105
37.5	1360-1369	10	870	1500	1500	63.5	298	24	73	1.76	132	0.36	116
Coupling Change													
37.5	1381-1391	11	880	1400	1500	84.3	286	33	86	1.60	47	0.32	81
45	1393-1402	10	650	1200	1500	67	256	30	70	1.48	31	0.62	88
45	1413-1425	12	500	1000	1200	60	248	28	70	1.51	36	0.39	60

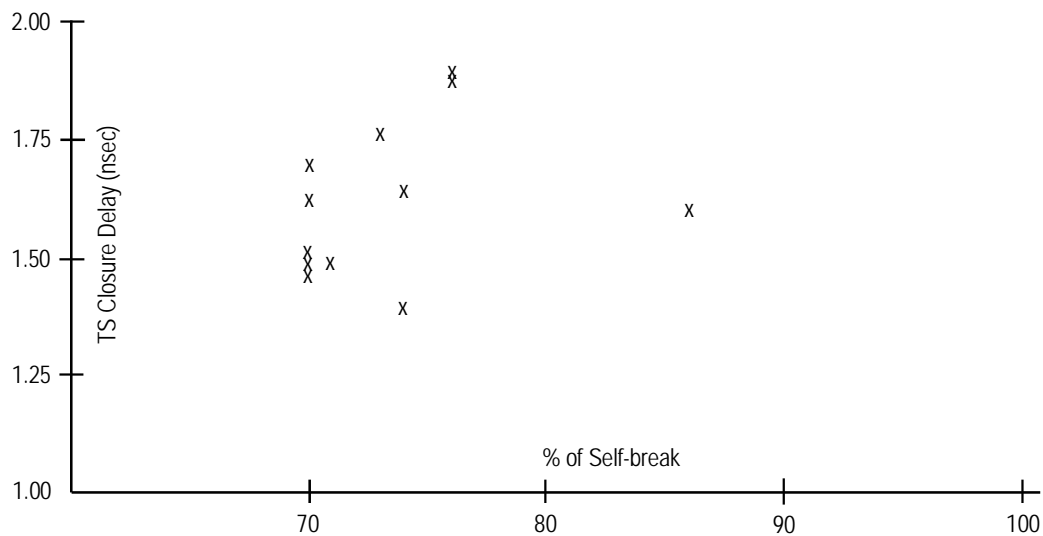


Figure 99. TS closure delay vs. percent of self-break with nitrogen and 0.226 cm gap; 38% mushroom stick-out (from Table 12).

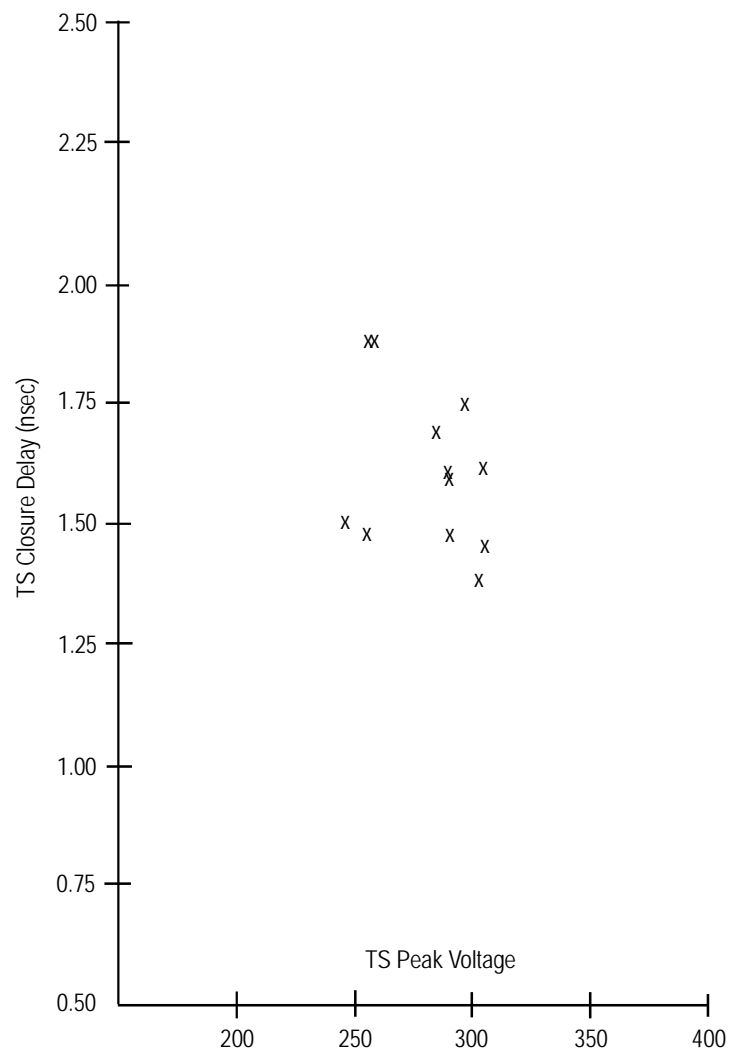


Figure 100. TS closure delay vs. peak voltage with nitrogen, gap = 0.226 cm, 38% mushroom stick-out (from Table 12).

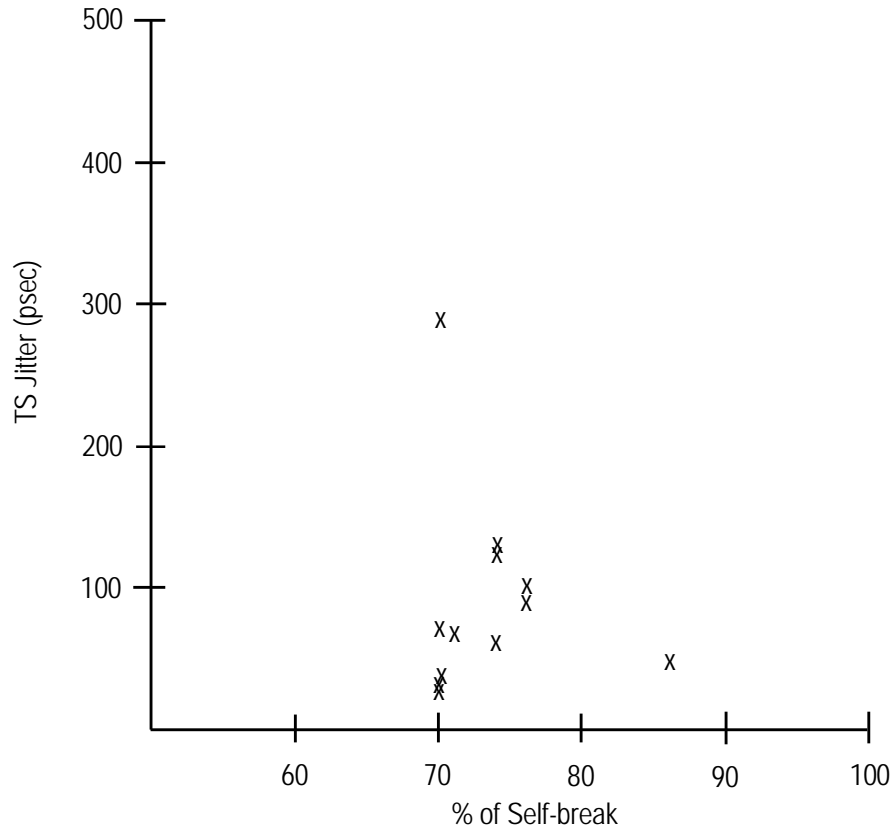


Figure 101. TS jitter vs. percent of self-break, nitrogen gap 0.226 cm, mushroom stick-out 38%, 37.5 kV Marx (from Table 12).

In the runs of Table 12, the delays and jitter of the output switch (OS) were also recorded. The OS gap during these runs was set at 0.105-cm. The peaking capacitor and OS were charged in approximately 1.8 ns to switch out and the switch out voltage was about 300 kV.

The OS jitter was computed by quadrature subtraction of the TS jitter from the overall throughput jitter of both the TS and OS. The OS jitter was surprisingly high. The calculated jitter of the OS was between 60 and 100 ps.

It has been observed that the UV-illuminator gap wore quite rapidly because of its extremely small pointed tip and the current densities produced during the discharge. This evidently contributed to the jitter. By continually readjusting this gap spacing to a value of 0.045 cm at opportune times, the jitter could be minimized but as it wore down, the jitter did rise appreciably. When worn, the gap opened up by 50% or more of its initial spacing.

The effectiveness of the UV gap for illuminating the OS was never determined with certainty. It was planned to purposely turn off the gap by shorting it or shielding it but this was never done.

For the UV illumination to be effective in achieving a diffuse bulk breakdown of the gas, one must pulse charge the gap in a time small in relation to the formative time of the gap.

A limited number of measurements taken during these pulser tests with hydrogen in the TS showed that the closure delay (formative time) was about 1 ns. Thus, with the charge time of 1.8 ns on the peaking capacitor circuit, this may be too long a time to achieve a diffuse breakdown of the gas.

Figure 102 plots the closure delays for each shot in a run at 1400 psig nitrogen in the TS which was shown in Table 12. The shots are plotted with the voltage of each shot. The jitter is a very low 47 ps with an average closure delay of  $2.1 - 0.475 = 1.63$  ns. There is virtually no variation in delay with TS peak voltage.

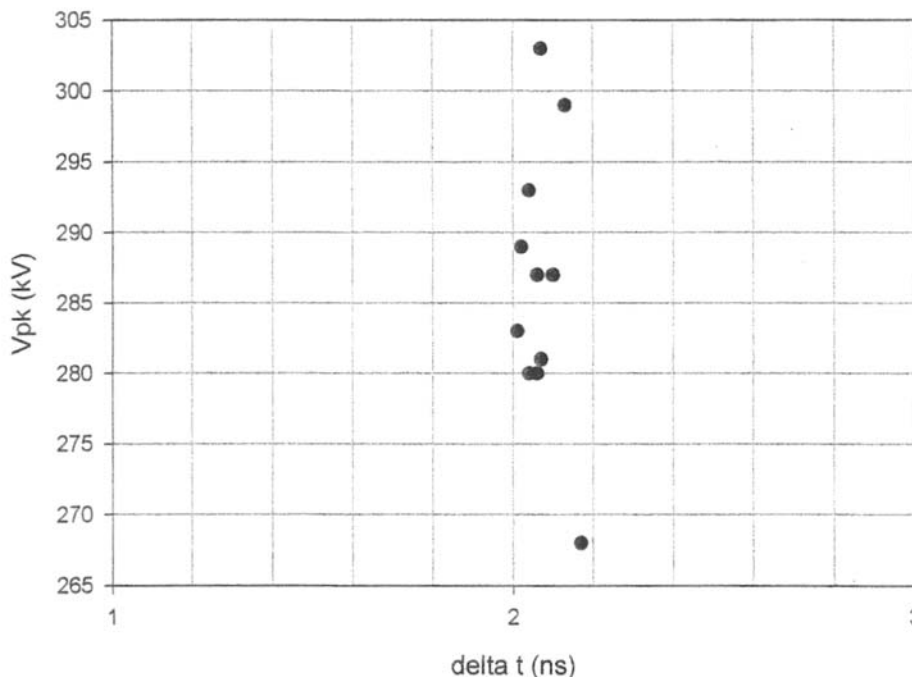


Figure 102. TS closure times as a function of peak voltage for shots 1381-1391 (from Table 12).

Figures 103 and 104 plot the TS and OS delays for the individual shots in two of the runs shown in Table 12. There is no significant change in closure delays with TS peak voltage.

A close examination of the jitter results seemed to indicate that the most significant reductions in the jitter had occurred when the Marx dc charge voltage was increased from 30 kV to 37.5 kV and then to 45 kV. This was further reinforced by the results summarized in Table 13.

Table 13 runs were taken with the TS gap unchanged at 0.226 cm with nitrogen but with the Marx dc charge level at 45 kV. The OS gap was 0.105 cm with hydrogen. The external coupling capacitance of the mushroom to ground was reduced by another factor of two after the second run sequence in the table.

The balancing of the mushroom voltage started out at about 36% with a jitter in the TS of 30 ps. After readjusting the balance, the mushroom voltage was at about 22-23% of the gap voltage. Still, the jitter stayed in the range of 25 ps to 38 ps. Operation during these runs was at about 80% to 95% of self-break.

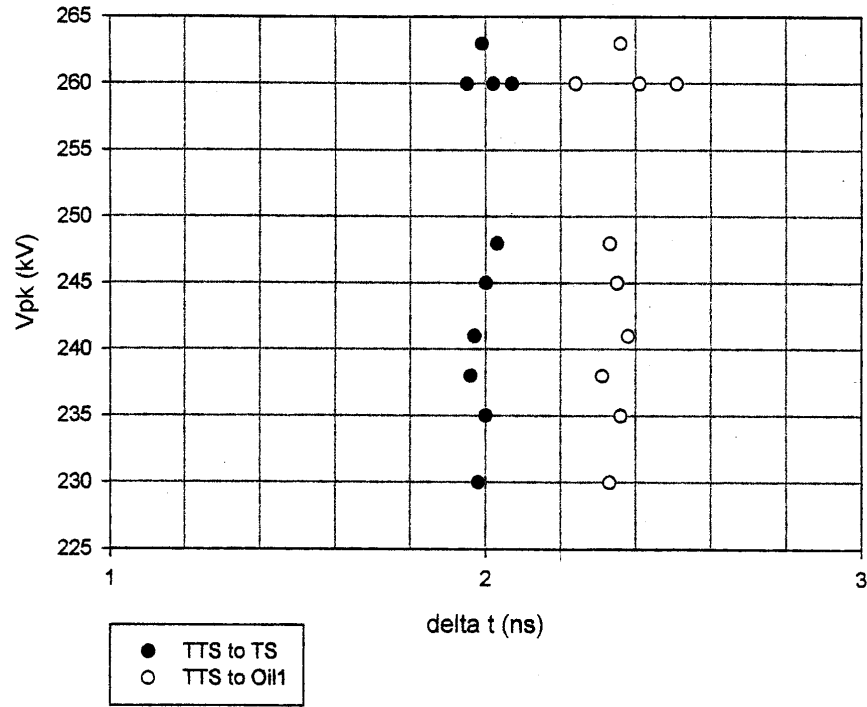


Figure 103. TS and OS closure times as a function of TS voltage for shots 1413-1425 (from Table 12).

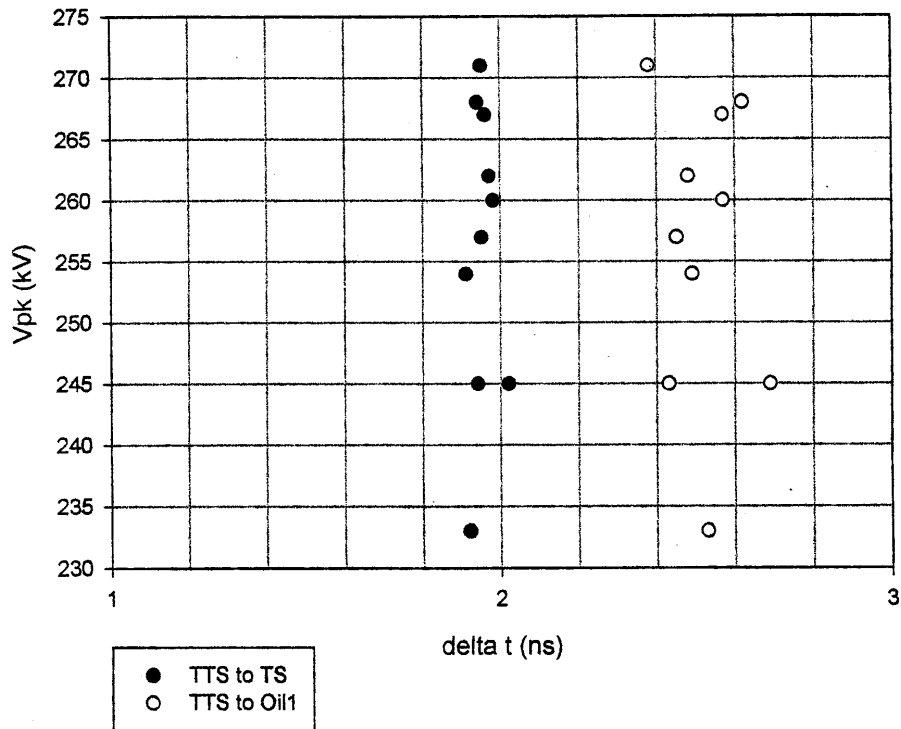


Figure 104. TS and OS closure times as a function of TS voltage for shots 1393-1402 (from Table 12).



Table 13. TS gap closure delay and jitter (0.226 cm, 38% stick-out, nitrogen; OS gap 0.105 cm, 45 kV Marx charge).

Shot No.	# of Shots	Pressure TTS (psig)	Pressure TS (psig)	Peak TTS (V)	Peak TS (V)	Mush-room Balance %	TS % of Self-break	TS Closure Delay	TS Jitter (ps)	Meas. TS to OS Delay Time	OS ( $\sigma$ )
1446-1455	10	650	1200	78	261	36	78	1.61	30	0.49	110
Coupling Change											
1457-1471	15	650	1000	54	285	23	98	1.20	28	0.49	28
1473-1482	10	650	1200	54	292	22	92	1.24	30	0.53	37
1485-1494	10	600	1000	52	275	23	94	1.16	25	0.48	42
1525-1555	31	650	1200	52	279	25	83	1.23	36	0.50	67
1556-1580	24	600	1000	50	270	22	92	1.18	38	0.45	56

The charge time of the peaking capacitor was a little longer than the data in the previous tables as implied by the delay between the measured TS and OS arrival times. The difference was about 150 ps. The jitter of the OS was mostly in the range of 28 to 67 ps. Perhaps this had something to do with the somewhat later switching of the OS.

Figure 105 plots the TS closure delay versus percent of self-break operation from Table 13 and shows no dependence of delay on the operating percent of self-break.

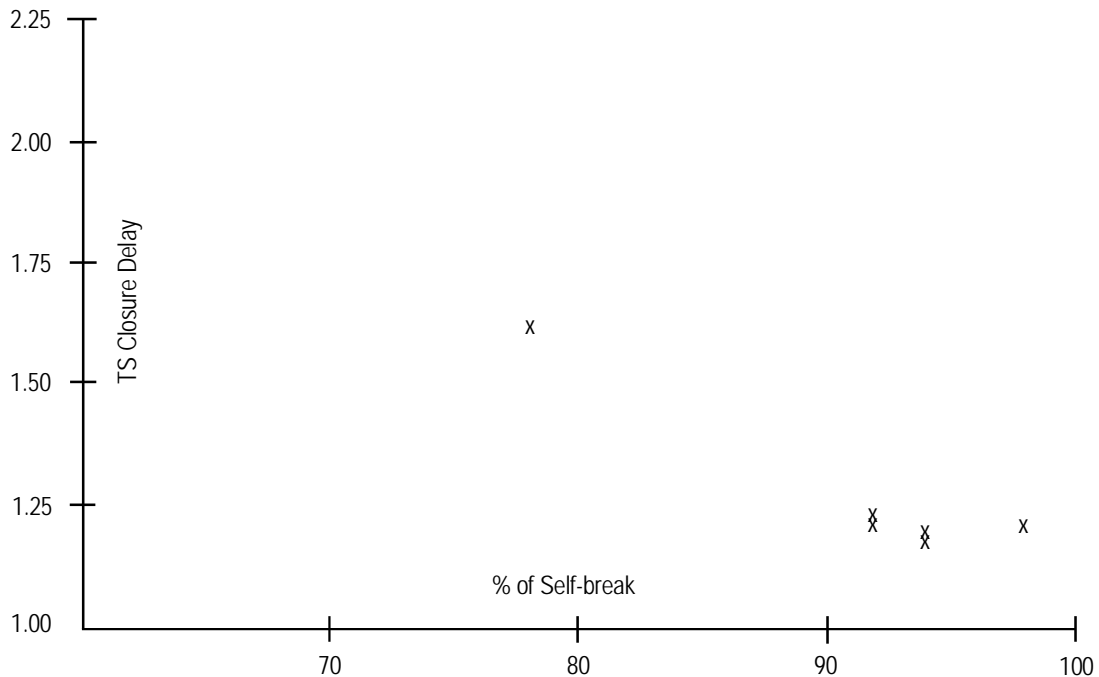


Figure 105. TS delay vs. percent of self-break (from Table 13).

Figure 106 plots the TS closure jitter versus percent of self-break operation from Table 13 and also shows no relationship between the two parameters.

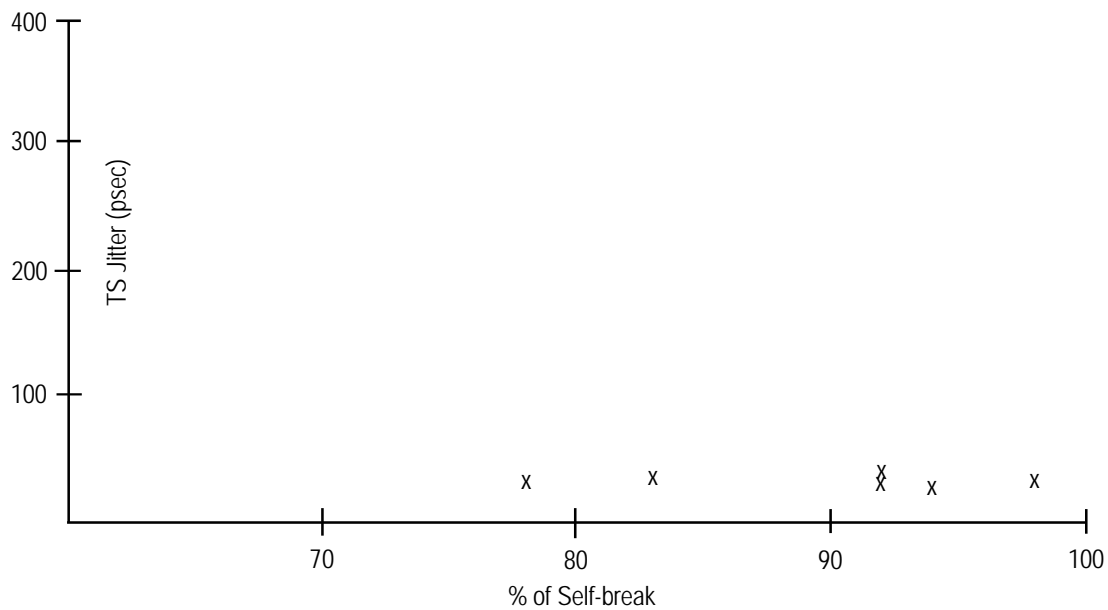


Figure 106. TS jitter vs. percent of self-break with nitrogen, gap = 0.226 cm, mushroom stick-out 38%.

Figures 107 and 108 show the individual shot data for two of the run sequences in Table 13 where the arrival times of the TS and oil line D-dot signals are plotted against peak TS voltage.

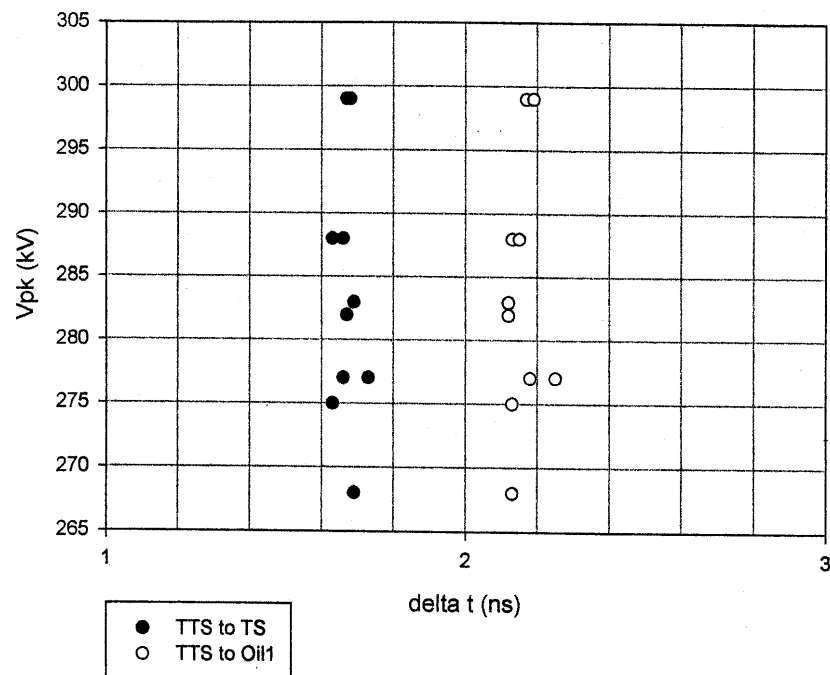


Figure 107. TS and OS closure times as a function of TS voltage for shots 1457-1471 (from Table 12).

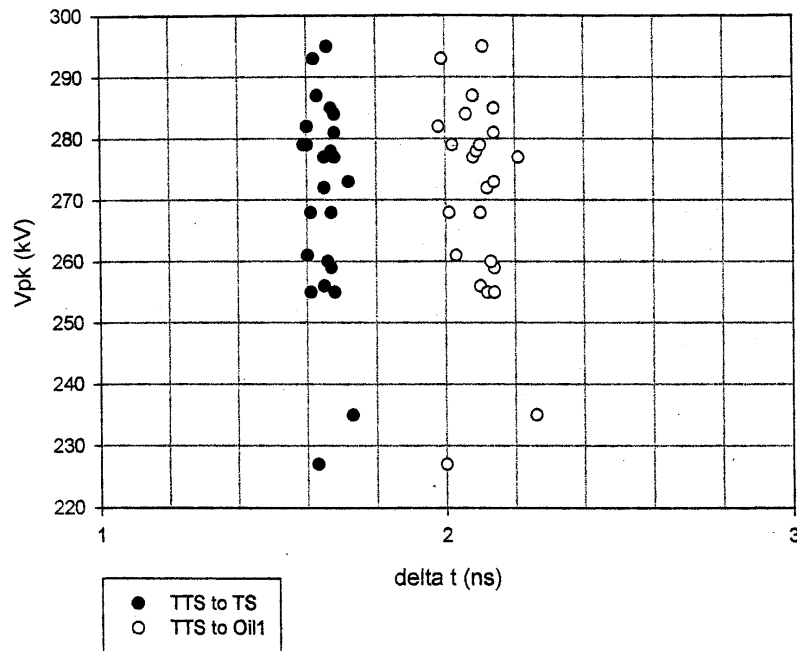


Figure 108. TS and OS closure times as a function of TS voltage for shots 1556-1580 (from Table 12).

### 3.1.8.3 TS and OS Risetimes

The TS output risetime with 1000 psig nitrogen was measured and found to be about 300 ps (10-90%) after correcting for the 100 ps diagnostics and instrumentation system. The switching fields in the TS were 1.35 MV/cm. Figure 109 shows this waveform. The waveform risetime is difficult to measure with any accuracy because of the turn that the wave has to make before it is detected by the D-dot and because of the mismatch when the wave slaps against the Torlon insulator. Thus, what is observed is the initial rising portion of the wave and then a momentary doubling when it reflects off the mismatch.

The TS risetime with 1500 psig hydrogen was found to be 137 ps (10-90%) after correction. The switching fields in the TS were 1.23 MV/cm. This waveform is shown in Figure 110 where only the rising portion before the doubling was recorded.

An estimate was made of the number of arc channels needed to achieve the risetimes cited above for the two gases. The method used calculated the inductive risetime based on Equation (4) where the L was estimated at 15 nH per cm of gap length and the total L was the inductance per channel divided by n where n is the number of channels.

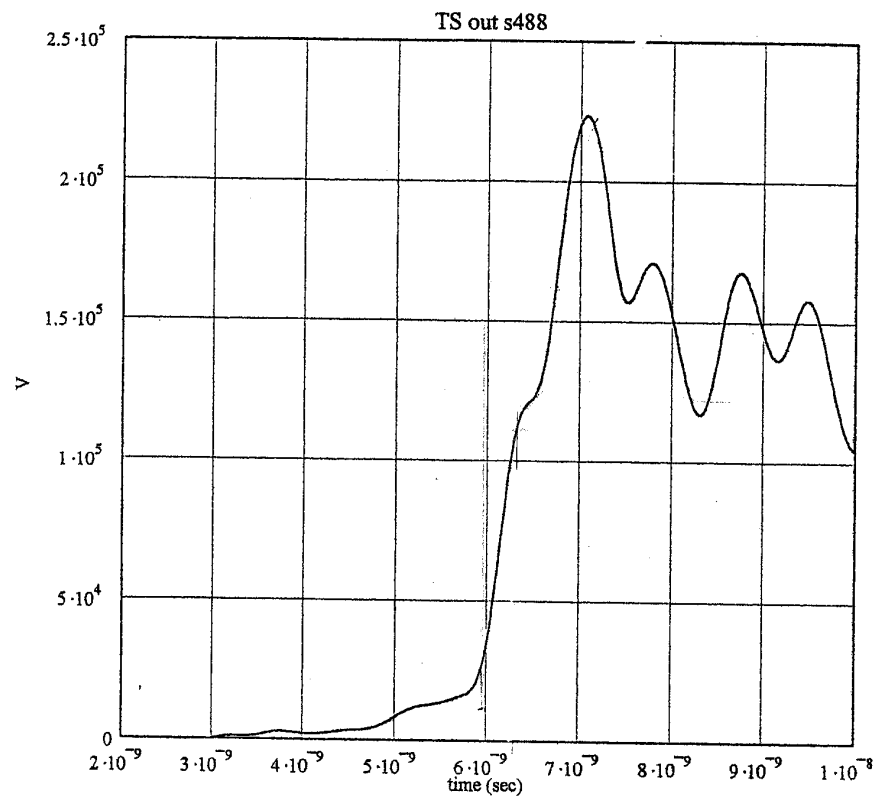


Figure 109. TS output pulse with nitrogen, risetime = 300 ps.

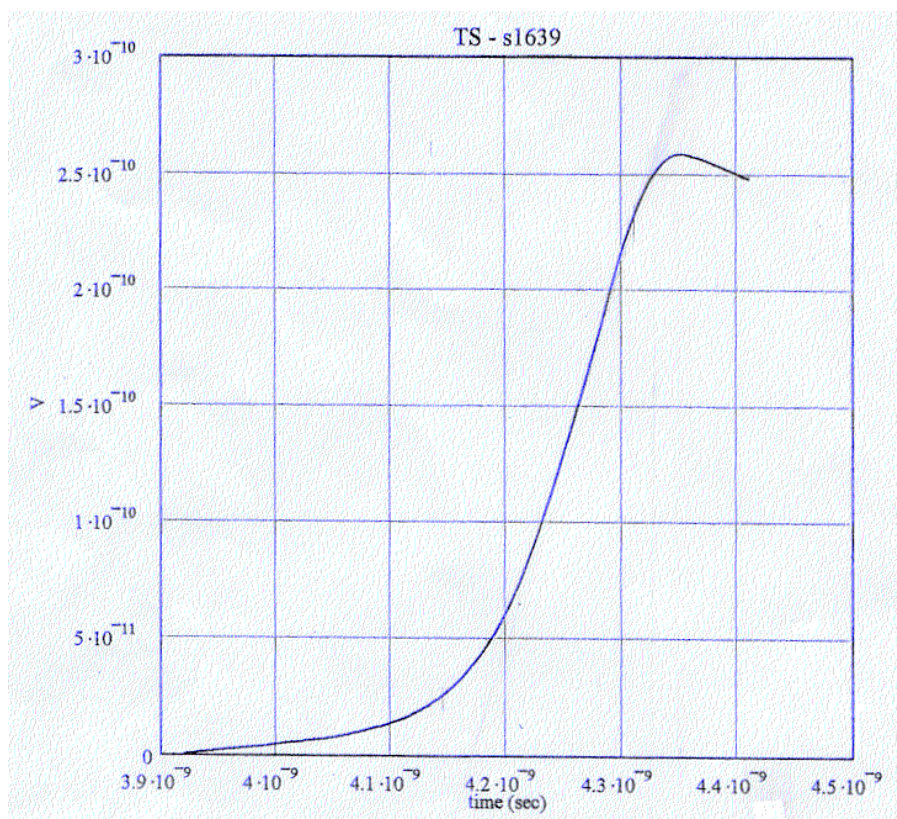


Figure 110. TS output pulse with hydrogen, risetime = 137 ps.

To estimate the resistive phase, Equation (1) was used. The impedance  $Z$  was adjusted for the number of channels by using an equivalent  $Z$  in the equation of  $n$  times  $Z$  where  $Z$  is the driven impedance of about 15 ohms. Earlier estimates of the resistive phase for nitrogen and hydrogen were described. The calculated nitrogen resistive phase risetime was twice the actual measured value. The calculated hydrogen risetime was very close to that measured.

The overall risetime is the quadrature sum of the two components.

Thus, for nitrogen, a calculated risetime of about 600 ps which is twice that measured implies five channels. For hydrogen, a calculated risetime of 137 ps implies channels numbering 5 to 10. This is reasonable number of channels comparable to the number observed in the 1MV fast risetime switching experiments described in Section 1.3.

The oil line risetime obtained from the oil line D-dot monitor measured the OS risetime into the 60-ohm coaxial line. This risetime was measured to be between 135 ps and 150 ps which after correction was between about 95 ps and 112 ps respectively. An example of this waveform is shown in Figure 111 that has an uncorrected measured risetime of 140 ps. Corrected for band width limits of the measuring system, this would imply a risetime of ~95 ps. The OS gap was 0.105 cm and the pressure was 1500 psig hydrogen. The switching field was about 3 MV/cm.

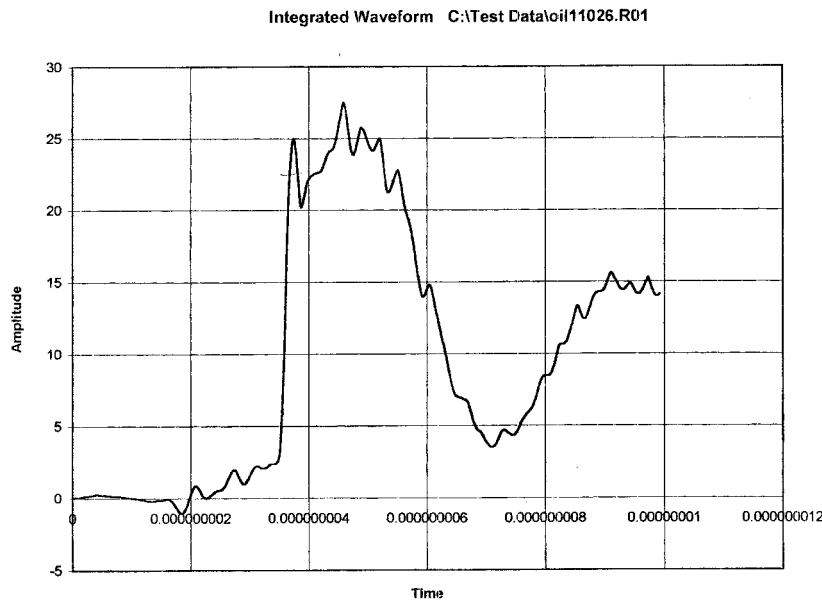


Figure 111. Output voltage from integrated oil line D-dot output voltage ~280 kV.

Estimating the number of channels in the manner described above, the implied number of channels for a 95 ps risetime is about three. Thus, it would appear that the OS switches with three channels.

However, if the fill time of the wave in the vicinity of the OS is taken into account, the actual contribution of the arc risetime is less than 95 ps. The fill time of the switch region is approximately 50 ps which is the two-way transit time from the switch apex to ground. Thus,

subtracting the fill time contribution from the overall risetime leaves 80 ps which could be attributable to the actual arc risetime.

A re-calculation of the arc risetime implies three to four channels in the OS. This would put the effectiveness of the UV illumination in question because as many channels were created in the TS without external UV illumination.

### **3.1.9 Next Generation Pulser**

The next generation pulser could potentially use only a single stage with hydrogen gas as the switching medium. This approach is attractive because it would minimize the throughput jitter by eliminating the jitter associated with the peaking stage and illuminator gaps.

The erratic and rather high jitter observed with hydrogen might have been caused by two factors. The first is the lack of precise control of the balancing of the mushroom. The second is that the shorter (1 ns) formative time of hydrogen may require a faster charging of the pulser to compensate.

More precise control of the mushroom balancing could be achieved by providing a coaxial-like capacitive voltage divider rather than lumped elements. This could be realized by surrounding the trigger coax with a grounded cylinder so that the full pulser charge voltage is taken up between this cylinder and the trigger coax outer conductor. Another cylinder is placed between these two coaxial conductors at the desired location to divide the voltage while being connected to the trigger coax inner conductor which is also the potential of the mushroom.

In view of the sensitivity of the TS jitter to the charge time of the pulser where it seemed that the streamer growth processes associated with the slightly enhanced mushroom edge prior to triggering were important, a more rapid charge time may improve hydrogen performance. By simple scaling of the formative times of nitrogen to hydrogen, perhaps a charge time of 10 ns would achieve good jitter performance and stability with hydrogen.

If a single hydrogen switch were feasible, each could feed multiple cables that in turn drive individual antennae. Multiple hydrogen switches could be triggered by a common source.

It is conceivable that such a single switch could operate at 500 kV with a jitter of 30-50 ps and produce a risetime of < 100 ps.

## 4.0 CONCLUSIONS

It has been shown that an ultra-low jitter electrically triggered gas switch is feasible. A pulser using such a switch has been demonstrated that produces up to a 300 kV output pulse with a 100 ps risetime and  $< 50$  ps jitter.

To achieve the optimum performance, virtually all of the design features thought to be essential were evidently necessary. For example, the best results were achieved with the use of high-pressure gas in all of the switches in the 80 to 100 atmosphere range. A positive trigger was essential as well as the use of a rapidly rising trigger pulse. A peaking circuit and hydrogen output switch was necessary for the fast output risetime. A rapidly applied charging voltage on the triggered switch reaching peak in about 15 ns was proven to be necessary to consistently achieve jitter  $< 50$  ps. Operating the TS at 75-85% of self-break also appeared optimal.

Nitrogen was better than hydrogen in the TS for low jitter triggering. This might be due to the differences in the characteristics of the two gases for point plane breakdown. This situation occurs when the trigger pulse swings the mushroom and enhances the edge to extremely high fields. Nitrogen has a more dramatic degradation in the mean breakdown field than hydrogen perhaps making nitrogen more conducive to streamer growth and triggering.

In most of the shot runs taken, the mushroom appeared to be biased in potential closer to the charged TS electrode than its physical position would call for. It is possible that this pre-ionizes the gas surrounding the mushroom edge before the trigger arrives and results in free electrons available for the ultimate avalanche and closure with low jitter.

The most apparent factor in reducing the jitter was the Marx dc charge voltage that resulted in charging the TS faster. It was surprising that the difference between 15 ns at 45 kV and 25 ns at 30 kV could have made such a difference in the TS jitter in the later test runs. Perhaps this application time had some effect on the streamer growth from the edge of the mushroom prior to triggering.

Previous multi-channel switch tests have shown that the number of channels was greater when a faster charge time was used. Although no jitter data was taken at the time, better multi-channeling might well imply lower jitter.

The estimated number of channels in the OS implied that the UV illumination effectiveness was questionable or that the formative time of the hydrogen was much shorter than the voltage application time.

## DISTRIBUTION LIST

DTIC/OCP 8725 John J. Kingman Rd, Suite 0944 Ft Belvoir, VA 22060-6218	1 cy
AFRL/VSIL Kirtland AFB, NM 87117-5776	1 cy
AFRL/VSIH Kirtland AFB, NM 87117-5776	1 cy
Official Record Copy AFRL/DEHP/Tyrone Tran	1 cy
Vic Carboni TITAN Systems Corporation Pulse Sciences Division 2700 Merced Street	1 cy
David V. Giri Pro-Tech 11-C orchard Court Alamo, CA 94507-1541	1 cy
Everett G. Farr Farr Research, Inc. 614 Paseo Del Mar NE Albuquerque, NM 87123	1 cy